Self-organized surface patterns originating from femtosecond laser-induced instability

Self-organized surface patterns originating from femtosecond laser-induced instability

Von der Fakultät für Mathematik, Naturwissenschaften und Informatik
der Brandenburgischen Technischen Universität Cottbus
zur Erlangung des akademischen Grades

Doktor der Naturwissenschaften
(Dr. rer. Nat.)

genehmigte Dissertation

vorgelegt von

Diplom-Physikerin

Olga Varlamova, Shelonkina

Geboren am 27. November 1969 in Ishewsk (USSR)

Gutachter: Prof. Dr. rer. nat. Jürgen Reif

Gutachter: Prof. Dr. rer. nat. Michael Bestehorn

Gutachter: Prof. Dr. rer. nat. Stephane Vallete

Tag der mündlichen Prüfung: 06. November 2013

Bibliografische Information der Deutschen Nationalbibliothek
Die Deutsche Nationalbibliothek verzeichnet diese Publikation in der Deutschen Nationalbibliografie; detaillierte bibliografische Daten sind im Internet über http://dnb.d-nb.de abrufbar.
1. Aufl. - Göttingen : Cuvillier, 2014
Zugl.: (TU) Cottbus, Univ., Diss., 2013

978-3-95404-604-1

© CUVILLIER VERLAG, Göttingen 2014
Nonnenstieg 8, 37075 Göttingen
Telefon: 0551-54724-0
Telefax: 0551-54724-21
www.cuvillier.de

Alle Rechte vorbehalten. Ohne ausdrückliche Genehmigung des Verlages ist es nicht gestattet, das Buch oder Teile daraus auf fotomechanischem Weg (Fotokopie, Mikrokopie) zu vervielfältigen.
1. Auflage, 2014
Gedruckt auf umweltfreundlichem, säurefreiem Papier aus nachhaltiger Forstwirtschaft.

978-3-95404-604-1

Abstract

The phenomenon of laser-induced periodic surface structures (LIPSS), or ripples, generated by near-infrared radiation with the central wavelength around 800 nanometer ($\lambda_{laser} \approx 800$ nm) and pulse duration about of 100 femtosecond ($\tau_{pulse} \approx 100$ fs) on solid targets is considered in this dissertation.

The main aim of the work is a better understanding of the fundamental processes of laser-matter interaction resulting in pattern formation by femtosecond (fs) laser ablation. The problem is of great interest both in fundamental and applied science. The knowledge of the underlying physical mechanisms will provide the opportunity to control surface nanostructuring, which has a big application potential in many modern technologies.

Femtosecond LIPSS observed at the bottom of ablation crater reveal a large variety of features including nanostructures with periods below 100 nm. Moreover, the ripple size depends mainly on the irradiation dose/absorbed laser energy and is rather insensitive to the variation of laser wavelength or incidence angle [CHR02]. The orientation of the structures is dictated by laser polarization. All these experimental observations and an astounding similarity of the structures to other patterns originating from instabilities led to the idea to attribute the femtosecond laser nanostructuring to a self-organized pattern formation from laser-induced surface instability [HVW99], [RCB06].

In this dissertation, surface pattern formation upon femtosecond laser ablation is considered in the framework of an adopted surface erosion model, based on the description of spontaneous pattern formation on surfaces bombarded with high-energy ions. We exploit the similarity to ion-beam sputtering and extend a corresponding model for laser ablation by including laser polarization. It has been found that an asymmetry in the deposition and dissipation of the incident laser energy, related to the laser polarization, results in a corresponding dependence of coefficients in a nonlinear equation of the Kuramoto-Sivashinsky type. The surface morphologies calculated in the framework of this model for different configurations of the incident laser electric field show an excellent qualitative agreement with structures observed in ultra-short pulse ablation experiments.

In this work, properties of the periodic surface structures induced upon femtosecond laser ablation are studied in detail, focusing on a systematic investigation of the main control parameters regulating the pattern formation process. The results support the non-linear self-organization mechanism of pattern formation from laser-induced surface instability.

Keywords: Femtosecond laser ablation, ripples, self-organized pattern formation, laser-induced surface patterning.

Abstrakt

Diese Dissertation beschäftigt sich mit dem Phänomen der Laser-Induzierten Periodischen Oberflächenstrukturen (LIPSS, Ripples), erzeugt bei der Ablation durch ultrakurze Lichtimpulsen mit ≈100 fs Dauer ($\tau_{Puls} \approx 100$ fs) und einer Wellenlänge von 800 nm ($\lambda_{Laser} \approx 800$ nm) an unterschiedlichen Targetmaterialien.

Das wesentliche Ziel der Arbeit bestand darin, die fundamentale Physik der Oberflächenstrukturierung bei der Femtosekundenlaserablation besser zu verstehen. Das Problem ist von großer Bedeutung sowohl für die Grundlagenforschung als auch in der angewandten Wissenschaft. Die Kenntnis der physikalischen Mechanismen hilft, die Nanostrukturierung von Oberflächen zu kontrollieren, die ein großes Anwendungspotenzial in vielen modernen Technologien bietet.

Femtosekunden LIPSS am Boden des Ablationskraters präsentieren eine große Vielfalt von Strukturen bis hin zu einer Periodizität kleiner als 100 nm. Die Größe der Strukturen hängt hauptsächlich von der Bestrahlungsdosis/absorbierten Laserenergie ab, und ist nicht von der Wellenlänge oder dem Einfallswinkel des Laserstrahls beeinflusst. Die Orientierung der Ripples ist mit der Polarisation der Laserpulse verknüpft. Alle diese experimentelle Beobachtungen und eine erstaunliche Ähnlichkeit der Strukturen zu anderen Mustern, die aus Instabilitäten entstehen, haben zur Idee geführt, die Entwicklung der Nanostrukturen im Rahmen einer Oberflächenselbstorganisation aus einer laserinduzierten Instabilität zu erklären.

In der Arbeit wird die Entwicklung der periodischen Oberflächenstrukturen bei Femtosekundenlaserablation im Rahmen eines adoptierten Oberflächenerosionsmodels betrachtet. Unser theoretischer Ansatz basiert auf dem Modell für die Entwicklung von selbstorganisierten Oberflächenstrukturen beim hochenergetischen Ionenstrahl-Sputtern. Unsere Erweiterung des Modells berücksichtigt den Einfluss polarisierter Laserstrahlung. Es wird gezeigt, dass die Laserpolarisation eine Asymmetrie in der Verteilung der absorbierten Laserenergie verursachen kann, die auf eine entsprechende Abhängigkeit von Koeffizienten in einer Kuramoto-Sivashinsky Gleichung hinausläuft. Die numerisch berechneten Oberflächenmorphologien zeigen eine ausgezeichnete qualitative Übereinstimmung mit dem Experiment.

Das experimentelle Teil der Dissertation präsentiert eine detaillierte Messung der Eigenschaften der laserinduzierten periodischen Oberflächenstrukturen. Der Schwerpunkt der Arbeit lag in der Untersuchung der Parameter die kontrollieren die Bildung/Entwicklung der Nanostrukturen. Die zahlreiche Daten aus Ablations-Experimenten unterstützen den nichtlinearen Charakter der Selbstorganisation bei der laser-induzierten Strukturbildung.

Schlagwörter: Femtosekundenlaserablation, Ripples, selbstorganisierte Strukturbildung, laser-induzierte Oberflächenstrukturierung.

Table of contents

List of publications

This dissertation is based on the published works:

O. Varlamova, F Costache, J. Reif, M Bestehorn; *„Self-organized pattern formation upon femtosecond laser ablation by circularly polarized light"*, Appl. Surf. Sci. (2006) 252, 4702.

J. Reif, M. Ratzke, O. Varlamova, F. Costache; *„Electrical properties of laser-ablation-initiated self-organized nanostructures on silicon surface"*, Mat. Sci. and Eng. B (2006) 134, 114.

O. Varlamova, F. Costache, M Ratzke, J. Reif; *„Control parameters in pattern formation upon femtosecond laser ablation"*, Appl. Surf. Sci. (2007) 253,7932.

J. Reif, O. Varlamova, F. Costache; *„Femtosecond laser induced nanostructure formation: self-organization control parameters"*, Appl. Phys. A (2008) 92, 1019.

J. Reif, F. Costache, O. Varlamova, G. Jia, M. Ratzke; *„Self‐organized regular surface patterning by pulsed laser ablation"*, Physica Status Solidi C (2009) 6, 681.

S. Varlamov, M. Bestehorn, O. Varlamova, J. Reif; *„The laser polarization as control parameter in the pattern formation"* arXiv:0902.4374 (2009).

O. Varlamova, M. Ratzke, J. Reif; *„Feedback effect on the self-organized nanostructures formation on Silicon upon femtosecond laser ablation"*, Sol. St. Phen. (2010) 156, 535.

M. Schade, O. Varlamova, J. Reif, H. Blumtritt, W. Erfurth, H.S. Leipner; *„High-resolution investigations of ripple structures formed by femtosecond laser irradiation of silicon"*, Anal. Bioanal. Chem. (2010) 396, 1905.

J. Reif, O. Varlamova, M. Ratzke, M. Schade, H.S. Leipner, T. Arguirov; *„Multipulse feedback in self-organized ripples formation upon femtosecond laser ablation from silicon"* Appl. Phys. A (2010) 101, 361.

J. Reif, O. Varlamova, M. Bounhalli, T. Arguirov, M. Schade, H.S. Leipner; *„Long-time feedback in selforganized nanostructures formation upon multipulse femtosecond laser ablation”* Proc. SPIE (2010), pp. 75860H-75860H.

O. Varlamova, J. Reif, S. Varlamov, M. Bestehorn; *„The laser polarization as control parameter in the formation of laser-induced periodic surface structures: Comparison of numerical and experimental results”*, Appl. Surf. Sci. (2011) 257, 5465.

O. Varlamova, S. Varlamov, M. Bestehorn, J. Reif; *"The Role of Anisotropic Excitation in Self-organized Nanostructure Formation upon Femtosecond Laser Ablation" Session 2A2 Laser-induced Periodic Surface Nanostructures: Fundamental Fabrication Mechanisms, Nanoscale-dominated Physical and Chemical Properties*: 240 (Proc. of LPM 2011).

O. Varlamova, J. Reif, S. Varlamov, M. Bestehorn; *„Modeling of the Laser Polarization as Control Parameter in Self-Organized Surface Pattern“* Journal of Nanoscience and Nanotechnology (2011) **11**, 9274.

J. Reif, O. Varlamova, M. Bounhalli, M. Muth, T. Arguirov; *„Nanostructure formation upon femtosecond ablation from silicon: Effect of double pulses”* Appl. Surf. Sci. (2012) 258, 9491.

O. Varlamova, M. Bounhalli, J. Reif; *„Influence of Irradiation Dose on Laser-Induced Surface Nanostructures on Silicon”* Appl. Surf. Sci. (2012) 278, 62.

O. Varlamova, J. Reif, S. Varlamov, M. Bestehorn; *„Self-organized surface pattern originating from laser-induced instability”* Chapter in book, Springer (2013), in print.

Introduction

Laser-induced periodic surface structures were detected in early experiments on laser application [Bir65] and have been studied experimentally ever since. The first widely accepted theoretical approach [EHW73], [SYP83] describing LIPSS suggested that the structures are the result of an interference of the incoming laser beam with some form of a surface-scattered electromagnetic wave traveling along the surface. The interference theory accounted well for a dependence of the ripples' orientation on the laser polarization. Also the cumulative effect of the laser irradiation has been taken into account by this model [YPD83], [YSD84]. In general, this theory was successful in the description of uniformly distributed patterns with the periodicity dependent on the laser wavelength and on the angle of incidence [Bir65], [SKK73], [EHW73], [YPD83], [YSD84], [BoH03] observed under long-pulse (ns) irradiation.

The application of femtosecond laser pulses, however, has revealed a large, much more complex diversity of patterns at the modified surface region. Such micro- and nanostructured areas exhibit surprising novel optical and mechanical properties, which offer a great potential application in various modern technologies. For instance, direct laser writing [KST01], special wettability (so-called "lotus-effect") [GrM06], [ZPP06], controllable reflectance of metals [VoG08], color marking [DSS09], as well as producing of "black silicon" [SKI08] are based on the ability of femtosecond laser to precise non-thermal material modifications.

Arrays of periodic linear structures with many bifurcations and with periods substantially shorter than the applied laser wavelength were reported in numerous publications of the end the 90s and beginning of the 2000s, some of them cited here [VWR98], [BSS00], [CHR02], [SKS05]. Their orientation and shape were generally dictated by polarization of the incident laser beam [RCH02], [CKR04], [MiM07], [DRD09], [BRK09]. Numerous experimental data have shown that usually the ripples completely develop only after a considerable number of pulses [BSS00], [BBK02], [BBM04], [CHR02], [CHR03], [BoK10], and that positive feedback plays an important role in the structure formation process [Rei09], [BoK10]. These peculiar features of "femtosecond ripples" do not comply with the "classical ripples theory" based on a locally modulated energy input due to the interference effect [EHW73], [SYP83], [YPD83], [YSD84]. The ripples exhibit non-trivial surface morphology, sharing many similarities with other self-organized patterns originating from instabilities [MiV03], [TBL98], [EAC99]. The periodicity seems to be insensible to the laser wavelength and incident angle, but it is correlated with the local intensity of

the laser beam [CHR02], [KRD05]. Formation mechanisms of laser-generated ripples and the underlying microscopic processes are still discussed.

Several years ago, taking into account all these facts and the strong nonequilibrium conditions of femtosecond laser ablation, self-organized pattern formation from the laser-induced surface instability was proposed by J. Reif and M. Bestehorn [HVW99], [CHR02], [RCB06] as a possible scenario for femtosecond ripples.

A systematic study on the surface nanostructuring upon femtosecond laser ablation is presented in this work. The various experimental parameters that control surface morphologies are investigated. The effect of laser polarization, an irradiation dose, surface defects and an important role of a multipulse feedback in structure formation are analyzed, based on a statistical evaluation of numerous experimental data. To gain more information about possible microscopic mechanisms of the ripples' formation, the thorough surface investigation of structured samples was also supplemented by a cross-sectional analysis and electrical measurements.

The dissertation is organized as follows:

The first chapter considers the fundamental mechanisms of the ultra-short pulsed laser-matter interaction that is characterized by a nonequilibrium nature of the processes. For various target materials, different microscopic mechanisms for absorption and dissipation of the laser energy, resulting in the macroscopic material removal/ablation, are discussed.

Results of the experimental and theoretical studies on laser-induced periodic surface structures are briefly reviewed in the second chapter. Here, special attention is paid to the peculiar features of the femtosecond LIPSS that cannot be explained by a widely accepted classical approach attributing ripple formation to an inhomogeneous energy deposition due to optical interference. Based on the critical analysis of existing theoretical studies, surface self-organization from laser-induced instability is proposed as the possible origin mechanism for femtosecond nanostructuring. According to this approach, femtosecond nanostructures arise from laser-induced surface erosion counterbalanced by thermal self-diffusion.

In the third chapter, an adopted surface erosion model for pattern formation upon femtosecond pulsed laser ablation is introduced. The dependence of generated patterns on the incident laser electric field is taken into account. The approach is based on the description of surface pattering by an energetic ion beam. The surface morphologies obtained in the framework of this model for different polarization directions and time periods are in excellent agreement with experimental results.

Representation of the experimental results of the dissertation begins with the fourth chapter. At the beginning, the brief review of technique and procedure of laser ablation experiments and the subsequent investigation of the structured samples is given.

Experimental studies of the parameters controlling the self-organized pattern formation process are presented in the fifth chapter. Laser polarization and the incidence angle of the laser beam, irradiation dose and surface defects, as well as a multipulse feedback effect are the focus of this chapter.

The sixth chapter is devoted to the in-depth investigations of the laser-modified silicon. The intrinsic modifications of the irradiated material, which indicate a very fast non-thermal surface relaxation from a highly nonequilibrium state, give strong support to the conception of self-organization from laser-induced instability as the origin of ripples.

General conclusions and outlook are given in the last chapter. Ripples generated on different target materials are compared. Control parameters common for dielectrics, semiconductors and metals as well as the similarity in shape and the size of the laser-induced morphologies confirm a universal mechanism of structuring, which is consistent with self-organization.

1. Laser ablation and laser-induced surface instability

1.1. General aspects of pulsed laser ablation

Laser ablation denotes, by definition, the removal of macroscopic amounts of matter from the surface of condensed matter upon intense − usually pulsed − laser irradiation. It is, commonly, characterized by a threshold fluence below which only desorption of individual particles is observed, without any noticeable surface modification. Since the laser is coupled to the target's electronic system, the ablation yield strictly depends on the electronic excitation density [Mil94] but follow-up processes such as excitation dissipation, thermal material response (melting, evaporation) and other material removal processes (direct electronic bond breaking [Bae96], [Sri86], phase explosion [MiK95], Coulomb explosion [Rei89], [HWR00], [SRA02] play an important role. In a general scheme (Fig. 1.1), the complex process chain from laser impact to ablation can be summarized [Bae96].

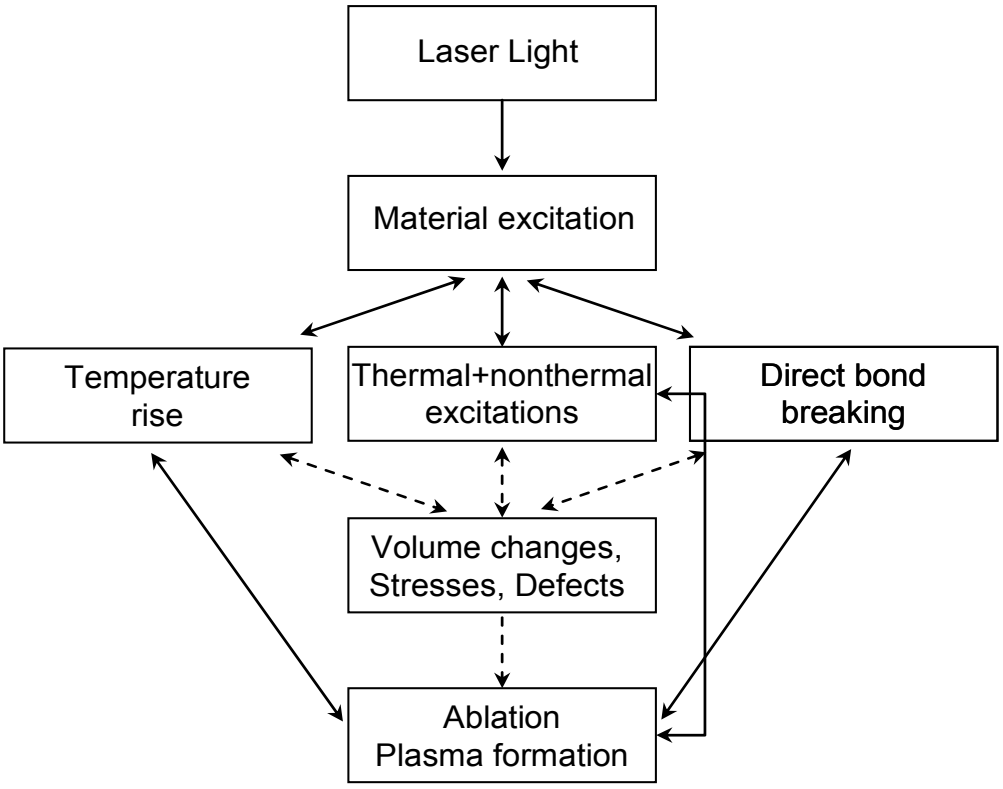

Fig. 1.1: Laser-matter interaction and feedback mechanisms during ablation. Different scenarios are possible: thermally activated ablation (left path), non-thermal photochemical ablation (right), and a combination of both (at the middle), (after [Bae96]).

After the material excitation by the incident laser pulse, one can distinguish, in principle, three main scenarios: (1) the deposited energy is completely transferred into

heat, (2) the absorbed laser light results in direct photochemical bond breaking, or (3) a combination of non-thermal bond breaking and thermal excitation is induced. All three dissipation channels can lead to direct material removal, e.g. by expulsion or melting/evaporation, respectively sublimation. Another possibility is an indirect process where, in an intermediate step, the material is first modified and only subsequent pulses remove this modified material. Both material removal and material modification can influence, in turn, the optical, thermal, and mechanical material properties and thus have a positive or negative feedback on subsequent excitation, dissipation and ablation processes.

This chapter will be mainly addressed to the fundamental mechanisms of interaction of an ultrashort pulsed laser irradiation of different targets (dielectric, semiconducting and metallic). When such short pulses (duration about 100 fs) are involved, additional particular features, such as temporal separation of laser excitation and massive particles emission, have to be considered in the ablation dynamics.

1.2. Electronic excitation

Laser ablation of materials starts with energy deposition in the electronic subsystem of a target through linear and non-linear absorption that leads to a high density of hot electrons in the conduction band. While in nonmetallic targets the free electron density increases during the pulse due to intraband transitions, in metals the density hardly changes, but the kinetic energy of free electrons drastically grows. A detailed picture of these effects will be presented in the next paragraphs.

1.2.1. Nonlinear absorption/ionization in *dielectrics*

When an intensive laser beam with photon energy less than the band gap of the material ($\hbar\omega << E_{gap}$) impinges on the surface of a transparent target, absorption and free electron generation in the conduction band can occur only through nonlinear processes such as multiphoton- or impact ionization [Kel65], [SKB77], [Rei89], [Blo74], [RSL04].

A first theoretical analysis of ionization of atoms in a strong light field was performed by Keldysh [Kel65]. He obtained the general equation for the photoionization probability, where, depending on the laser frequency and laser intensity, multiphoton and tunneling ionization can be considered as two limiting cases of the general solution. According to this theory [Kel65], the ionization probability for different processes is given by the parameter γ that is determined as the ratio between the frequency of laser light, ω, and the frequency ω_t of electrons tunneling through a potential barrier:

$$\gamma = \frac{\omega}{\omega_t} = \frac{\omega\sqrt{2m^*\varepsilon_i}}{eE}, \tag{1.1}$$

where E describes the laser electric field; ε_i denotes ionization energy of an atom; e is electron charge and $m^* = \frac{m_C m_V}{m_C + m_V}$ is the electron's reduced effective mass, with m_C and m_V the effective mass of the electrons in the conduction and valence band, respectively.

From Keldysh's approach [Kel65] it follows that at high laser frequencies ($\gamma >> 0$), multiphoton ionization (MPI) is the dominant mechanism of free electron generation. The probability P of MPI is correlated with the laser intensity I by the power law [Del75]:

$$P = \sigma^{(n)}(I) I^n, \tag{1.2}$$

where index n is the order of the multiphoton process, which shows how many photons will be absorbed by an electron in one elementary excitation act; and $\sigma^{(n)}(I)$ is the macroscopic absorption cross section that depends on the laser intensity for a strong incident laser field [Rei09].

The electron transition into a free state is accomplished by simultaneous absorption of n photons (process I in Fig. 1.3 (a)), in which total energy E_{abs} should be equal or exceed the band-gap energy and is given by [Rei89], [BeG66]:

$$E_{abs} = \sigma^{(n)} I^n \tau_{pulse} = \sigma^{(n)} I^{n-1} F, \tag{1.3}$$

where F is the laser fluence and τ_{pulse} is the laser pulse duration. The process can additionally be enhanced by localized defect states within the band gap (process II in Fig. 1.3 (a)). The resultant number of extracted electrons, or electron yield Y_{el}, is also proportional to the laser intensity I and follows the power low [Rei89], [BeG66]:

$$Y_{el} \propto I^n. \tag{1.4}$$

Indeed, the power law dependence of the electron yield Y_{el} on the laser intensity I (1.4) is in good agreement with data of time-of-flight mass spectra taken upon ablation of different wide band gap dielectrics [RCE04], [Cos07]. The slopes of the linear functions in Fig. 1.2 indicate a nonlinear ionization process, but the nonlinearity may

be less than expected from the band gap. The phenomenon can be explained by laser induced localized or transient defect states within the band gap [Rei89]. As shown in the insert in the Al_2O_3 panel (Fig. 1.2), localized energy states within the band gap, e.g. due to formation of an F-center (an anion vacancy), may act as intermediate resonances and reduce the order of nonlinearity [Rei09].

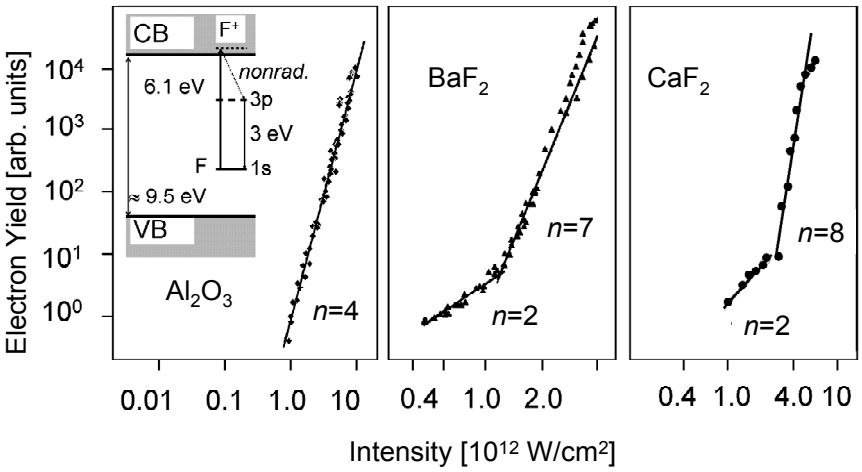

Fig. 1.2: Double logarithmic plot of electron yield as a function of laser intensity after irradiation with laser pulses at photon energy 1.55 eV of three different dielectric targets: Al_2O_3 ($E_{gap} \approx 9.5$ eV [ArW68]), BaF_2 ($E_{gap} \approx 10.5$ eV [KKR87]), and CaF_2 ($E_{gap} \approx 12$ eV [Rub71]). The slopes of the linear functions suggest *n*-photon absorption. The insert in the Al_2O_3 panel shows, schematically, the band-structure (VB: valence band and CB: conduction band) and the energy levels of a localized F-center with a 1s ground state, a 3p excited state, and the ionized F^+-center energy in the conduction band. (after [Rei09])

In the other limiting case $\gamma \ll 1$, corresponding to low irradiation frequencies or very strong laser fields ($E \sim 200$ MV/cm), tunneling of an atomic electron through a potential barrier under the action of an external electric field is reported to be main scenario for free electron generation [Kel65]. Here the ionization probability P depends exponentially on the laser electric field E [Del75]:

$$P = \frac{b}{\sqrt{E}} \exp\left(-\frac{c}{E}\right), \tag{1.5}$$

where b and c are constants and the exponential has a well known expression for the tunnel auto-ionization of atoms in a constant electric field [LaLd87].

In contrast to multiphoton and tunneling ionization, where the transition of electrons from the valence band to the conduction band is assisted by the laser electric field, Auger-like impact ionization is caused by already existing free electrons in the

conduction band. Those can be provided, for instance, by ionized defect states [Cos07] or by photoionization [Kel65]. As shown in Fig. 1.3 (b), the conduction band electrons gain additional energy in the laser field via inverse Bremsstrahlung (step I). If its kinetic energy is sufficiently large, part of this energy can be transferred in an Auger-like process to a valence band electron (step II), thus exciting it to the conduction band (step III) [Blo74]. The impact ionization may even result to an electron avalanche.

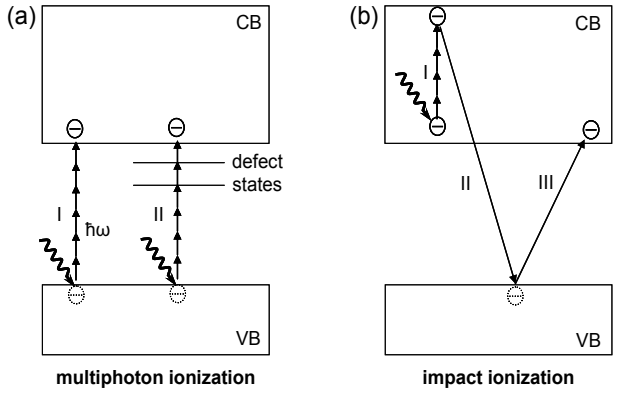

Fig. 1.3: Ionization mechanisms in wide band-gap dielectrics: (a) multiphoton absorption across the band gap (I) and resonance enhancement by defect states (II); (b) impact ionization: a conduction band electron gains additional energy in the laser field via inverse Bremsstrahlung (I), after that it transfers its kinetic energy to a valence band electron (II), thus exciting it to the conduction band (III).

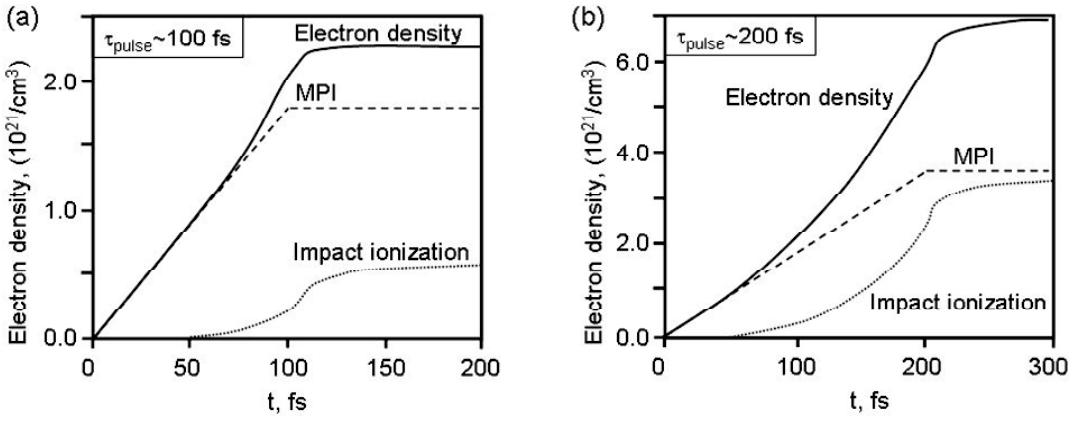

Fig. 1.4: Temporal dynamics of free electron density in the conduction band of an insulator irradiated with a laser pulse of (a) 100 fs and (b) 200 fs duration (E_{laser}=150 MV/cm). The total free electron density (solid line) is a sum of electron density produced by multiphoton ionization only (dashed line) and by impact ionization (dotted line) [KRV00]).

Considering microscopic interaction mechanisms of ultrashort laser irradiation with dielectrics and taking into account conservation of energy and momentum, Kaiser *et. al*. calculated the contribution of different ionization processes to the laser generated free electron density [KRV00]. Numerical results for a 100 fs laser pulse are

presented in Fig. 1.4 (a): while multiphoton ionization starts immediately with the beginning of the irradiation and increases linearly during the pulse, the impact/avalanche ionization is activated much later and its contribution to the electron density is not significant in comparison to the MPI. The authors [KRV00] found that only for pulse duration $\tau_{pulse} \geq 200$ fs, the density of impact electrons may become comparable to the MPI contribution (Fig. 1.4 (b)).

1.2.2. Absorption of laser irradiation in *silicon*

When laser radiation with energy $\hbar\omega$ slightly above the bandgap width E_{gap} interacts with silicon (Si), light is absorbed by the electronic system via interband linear or nonlinear (two- or more-photon) absorption that results in the generation of electron-hole (*e*-*h*) pairs. Intraband free carrier absorption (inverse Bremsstrahlung) is also possible, but it is, mainly, a secondary process, because it depends on the number of already existing carriers. Moreover, the process becomes important for Si only for the longer laser pulses or at the shorter wavelength [PVH98].

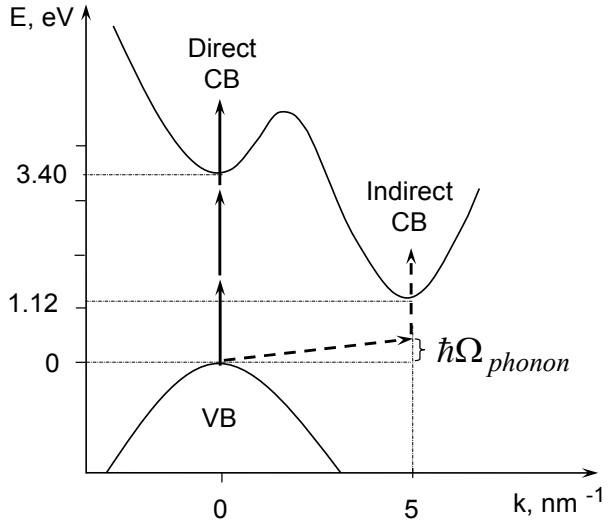

Fig. 1.5: Simplified energy diagram of electronic transitions in silicon upon irradiation with near-IR ultrashort laser pulses (E_{photon}=1.5 eV) of 100 fs duration. Direct and indirect electron transitions across the bandgap of silicon are shown with arrows.

To illustrate the possible absorption mechanisms in silicon after excitation at ~800 nm (E_{photon}=1.55 eV) with 100-fs laser pulses, the simplified energy band diagram is represented in Fig. 1.5. The energy is chosen to be zero at the edge of the valence band (VB). The direct conduction band (CB) minimum at $k = 0$ nm^{-1} occurs at 3.40 eV, and the indirect CB minimum ($k = 5$ nm^{-1}) is equal at 1.12 eV. For laser irradiation (E_{photon}=1.55 eV) at an intensity near the single-shot ablation threshold

[BBK02], the initial electronic excitation can occur through the indirect CB by one-photon absorption (dashed arrows in Fig. 1.5), which involves a phonon to satisfy momentum conservation. Along with the indirect band-band excitation, the direct transition from valence to conduction band ($E_{gap} \approx 3.40$ eV) [Sin93] is also possible by simultaneous absorption of three photons.

For a near-IR ultrashort laser pulse, it is assumed that absorption of the leading edge occurs at the depth about of $\alpha^{-1} \sim 10$ μm, where α is the optical absorption coefficient, and the rest of the pulse can be absorbed only in a shallow surface layer (0.1-0.2 μm) due to generation of a dense electron-hole (*e-h*) plasma at the surface region. This modeling is based on changes in optical reflectivity of a Si surface irradiated with 100-fs laser pulses at 625 nm, reported by Sokolowski-Tinten and von der Linde [SoL00]. In this work it has been shown that for a wide range of fluencies (up to 0.4 J/cm²), multiphoton absorption is the main mechanism of the electron-hole plasma formation, but also higher orders of nonlinearity are possible. Further, they estimated that the maximal density of the laser generated plasma can be over 10^{22} cm^3.

It is necessary to note here that such high concentration of *e-h* pairs [SoL00] can probably be expected only in the volume of the target, whereas the surface shallow layer will be considerably depleted due to appreciable emission of photoelectrons. The total electron yield in Si irradiated with 800 nm laser pulses, estimated numerically by Choi *et al.* [ChG02], can reach 10^{20} cm^{-2}. Moreover, numerous time-of-flight measurements have revealed that a substantial number of electrons instantaneously leave the surface upon femtosecond laser pulsed irradiation already at intensities well below the ablation threshold [Cos07]. These facts show that the important question concerning the real density of the fs-laser-induced plasma at the sample surface is still open.

1.2.3. Absorption of laser energy in *metals*

Generally, metals are modeled as a periodic crystal lattice of metallic ions with electrons free-moving in the self-consistent potential field that takes into account all electron-electron and electron-ion interactions [AsM76]. By irradiation of a metal with laser light, conduction electrons may absorb the laser energy through inverse Bremsstrahlung. When the absorbed energy exceeds the work function W of the metal, the electron can leave the surface as shown in Fig. 1.6 (a). From Fig. 1.6 (b), the work function W is given by

$$W = \Delta\phi - \mu, \tag{1.6}$$

where $\Delta\phi$ is an electronic potential difference across the surface layer and μ is the chemical potential of the electrons in bulk [LaL71].

In the case of ultrashort laser excitation the pulse width is short enough to excite only the electron system, while the lattice remains cold. During the pulse (100 fs) the excited electron system will be thermalized by electron-electron collisions that lead to a Fermi gas with the internal energy determined by the absorbed laser energy. The energy transfer from the hot electron gas to the lattice occurs by electron-phonon coupling. Though the electron-phonon coupling time $\tau_{e\text{-}ph}$ may be comparable with the electron-electron collision time τ_{ee} [RKV02], the energy transfer from the excited electron system to the cold lattice will take much longer (typically a few tens of picoseconds) due to the large mass difference between electrons and ions [FLI84], [Ani95]. One can confirm that femtosecond laser excitation generates a hot electron gas being in transient nonequilibrium with the lattice. Further energy evolution in the system is described in the framework of the *Two-temperature model* [AKP74] in the next chapter.

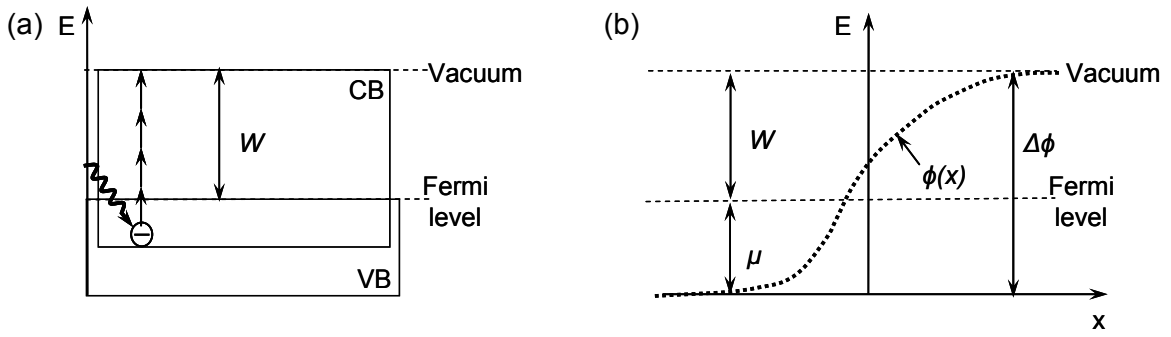

Fig. 1.6: Schematic representation of (a) electron emission from a metal due to absorption of several photons; (b) energy levels relevant to the determination of the work function.

The electron emission under 100-fs laser pulses ($\hbar\omega < W$) occurs either through the multiphoton photoelectric effect [ABF77], or by thermionic emission [AAM88], or through thermally assisted photoemission [ABF77], where the thermally excited electrons can further absorb laser energy and escape the surface. (Fig. 1.7).

The multiphoton assisted emission starts immediately with the incoming laser pulse and the electron yield Y_{el} is proportional to the intensity of the incident irradiation (see Eq. (1.4)). Moreover, the photoelectric current depends strongly on the laser electric field component, which is normal to the surface, as well as on the angle of incidence and on the polarization of light [ABF77]. The decay of the signal is determined by the electron-phonon coupling time $\tau_{e\text{-}ph}$. The maximum energy of the

emitted photoelectrons E_{max} is independent on the laser intensity and proportional to the number n of absorbed photons of energy $\hbar\omega$ [ABF77]:

$$E_{\max} = n\hbar\omega - W\,, \tag{1.7}$$

where W is the work function.

Photo-assisted emission of hot electrons is followed by thermionic emission, which is delayed relative to the laser pulse by $\tau \approx c_e/\alpha \sim 10^{-12}$ s, where c_e is the specific heat capacity of the electronic subsystem and α is the parameter characterizing the electron-phonon coupling constant [FLI84]. The shape of the thermionic signal and the decay are determined by the thermal properties of the target material, and the number of extracted electrons is governed entirely by the target temperature T [MuG56]:

$$Y_{el} \propto T^2 \exp(-1/T). \tag{1.8}$$

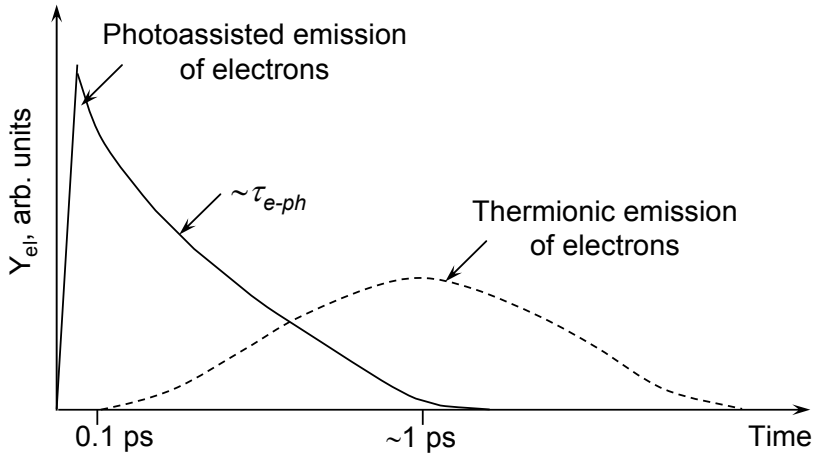

Fig. 1.7: Possible origins of the electron emission from a metal exposed to ultrashort laser irradiation. The decay of the photoemission signal depends on the electron-phonon coupling time $\tau_{e\text{-}ph}$.

1.2.4. Ultrafast excitation/nonequilibrium

In this subsection, we consider microscopic excitation mechanisms upon irradiation with femtosecond pulses at fluencies below the single-shot ablation threshold for dielectrics and around the ablation threshold for semiconductors and metals.

It has been shown that the initial laser-matter interaction consists of a very strong excitation of the electronic subsystem, where the crystal lattice remains almost unaffected. The absorbed laser energy is distributed among the electrons through electron-electron collisions. Thermalization of the electronic system depends on both

the material properties and laser fluence. In metals irradiated by laser fluencies around the ablation threshold, the hot electron gas can be considered as thermalized on a femtosecond time scale ($\approx 10^{-14}$-10^{-13} s) [RKV02], whereas in dielectrics, electron thermalization can last up to several picoseconds [KRV00].

Due to laser-induced thermal nonequilibrium ($T_e >> T_i$.), electrons are uncoupled from the lattice and the electron-lattice system becomes unstable. The degree of instability can be very high because of the small heat capacity of electrons in comparison to that of the lattice [Ani95]. The further energy transfer from hot electrons to the lattice is characterized by the electron-phonon coupling and takes about a few picoseconds due to the large ion-to-electron mass ratio [SLF87].

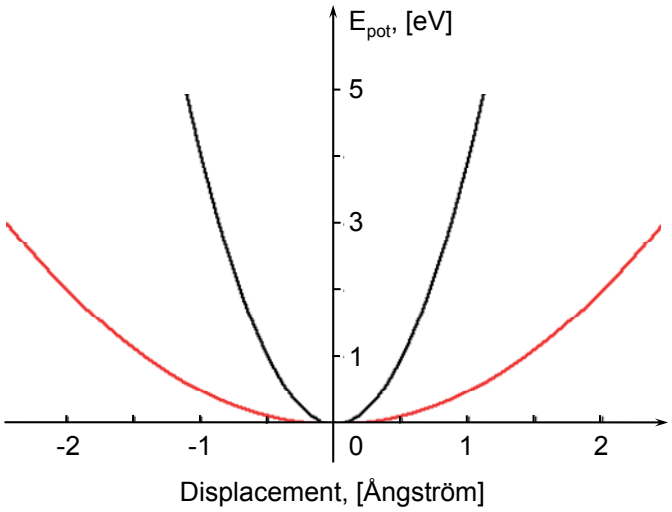

Fig. 1.8: Changes in the interatomic potential of semiconductor materials upon intense femtosecond laser excitation. Black curve refers to the unperturbed state, and red curve refers to t=200 fs after excitation (after [LLS05])

In semiconductors, Lindenberg *et al.* [LLS05] reported the ultrafast changes in the crystalline material irradiated with intense femtosecond laser pulses. Despite of the large lattice displacement that induces, correspondingly, the strong modification of atomic potential (see red curve in Fig. 1.8); the averaged displacement of atoms from the equilibrium lattice sites is still zero. It means that for the first few hundred femtoseconds after excitation, the crystal lattice is very strong perturbed and unstable, but the system still retains the symmetry, reflecting the initial crystalline state. Recently, the first direct measurements of the ultrafast atomic dynamics during the femtosecond ablation process in semiconductors confirmed that the strong laser-induced instability relaxes via non-thermal explosion-driven processes [LEG08].

1.2.4.1. Two-temperature model

The first theoretical approach, well-known as the *Two-temperature model*, describing evolution of material exposed to intense pulsed laser irradiation, was proposed by Anisimov *et al*. [AKP74], [Ani95], [AnL02]. Assuming that the thermalization time within the electronic subsystem is much shorter than the electron-lattice coupling [SLF87], [Wan94], [RKV02], they characterized the excited electrons and the cold ion lattice by two different temperatures T_e and T_i, respectively. This classical description is based on the assumption of thermal equilibrium within the electron and lattice subsystems independently, and describes the energy transfer inside the material with the following one-dimensional, coupled heat conduction equations:

$$\begin{aligned} C_e \frac{\partial T_e}{\partial t} &= \frac{k_e \partial^2 T_e}{\partial z^2} - \gamma\left(T_e - T_i\right) + Q \\ C_i \frac{\partial T_i}{\partial t} &= \frac{k_i \partial^2 T_i}{\partial z^2} + \gamma\left(T_e - T_i\right) \end{aligned}, \qquad (1.9)$$

where z is the direction perpendicular to the target surface; $C_{e/i}$ and $k_{e/i}$ are the heat capacities per unit volume and thermal conductivities of the electrons and lattice, respectively; γ is the parameter characterizing the electron-lattice coupling [AKP74], [Ani95]; Q is the source term that describes the absorption of the laser energy by electrons. The source term depends on the laser intensity, $I(t)$; on the surface absorptivity of the material, A = 1- R, where R is the reflection coefficient; and on the material absorption coefficient, α. When the laser beam travels along z-axis and the surface is located at $z = 0$, it takes the form:

$$Q = I(t) A \alpha \exp(-\alpha \cdot z) \qquad (1.10)$$

Considering the electron energy, $k_B T_e \sim 1$ eV [Wan94], smaller than the Fermi energy, E_F, we assume that, first, the electron heat capacity, C_e, is a linear function of the electron temperature, T_e, given by $C_e = \widetilde{C}_e T_e$ (here $\widetilde{C}_e$ is a constant), and, secondly, the electron thermal conductivity, k_e, in the nonequilibrium two-temperature system is taken as $k_e = k_0(T_i)\frac{T_e}{T_i}$, where $k_0(T_i)$ is the conventional equilibrium thermal conductivity of the material [AsM76].

Two characteristic times are included in the model (1.9): the electron-phonon coupling time, $\tau_{e\text{-}ph} = C_e/\gamma$; and the lattice heating time, $\tau_i = C_i/\gamma$, which is attributed to

thermal conductivity of the sample. Thermalization within the electronic subsystem is assumed to be on a time scale shorter than the laser pulse [AAM88].

For greater specificity we restrict ourselves to interaction of an ultrashort laser pulse (τ_{pulse} ~ 100 fs) at low intensity with a metallic target. For this case, when the laser pulse duration is shorter than the electron-phonon coupling time, ($\tau_{pulse} << \tau_{e\text{-}ph}$), the set of equations (1.9) can be considerably simplified.

For time interval $t << \tau_{e\text{-}ph}$, the electron lattice energy exchange terms can be ignored in both equations (1.9). The next simplification, namely, neglecting of the electron heat conduction term in the first equation, can be done when the following condition for the electron thermal diffusivity, $D_e = k_e / C_e$, is satisfied $D_e \tau_{pulse} < \alpha^{-2}$ [CMN96]. Further, in the second equation of the system, the phonon heat conduction, $\frac{k_i \partial^2 T_i}{\partial z^2}$, can be omitted, because it is typically negligible in comparison to the electronic heat conduction. Finally, the set of equations (1.9) takes the simple form [AnL02]:

$$\begin{aligned} \widetilde{C}_e T_e \frac{\partial T_e}{\partial t} &= I(t) A \alpha \exp(-\alpha \cdot z) \\ \frac{\partial T_i}{\partial t} &= 0 \end{aligned}, \qquad (1.11)$$

where the second equation indicates that the lattice temperature, T_i, is unaffected during the pulse. Assuming that the incident laser intensity remains constant $I(t) = I_0$, the first equation in (1.11) can be easily solved

$$\frac{\partial T_e^{\,2}}{\partial t} = \frac{2 I_0 A \alpha}{\widetilde{C}_e} \exp(-\alpha \cdot z) \qquad (1.12)$$

and results in

$$T_e(t) = \left[T_0^{\,2} + \frac{2 I_0 A \alpha}{\widetilde{C}_e} t \exp(-\alpha \cdot z) \right]^{1/2}. \qquad (1.13)$$

Here T_0 is the initial electron temperature $T_e(t = 0)$. At the end of the laser pulse, when the inequality $T_e\left(t = \tau_{pulse}\right) >> T_0$ is fulfilled, the electron temperature is given by

$$T_e(\tau_{pulse}) \cong \left[\frac{2I_0 A\alpha}{\widetilde{C}_e}\tau_{pulse}\right]^{1/2} \exp\left(-\frac{\alpha \cdot z}{2}\right), \tag{1.14}$$

where T_0 can be omitted, because it is too small in comparison to $T_e(\tau_{pulse})$. Designating the absorbed laser fluence as $F = I_0 A \tau_{pulse}$ and $\delta = 2/\alpha$ as the skin depth, we obtain (1.14) in the following form:

$$T_e(\tau_{pulse}) \cong \left[\frac{2F\alpha}{\widetilde{C}_e}\right]^{1/2} \exp\left(-\frac{z}{\delta}\right). \tag{1.15}$$

When the laser pulse is off ($t >> \tau_{pulse}$), the temperature dynamics of the electron-lattice system is described by Eq. (1.9) by setting of the laser energy source term to zero, $Q = 0$. The initial electron temperature is determined by Eq. (1.14) and the initial lattice temperature is T_0. The excited electronic system will be thermalized through electron-lattice energy transfer and heat conduction into the bulk. If we take in account the very short electron cooling time, then according to Chichkov *et. al*. [CMN96] the second equation in (1.9) can be written as

$$\frac{\partial T_i}{\partial t} = \frac{1}{\tau_i}(T_e - T_i) \tag{1.16}$$

with the solution

$$T_i \cong \frac{T_e(\tau_{pulse})t}{\tau_i}, \tag{1.17}$$

where the initial lattice temperature, T_0, is neglected. The reachable lattice temperature at time $t > \tau_{pulse}$ depends on the average electron-phonon coupling time $\bar{\tau}_e = \dfrac{\widetilde{C}_e T_e(\tau_{pulse})}{2\gamma}$ [CMN96] and is given in the form:

$$T_i \cong T_e^2(\tau_{pulse})\frac{\widetilde{C}_e}{2C_i} \cong \frac{F\alpha}{C_i}\exp(-\alpha \cdot z), \tag{1.18}$$

where $F = I_0 A \tau_{pulse}$ is the absorbed laser fluence.

The *Two-temperature model* quite accurately describes qualitative aspects of the subpicosecond laser ablation. The results shown in Fig. 1.9 present the dynamics of ultrashort laser pulse interaction with the metals [AnL02]. Here, we see the temperature response of electron and ion subsystems to the laser excitation on a picosecond time scale: while the electron temperature abruptly increases during the laser pulse, the lattice remains almost not affected (see inset in Fig. 1.9).

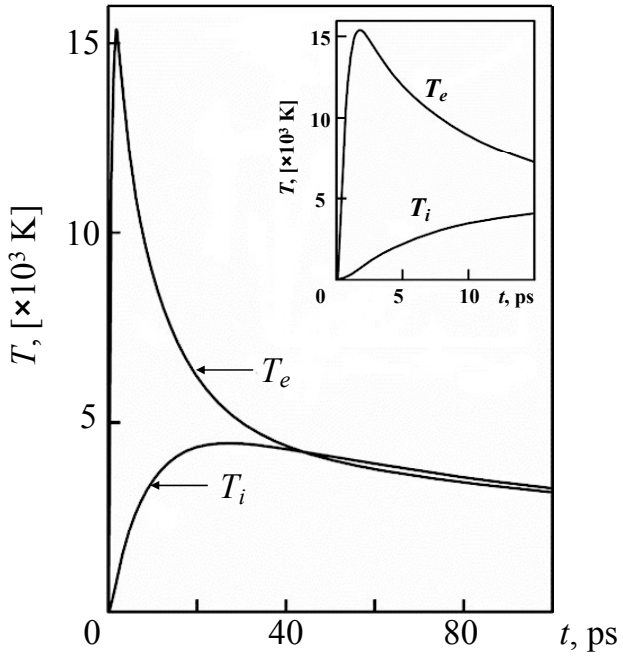

Fig. 1.9: Dynamics of metal heating by a laser pulse of τ_{pulse} =1 ps duration and a pulse energy density 0.15 J/Fig. 1.9cm². T_e and T_i refer to electron and ion lattice temperature, correspondingly. The inset shows an enlarged view of the initial stage of the process (after [AnL02]).

1.3. Transient effects of multipulse laser irradiation

Obviously, the absorption of laser energy causes modifications in the irradiated target. On the one hand, a pulse-to-pulse increase of the excited-electron density may influence optical properties of the irradiated material and, thereby, its absorption properties. On the other hand, photoemission and subsequent desorption of individual ions disturb a local surface order. As indicated in Fig. 1.2, desorption leads to creation of localized defect states within the bandgap that reduces the order of the nonlinear absorption, thus increasing the absorption probability. These changes of the excited material may last for a considerable time [Ito82], affect surface optical breakdown and reduce the damage fluence threshold for multipulse irradiation [ASR00], [Cos07].

1.3.1. Laser induced defects

Primary interaction between ionizing irradiation and solids not only produces electrons and holes, but also creates excitons, i.e. an excited electronic state of the crystal lattice. Excitons have a longer lifetime than free charge carriers and can relax through emission of luminescence, or interaction with impurities or defects in crystals [Ito82], [ItN86]. In materials with strong electron-phonon coupling (e.g. wide bandgap dielectrics), the excitons are in a self-trapped configuration, caused by the strong electron-lattice interaction. The self-trapped excitons (STE) transfer the excitation energy through the local lattice deformations from ion to ion without moving of the ions themselves [AsM76]. Excitation of the STE with the subsequent pulses generates F color centers [TKI89] (electron is trapped in anion vacancy) that lead to the formation of permanent defects and emission of particles.

A perfect ionic crystal with a large band gap (typically 8-12 eV) is widely transparent for near-IR laser light with photon energy of about 1.55 eV. The laser-matter interaction can be realized through electronic band-band transitions by simultaneous absorption of many photons. This process has a rather small cross-section. The presence of any defects (imperfections, impurities or laser-generated defects) in the crystal creates localized electronic states inside the band gap that facilitates absorption and can lead to a resonant enhancement of the process by several orders of magnitude [Rei89].

A typical example is the formation of laser induced defects in alkali halides. An optical absorption spectrum of NaCl, measured directly after femtosecond multipulse laser irradiation, has revealed several absorption peaks that were attributed to the formation of F color centers, an electron trapped in an anion vacancy, and their aggregates F_2, F_3, F_4. [HCR02]. The reported lifetime of bulk F-centers is several minutes, while surface color centers should recombine much faster. Observable changes in color of the irradiated surface after several minutes lets us assume that the F-centers can be transformed to stable metallic colloids.

Defect formation similar to those in alkali halides are observed in alkaline-earth fluorides under irradiation with an energetic electron pulse. [ScS60], [WMW77]. Study of the dynamics of high excited self-trapped excitons (STE) in a CaF_2 crystal has been reported by Tanimura *et al.* [TKI89]. They have demonstrated that both electrons and holes excitation of the STE results in generation of F-centers.

1.3.2. Incubation

For multipulse (N-on-1) irradiation, the incubation behavior of materials has been observed experimentally [HVW99], [ALS99] [ASR00], [HMW00]; i.e., ablation takes

place upon irradiation with pulse's energy below the single-shot ablation threshold. An interpretation of the incubation is based on a pulse-to-pulse defect generation until the defect density locally saturates. According to empirical observations [HVW99], [Cos07] ions desorption takes place when a certain surface defect density is locally reached.

The incubation of dielectric crystals upon multipulse laser irradiation (800 nm, ≈100 fs) was studied intensively in our laboratory by different researchers [HVW99], [HWR00], [CER08]. As shown in Fig. 1.10 (a), it is necessary to apply a certain number of incubative pulses N_{inc} to reach a "steady-state" ablation regime. On the other hand, the number of the incubative pulses N_{inc} decreases with the increasing intensity (Fig. 1.10 (b)).

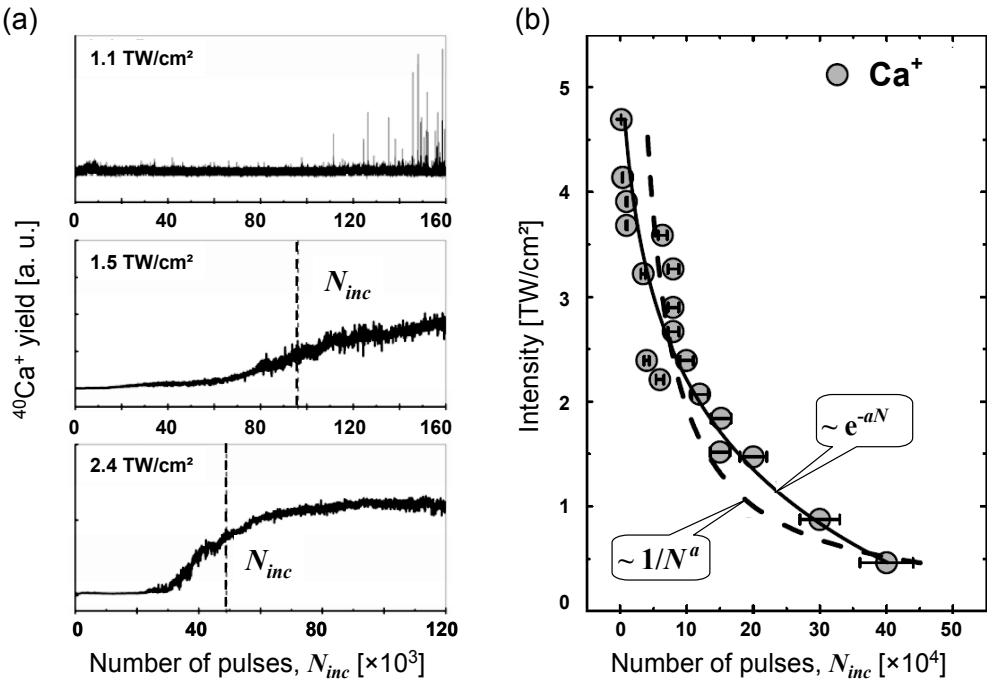

Fig. 1.10: (a) Incubation behavior of Ca^+ ions from CaF_2. A number of incubative pulses N_{inc} is set at a mean value between an average minimum and maximum ion yield, respectively [Cos07]. (b) Dependence of the multipulse (N-on-1) desorption threshold intensity on the number of incident pulses. The experimental data are fitted with an exponential decay (solid line) and a power low (dashed line) (after [CER08]).

A model taking into account defect generation upon repetitive pulses reveals the best fit to the experiments [CER08], as indicated by the solid line in Fig. 1.10 (b). Reduction of the damage threshold intensity I_{th} is explained by an exponential pulse-to-pulse growth of the number of laser-induced defects [PER89]. In this framework,

the following relation between the threshold intensity I_{th} and the number of laser pulses N was proposed:

$$I_{th}(N) \sim \exp(-aN), \tag{1.19}$$

where a is a constant.

In another approximation, the dashed line in Fig. 1.10 (b), the incubation data were fitted by a power function proposed in a statistical model [JBW88] for ablation of metals. In this approach, the ablation threshold I_{th} is inversely proportional to a power α of the number of incident pulses N:

$$I_{th}(N) \sim 1/N^{a}. \tag{1.20}$$

1.3.3. Conclusion

The effect of cumulative exposure to many laser pulses results in a generation of transient defect states within the bandgap. If the decay of the defects lasts longer than pulse separation time, they enhance the probability of light absorption and subsequent particle emission from the irradiated surface, supporting a certain feedback between successive pulses. In our conditions of a laser pulse repetition rate of 1 kHz, long-lived surface defects (with lifetime longer than 1 ms) could survive between pulses. Their interaction and accumulation upon repetitive irradiation leads to the creation of large conglomerates that can be considered as a possible mechanism to transfer information about the incident laser electric field from one pulse to the other.

1.4. Models of ultrashort pulsed laser ablation

Laser ablation from solids includes a whole range of optical, mechanical and thermodynamic processes, which become more intricate for shorter laser pulses. The complexity and many-sided nature of laser-material interaction, depending on the electronic structure of the target and laser characteristics, makes it very difficult to represent all different aspects of ablation in a common/universal model.

Experimental and theoretical research has shown that despite their distinct electronic structure, different materials behave very similarly upon irradiation with subpicosecond pulses [CSB99], [Cos07]. In the preceding chapter (Ch. 1.2) it was shown that after optical excitation by a femtosecond laser pulse the excited electronic system of solids is in transient nonequilibrium with the lattice. The follow-up

processes, modification of the irradiated material and the resultant target defragmentation/ablation, are discussed further in frameworks of different approaches.

1.4.1. Coulomb explosion in Dielectrics

A mechanism known as Coulomb explosion has been proposed to explain material removal for dielectric targets upon ultrashort laser pulses [HWR00], [SRA02], [GRT02]. So far, it has been shown that the laser pulse induces multiphoton ionization at the irradiated surface. During the pulse, appreciable numbers of photoelectrons almost instantaneously escape from the irradiated area, inducing an excess positive charge that is localized in the thin surface layer and cannot be compensated for due to the low carrier mobility. When a sufficient local charge density is achieved, the target surface becomes electrostatically unstable resulting in a Coulomb explosion [HWR00], [RHW00], [SRA02] of positive ions. This explosion scenario, illustrated in Fig. 1.11, is strongly supported by the high kinetic energies of the expelled positive ions, which are about of 100 eV and depend only on the charge state and not on the mass of the sputtering fragments [HWR00].

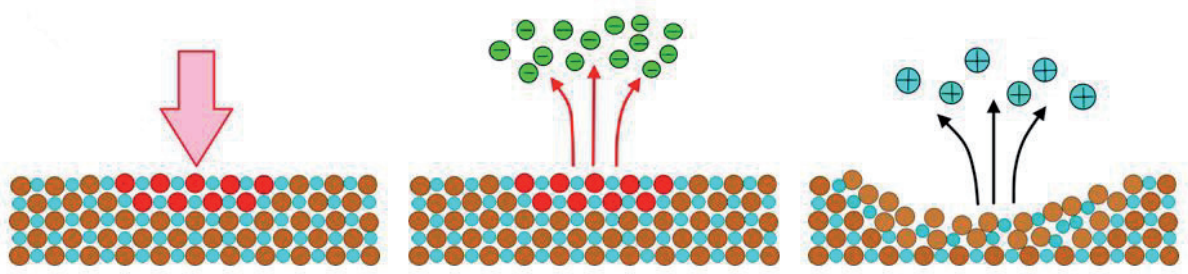

Fig. 1.11: Coulomb explosion is a possible mechanism for the dynamics of femtosecond laser ablation: intense laser pulses (≈100 fs) induce multiphoton ionization (left panel); emission of photoelectrons and creation of positively charged/electrostatic unstable area (the central panel); ejection of positive particles (right panel).

Only at much higher irradiation dose, negative ions (and, probably, also neutral atoms) occur in ion mass ToF spectra (*Phase explosion*; cf. 1.4.2.1). As reported by M. Henyk [HWR00] and F. Costache [Cos07], the negative ion emission exhibits some specific characteristics in dynamics in comparison to that of positive ions. First, even at high intensities it needs a few thousand laser pulses before an appreciable signal of the negative ions yield appears. Other peculiar features of this process are a relative longer time-of-flight and a broader angular distribution; that means the emission is considerably delayed with respect to the laser pulse and the kinetic energy of the ions

is very low. All this supports the thermal mechanism of desorption of the negative ions.

1.4.2. Ablation mechanisms of Semiconductors and Metals

Pulsed laser ablation of semiconductors and metals could be described by thermodynamic processes such as vaporization (t > 1 ns), normal boiling (t > 100 ns) and explosive boiling (t≈1÷100 ns) (*phase explosion*) [MiK95]. The relevance of these processes depends on the laser pulse duration and on the temperature of the irradiated target. Moreover, all these effects are considered to occur mainly for ablation with long pulses [MiK99].

Ablation with subpicosecond pulses is often described as a direct solid-vapor/plasma transition [CMN96], where all thermal effects can be neglected in a first approximation. However, as shown in numerous studies [LSB97], [SBL95], [CSB99], [BuB02], the situation is more complex: at the threshold fluencies, ablation may occur either thermally or nonthermally. As it has been reported by some groups [CSB99], [BuB02], the typical *phase explosion* is observed for a whole range of materials irradiated with pulses of duration as short as 100 fs. Hence, the question about the ablation mechanisms under femtosecond laser irradiation is still open. The possible paths are discussed below.

1.4.2.1. Phase explosion

In the case of an intense irradiation with sufficiently short pulses, when the temperature of the target surface almost reaches the thermodynamic critical temperature T_c, homogeneous bubble nucleation near to the surface can occur, and this unstable, superheated, high pressure region can relax through a fast explosive transition (*phase explosion*) from superheated liquid to a mixture of gas phase and liquid droplets [MiK95]. This mechanism is supposed to be responsible for ablation of semiconductors and metals [LSB97], [CSB99], [SRA02].

Possible thermodynamic pathways of ablation can be illustrated by the schematic Van der Waals-like P-V diagram. The main regions are shown in Fig. 1.12. The left- and right-hand sides of the diagram are the liquid and the gas state of the material, correspondingly. The dark shaded area under the spinodal (dbe) represents the inhomogeneous liquid-gas mixture. This two-phase instability region borders with the light shaded area delimited with the binodal (abc). The light shaded area indicates metastable homogeneous phases and corresponds to superheated liquid (adb) and undercooled gas (ebc). The binodal curve is the coexistence curve of liquid and gas

phases. The temperature maxima of the binodal and spinodal coincide and are known as the thermodynamic critical temperature T_c.

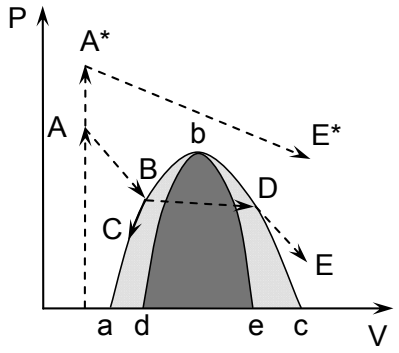

Fig. 1.12: Schematic Van der Waals-like P-V diagram of a solid and thermodynamic path of ablation (after [CSB99]).

Highly intense laser pulses can heat the material in a very short time (in a few picoseconds [SBL95]) above the critical point. This state is presented by the point A* in the diagram (Fig. 1.12). From this superheated state, the system can relax through a fast adiabatic expansion directly into the gas phase (A*→E*), avoiding the two-phase regime.

For laser fluencies at about the ablation threshold [CSB99], the situation is more complex. The liquid heated to the temperature above the T_c, the point A in Fig. 1.12, can undergo adiabatic cooling and reach the liquid-gas equilibrium curve (abc). On the pathway A→B, the pressure is reduced through mechanical expansion within several picoseconds. Crossing of the binodal at the point B corresponds to the transition of the system in the metastable region, where the superheated liquid tends to the formation of gas bubbles. Here, the material can either cool down as a liquid along the binodal (B→C) or cross over the two-phase instability region (B→D) as an inhomogeneous gas-liquid mixture. On this pathway, a rapid nucleation of gas bubbles inverts the liquid phase in a gas containing liquid droplets and progressive evaporation takes place. This homogeneous boiling, known as *phase explosion*, takes place over the whole liquid layer and not only at the surface like normal heterogeneous boiling [MiK95]. After several nanoseconds [LSB97], [SoL00], the material transforms into a gas (D→E).

1.4.2.2. Ultrafast nonthermal melting

For pulses with subpicosecond duration, laser induced melting has been reported to be an ultrafast, nonthermal process. Experimental and theoretical studies of the electronic excitation showed that the crystal lattice exposed to an ultrashort intense laser

irradiation can be driven directly into a disordered state, long before the electron-phonon coupling takes place [StB94], [SAP96], [LSB97], [CSB99], [SCS99], [LiS00], [RRF01], [LEG08].

Studies on temporal dynamics of femtosecond ablation from semiconductors, using second harmonic generation (SHG) from the surface, showed a drastic decrease of the reflected SHG-signal during the pulse ($\tau_{pulse} \approx 100$ fs) and, simultaneously, increasing of the optical reflectivity [LSB97][1]. Such fast changes of these parameters were observed at fluencies that exceed the melting threshold by about five times and indicated an ultrafast solid-liquid phase transition that cannot be explained by classical thermal melting. Direct observations of a nonthermal melting at the surface of semiconductors, Ge and GaAs, irradiated with femtosecond pulses at intensities close to the single-shot ablation threshold, was reported by Siders *et al.* [SCS99]. Measurements of the time-resolved x-ray reflectivity from a thin Ge (111) film suggest that the irradiated target rapidly and homogeneously melts through a nonthermal fragmentation in the first few picoseconds after the laser pulse. Moreover, it was demonstrated that beneath the ultrafast solid-liquid phase transition, also thermal melting takes place. Recently, Lindenberg and coauthors [LEG08] have revealed experimental evidence of atomic displacement upon subpicosecond laser irradiation, leading to the ultrafast disordering of the crystal lattice. During the first few hundred femtoseconds, the atoms start to fluctuate around their initial position in a crystal with increasing amplitude, but the average displacement from the equilibrium state is still zero. These experimental studies are supported by molecular dynamics simulations [StB90], [StB94], [SAP96], [ZhG00], [JDG09], which provide the same time scale of the disordering of the crystal structure due to electronic excitation, and melting of the target in less than one picosecond.

In conclusion, under femtosecond pulsed laser excitation, a non-thermal solid-liquid transition occurs on a subpicosecond time scale within an extreme thermal nonequilibrium.

1.4.2.3. Role of thermal melting

As has been mentioned, during the irradiation of the semiconducting target with femtosecond laser pulses at near threshold intensities, a thermal melting mechanism is also activated beneath the nonthermal processes.

The excited electrons translate their energy to the lattice through electron-phonon interaction within a time equal to the electron-phonon coupling constant, which is

[1] Anyway, these results should be interpreted carefully. In semiconductors, changes of these optical properties can be caused by the conduction band electrons alone.

about a picosecond in silicon [LiS00]. When a sufficient amount of energy is invested in the system, nucleation and growth of the liquid phase occurs heterogeneously at the surface layer and moves into the solid. At this stage thermal melting (loss of long range order) takes place on a relatively long time scale and the deposited energy distribution is close to the thermal equilibrium and can be characterized by the temperature profile [LSB97].

Complex dynamics of the excited electrons induces structural modifications of the crystal lattice that proceed through both non-thermal and thermal mechanisms, and, finally, lead to macroscopic removal of a material.

1.4.2.4. Possibility of Coulomb explosion

It is generally assumed that in semiconductors and metals, irradiated with femtosecond pulses, Coulomb explosion cannot occur because carrier transport is fast enough to neutralize the holes produced by laser ionization [BOM04].

The first convincing experimental evidence of an electrostatic explosion in silicon was observed in the regime of high fluence (more than 1 J/cm^2) by Roeterdink *et al.* [RJV03], although this effect was predicted in a molecular dynamics simulation at much lower fluencies for 80 fs pulses [HGC97]. Further experimental observations on ultrashort laser ablation of semiconductors and metals confirmed the possibility of Coulomb explosion at fluencies at about the ablation threshold for pulses shorter than 100 fs [DHB06]. Finally, a recent study of laser-induced (λ_{laser} = 800 nm, τ_{pulse} = 130 fs) particle emission from a copper surface has proposed the Coulomb explosion as a possible origin of a ripple formation [HNO10]. These experimental data are interpreted in the framework of the model in which the laser field induces a charge distribution on the irradiated surface due to interaction with electrons in the metal and creates an ion-enriched local area that explodes due to Coulomb repulsion [SHT09]. By repetitive irradiation the first surface modification/defect states will be preferentially ablated because of high absorption probability, thus the ripples will be formed.

On the other side, experimental studies of the ion dynamics by femtosecond laser ablation of silicon [CKR04], [MBP04], [BOM04] have provided results similar to dielectrics, suggesting electrostatic explosion. Positive ion yield consisting not only of single and double charged atomic ions, but also of larger clusters and velocity distributions of ablated particles depend strongly on applied laser irradiation dose. Analysis of kinetic energy of the ablated products indicates that the surface is far from thermal equilibrium and that the species observed in ToF mass spectra can be produced by nonthermal explosive mechanisms.

1.5. Conclusion

Ultrashort laser ablation of various materials (dielectrics, semiconductors and metals) is characterized by several common features, which can be related to similar background physics. The rapid excitation of electrons by the incident laser electric field induces a strong instability of the crystal lattice due to a softening of the atomic bonds. Additionally, the surface equilibrium order can be disturbed due to emission of individual components. As a result, the target is perturbed on a very short time scale though it is not molten; i.e. the system is strongly unstable and very far from thermodynamic equilibrium. This nonequilibrium in the system aspires to be balanced through redistribution of the deposited energy on a time scale about of several hundred femtoseconds leading to a destabilization of the crystal lattice [LEG08], and, finally, to a macroscopic material removal. The short relaxation time is conditioned by a steep gradient in crystalline order to the surrounding material and excludes any classical thermal routes [Rei09].

2. LIPSS: survey of experimental data and models

2.1. Experimental observation of LIPSS

The first experimental registration of laser-induced periodic surface structures (LIPSS), also known as ripples, was reported in 1965 by Birnbaum [Bir65]. A regular system of parallel straight lines was produced on the surface of various semiconductors irradiated by a focused ruby laser beam. Later, the laser-induced patterns have been observed at the surfaces of intrinsic and extrinsic semiconductors [YSP82, [YPD83], dielectrics [TeS81], [VWR98], [HVW99], [OMR99], [RCH02], metals [KeB82], [YPD83], [EZS84], [GCP11], compound materials [BSS00], [BMS05] and polymers [KTL95], using irradiation of cw to subpicosecond pulse duration with wavelength varying from ultraviolet [ClE89] up to far infrared [EHW73]. Ripples were reported not only on bulk materials, but also on thin films [YaT99], [YMK03]. The common characteristic features of the observed damage patterns indicate that LIPSS, forming upon irradiation near or slightly above the ablation threshold with a few laser pulses, can be generated on any material, regardless of its dielectric constant.

2.1.1. Femtosecond laser-induced surface structures

The development of laser technologies and application of ultrashort, i.e. subpicosecond pulses in material processing, has revealed a large diversity of surface structures distinct from the earlier observed LIPSS [Bir65], [EHW73], [YSP82], [YPD83]. Along with the classical ripples of periods around the laser wavelength, also fine nanoripples with a feature size much smaller than the applied laser wavelength and coarse macroripples with a lateral size in a range of several microns, as well as even more complex patterns like arrays of conical features were registrated at the laser-modified area [VWR98], [OMR99], [BBK02], [BBM04], [BRK09], [DRD09], [CHR02], [CHR03], [CKR04], [SKS05], [MiM07], [MiM06], [LLZ12]. Very often, several different types of these structures can coexist in the same ablation spot.

In 1998, Varel et al. [VWR98] presented images of ablation craters on sapphire produced by 15 ultrashort (200 fs) laser pulses at a wavelength of 790 nm, where the nanoripples could be seen on the edge of ablation spots. In 1999, ripples with multiple periodicities down to 50 nm were reported on diamond crystals by femtosecond ablation with pulses of 380 fs duration and at a wavelength of 248 nm by Ozkan *et al.* [OMR99].

Since the end of the 1990s it has been established that, typically, these structures can be generated upon irradiation of the picosecond to femtosecond range at intensities

below or near the single-shot ablation threshold on surfaces of different solids (crystalline and amorphous insulators, semiconductors, and metals). The laser-induced morphology is qualitatively independent of the kind of ablated material and of its crystallographic structure. Generally, the LIPSS completely develop only after a considerable number of pulses [BSS00], [BBK02], [CHR02], and positive feedback plays an important role in the ripple formation process [TKM07], [Rei09]. The period and complexity of the ripples vary across the ablation spot, from fine and regular at the edge to coarse and complex in the middle, depending rather on the local pulse intensity than on the laser wavelength [CHR02].

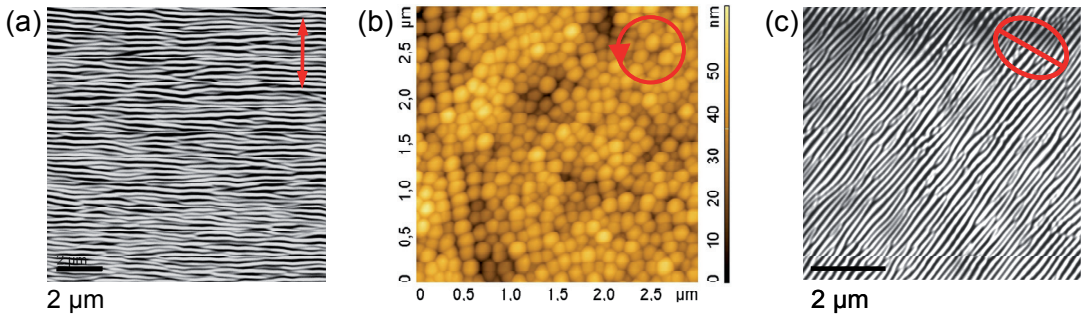

Fig. 2.1: Micrographs of sections from the bottom of ablation craters obtained on a CaF_2 surface. (a), (b) and (c) show patterns generated with linearly, circularly and elliptically polarized irradiation (λ_{laser}=800 nm, $\tau_{pulse}\approx$100 fs), respectively (5,000 pulses@8.1 TW/cm^2). (State of the laser polarization indicated at the right upper corner).

Pattern morphology and orientation are typically controlled by the polarization state of the laser electric field [RCH02], [RCV09], [HRK12]. Linear high-periodic structures with multiple bifurcations or an arrangement of nanospheres are typical for linearly and circularly polarized light, respectively, as shown in Fig. 2.1 (a) and (b); a mixture of long and short lines (Fig. 2.1 (c)) is observed for elliptically polarized pulses. However, extended macroscopic surface defects also play an important role as an order parameter [RVC08], the influence of the surface defects on structure orientation being even significantly stronger than that of the polarization (Fig. 5.13).

At an increasing irradiation dose, also the superposition of several structures can be observed. Detailed inspection of the ablation spot on CaF_2, induced upon 10,000 pulses of linear polarization at intensity 8.4 TW/cm^2, reveals complex structuring of the crater walls. A coarse overstructure that is not really related to the polarization direction (Fig. 2.2 (a)), and fine ripples with spacing less than 20 nm, directed perpendicular to the laser electric field (Fig. 2.2 (b)), coexist in the irradiated area.

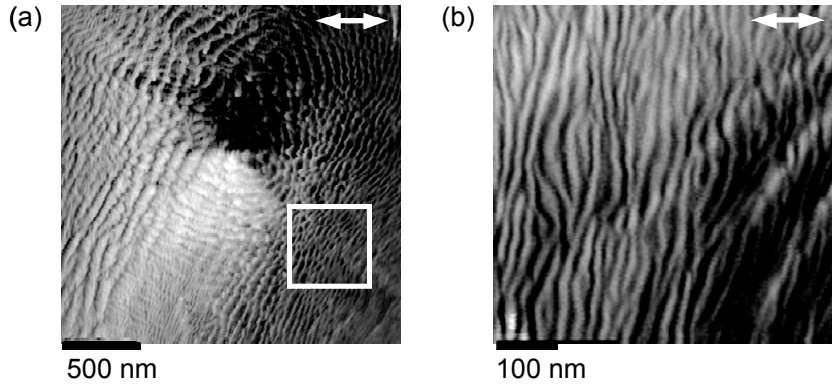

Fig. 2.2: SEM micrographs in the central part of an ablation crater on CaF_2 (10,000 pulses@8.4 TW/cm^2) exhibiting: (a) radially spreading coarse overstructure and (b) magnified area of the region marked (a) presenting fine ripples. The double arrows indicate the direction of the laser polarization.

2.2. Modeling of ripples formation

Experimental observation of ripples over such wide range of materials and over a large wavelength interval has been accompanied by intensive theoretical studies; however, the underlying physical mechanisms are not still fully understood. Presently, two basically different approaches are discussed in the literature.

The "classical" approach assumes that a lithography-like *modulated energy deposition*, caused by some optical interference, is imprinted into a corresponding ablation pattern and thus results in a modulated surface morphology, as shown in Fig. 2.3 (a) [DSY82], [SYP83], [YSD84]. In that model, ablation occurs in the areas where the absorbed energy is largest, and the ripple formation process is lithography-like, where the irradiated material only plays a *passive* role. Another approach, schematically presented in Fig. 2.3 (b), known as a *self-organization model* [HVW99], [RCH02], is based on the dynamics of ultrashort pulse laser interaction with the target material [Rei89], [RHW00], and is inspired by the similarity of the laser generated patterns with those observed in very many other fields in nature, in particular in surface sputtering by energetic ions [CuB95]. The model supposes an *active* contribution of the irradiated material: The absorbed laser energy causes perturbation and softening of the crystal binding, leading to an unstable surface region, which relaxes via self-organization. As a consequence of this, a spontaneous formation of surface structures occurs in the laser-modified area [RCB06], [RVV11].

Advantages and weaknesses of both theoretical models in the light of the recent experimental data will be discussed in this chapter.

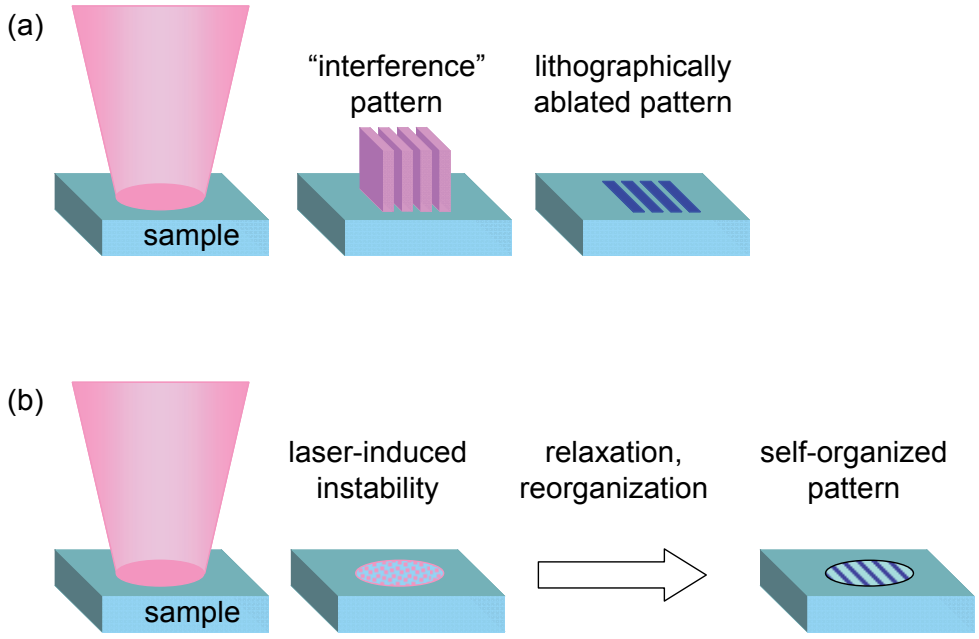

Fig. 2.3: Different approaches of LIPSS formation: a) spatially modulated energy deposition ("interference" pattern) results in modulated ablation; b) "self-organization model": femtosecond irradiation induces a high degree of instability at the surface; the perturbated surface relaxes through reorganization which leads to the formation of self-organized patterns in the laser-affected region.

2.2.1. Inhomogeneous energy deposition as origin of LIPSS

The first quantitative description of LIPSS was proposed in 1973 by Emmony *et al.* [EHW73]. A linear periodic damage pattern with the periodicity corresponding to the laser wavelength was explained by a modulated energy deposition due to interference between the incident laser field with some form of a surface-scattered electromagnetic wave. It leads to a modulated ablation and formation of periodic structures with a spatial period Λ given by:

$$\Lambda = \frac{\lambda_{laser}}{1 \pm \sin\theta}. \qquad (2.1)$$

Here λ_{laser} is the laser wavelength, θ determines the angle of incidence of the beam on the surface, and the positive and negative signs correspond to the backward and forward scattered surface waves, correspondingly. The pattern is oriented perpendicular to the vector E of the incident laser field.

Further development of Emmony's approach consisted in definition of the nature of the "surface-scattered wave" for different experimental conditions. For instance, Temple and Soileau [TeS81] introduced the scattered field generated by the interaction of the incident laser field with the material defects.

Several authors studying ablation of metals suggested that surface plasmon polaritons (SPPs), collective longitudinal oscillations of electrons, could be responsible for the ripple formation [KeB82], [EZS84]. SPP waves are electromagnetic waves of the transverse magnetic type that are localized in the surface region and can propagate along a metal-dielectric interface. The SPP-field can be excited at the metal-dielectric boundary if the dielectric constant of one of them (dielectrics) is real and positive ($\varepsilon_1 > 0$), and the other medium (metal) is characterized by a frequency-dependent, complex dielectric function $\varepsilon_2(\omega)$, with negative real part $\Re e(\varepsilon_2) < 0$. Moreover, the dielectric functions are related as $\varepsilon_1 < |\Re e(\varepsilon_2)|$. Interaction of the SPPs with the incident wave results in the spatial modulation of the deposited energy and modulated ablation.

Some surface structures whose origin cannot be linked to interference were attributed to a standing acoustic wave pattern due to a nonlinear interaction between several laser modes taking place in the irradiated sample [MHL78] or to laser induced capillary waves [ClE89]. Among a number of models, the most rigorous and currently accepted form of the "interference" model was formulated in the beginning of 80s by Sipe *et al*. [SYP83].

2.2.1.1. Sipe's model

Sipe *et al.* [YSP82], [SYP83] studied interaction of a laser beam, modeled as an infinite plane wave, with a rough surface in $\vec{k}$ space. The model predicts LIPSS formation due to a modulated energy deposition caused by interference of "scattered waves" with the refracted laser beam. Here, the coherently "scattered field" is generated by a microscopic surface roughness *l*, which is smaller than the laser wavelength λ_{laser} and localized in the "selvedge region" [Sip80], [SiB81]. Here, *selvedge* is part of both adjacent media, as shown in Fig. 2.4.

The optical properties of the "selvedge" are different from the bulk material, and a bulk dielectric function cannot be used to describe this special region. While the dielectric function of the bulk material is constant and has the value ε and the dielectric constant of the vacuum ε_{vac}=1, the selvedge dielectric function depends on the surface roughness, or surface filling factor *f* [SYP83], that can vary from zero to one, $0 \le f \le 1$, corresponding to the "unfilled" and "filled" part of the selvedge, respectively. Based on this assumption, the selvedge dielectric function ε' can be approximated as:

$$\varepsilon' = \frac{1+f}{2}\varepsilon \quad . \tag{2.2}$$

The geometry of the model is shown in Fig. 2.4: the linear polarized laser beam of wavelength λ_{laser}, with a wave vector $\vec{k}$, strikes the rough surface ("*selvedge"*) at an incident angle θ. The component of the wave vector $\vec{k}$ parallel to the surface is referred as $\vec{k}_i$. In the absence of surface roughness, only the usual refracted beam with the component $\vec{k}_i$ parallel to the surface would be generated in the bulk. But, due to a Fourier component of surface roughness at $\vec{k}$, "scattered" fields appear in the bulk at $\vec{k}_{\pm} = \vec{k}_i \pm \vec{k}$. The interference of the "scattered" and the refracted components of the incident laser field causes the non-uniform energy absorption with a magnitude $I(\vec{k})$:

$$I(\vec{k}) \propto \eta(\vec{k};\vec{k}_i) \cdot \left| b(\vec{k}) \right|. \tag{2.3}$$

Here $b(\vec{k})$ is a magnitude of the surface roughness; and function $\eta(\vec{k},\vec{k}_i)$ describes the efficacy with which the roughness leads to inhomogeneous energy absorption at $\vec{k}$ just below the selvedge. An expression and detailed analysis of $\eta(\vec{k},\vec{k}_i)$ can be found by Sipe *et al.* [SYP83]: it has been shown that the efficacy factor η can exhibit very sharp peaks that occur at $\vec{k}$ satisfied to:

$$\left| \vec{k}_i \pm \vec{k} \right| = \frac{2\pi}{\lambda} \tag{2.4}$$

or

$$\left| \vec{k}_i \pm \vec{k} \right| = n\frac{2\pi}{\lambda}, \tag{2.5}$$

where n is the refractive index of the material. From the physical point of view, these conditions (2.3) and (2.4) can be explained by excitations of SPPs or as the result of nonradiative fields ("radiation remnants") in polaritons-inactive materials [YSP82], [DSY82]. The peaks determine the strongest energy deposition in $\vec{k}$ space and, correspondingly, the spatial ripple periods of LIPSS.

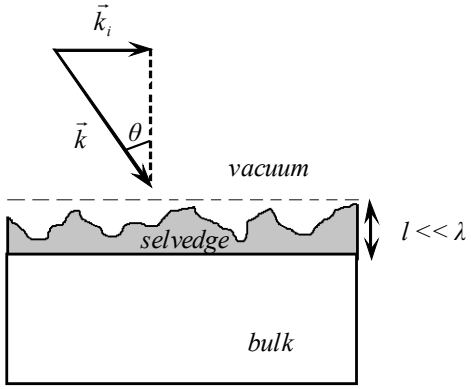

Fig. 2.4: Geometry for inhomogeneous energy absorption in the model of Sipe [SYP83].

In the model, occurrence of periodic patterns with the spatial periods $\Lambda_{1,2}$ given by Eq. (2.1) and with $\Lambda_3 = \frac{\lambda}{\cos\theta}$ is predicted. The third ripple set (Λ_3) would be generated with p-polarized light and be oriented parallel to the laser electric field. It has been shown that under special experimental conditions, pattern arrays with all three spatial periods can coexist intermixed in the same area.

2.2.2. "Extension" of the classical approach

To describe the femtosecond laser-induced pattern with periods much smaller than the laser wavelength, optical properties of the excited target material were taken into account [WMF03], [BBM04] and the "surface scattered field" in the classical approach was modified to the short-wavelength irradiation generated by higher harmonics [BMS05], [CrH07], [DRD09] or excitation of surface plasmon polaritons [MiM08], [BRK09], [GCP11].

2.2.2.1. Dielectric function of laser-excited material in Sipe's model

The classic model of ripple formation based on the inhomogeneous energy deposition [SYP83] considered light-matter interaction in the framework of linear optics; neither microscopic transient properties of the irradiated target, nor nonlinear effects were taken into account. In the model, the efficacy factor η depends on the laser irradiation parameters as well as on the optical properties of the target that were described by the complex dielectric function $\tilde{\varepsilon} = (n + ik)^2$ [BMS05].

Bonse and co-authors [BRK09] modelled the optical properties of laser-excited silicon according to the Drude model, where the complex dielectric function of the irradiated material consists of two parts:

$$\tilde{\varepsilon}^* = \tilde{\varepsilon} + \tilde{\varepsilon}_{Drude}, \tag{2.6}$$

where the first term in the equation, $\tilde{\varepsilon}$, is the complex dielectric constant of the nonexcited material; the second term, $\tilde{\varepsilon}_{Drude}$, corresponds to the generation of free electrons in the conduction band during laser irradiation.

The part of the dielectric function describing free-electron effects in the conduction band, $\tilde{\varepsilon}_{Drude}$, can be given by the Drude model [SoL00]:

$$\tilde{\varepsilon}_{Drude} = -\left(\frac{\omega_p}{\omega}\right)^2 \frac{1}{1+i\dfrac{1}{\omega\tau_D}}. \qquad (2.7)$$

In this equation $\omega_p = \sqrt{N_e e^2 / \varepsilon_0 m_{opt}^* m_e}$ is the plasma frequency with the electron charge *e,* carrier density N_e and the vacuum dielectric permittivity ε_0; m_{opt}^* and m_e stand for the optical effective and the free electron mass, correspondingly; and τ_D is the Drude damping time accounting for *e-e* and *e-h* scattering.

2.2.2.2. Surface plasmon polaritons in the ripple formation model

While in semiconductors and metals the intense femtosecond irradiation is able to excite surface plasmon-polaritons already during the first pulse, in dielectrics this process seems to be possible as a consequence of repetitive irradiation.

By using ≈100 fs laser pulses, absorption of the laser energy in the bulk of material results in generation of conduction band electrons during the pulse by multiphoton ionization. Crystallographic imperfections or impurities and long-lived defects created by the repetitive laser irradiation [CER08] cause an increase of the ionization probability by several orders of magnitude [Rei89] and locally enhance the free electron density. We can suppose that such long-lived defects accumulate pulse-by-pulse and may form nano-particles of plasma, like metallic colloids in fluorides, living for a several milliseconds [Cos07]. These metallic nano-particles created by a laser field close to a surface of the irradiated sample become coated with a thin dielectric layer because of the high escape probability of excited electrons in the region. Interaction of infrared laser irradiation with such metal-dielectric composites generates the excitation of surface plasmon-polaritons in the nano-particles which leads to huge enhancement of the local electric fields. SPPs and enhancement of the local field intensify inhomogeneous energy distribution into the area.

Motivated by the strong polarization dependence of ripples, some authors attribute the initial stage of femtosecond LIPSS formation to the excitation of surface

plasmons [MiM08], [BRK09], [GCP11]. In this approach, it has been suggested that the effective coupling of the surface field generated by the plasmons with the incident laser electromagnetic field can induce a significant enhancement of the local fields in the surface layer that initiates the modulated ablation process and leads to the formation of linear periodic surface structures. Initial surface roughness is a crucial parameter in the model that makes possible the excitation of SPPs [MiM07], [MiM08].

The spatial period of the observed surface pattern, Λ, can be derived from the classical model of LIPSS formation [SYP83] by taking into account a correlation with the excited surface plasmon mode [GCP11]:

$$\Lambda = \frac{\lambda_{laser}}{\eta \pm \sin\theta}. \qquad (2.8)$$

Here λ_{laser}, θ are the wavelength and the angle of incidence of the laser beam, correspondingly; and $\eta = \Re e[\tilde{\varepsilon}_m \varepsilon_d / (\tilde{\varepsilon}_m + \varepsilon_d)]^{1/2}$ is the real part of the effective index of the surface plasmon mode, where $\tilde{\varepsilon}_m$ designates the complex dielectric function of the metal, and ε_d is the permittivity of the dielectric material.

It has been reported that SPPs can be generated in the early stage of the laser-matter interaction not only on metallic surfaces, but also on the initially dielectric materials, for instance in semiconductors, that convert to a metallic state upon laser radiation [BRK09]. Here it should be noticed that in this approach the excitation of surface polaritons is possible when carrier density is, approximately, in the range $5 \cdot 10^{21} \text{cm}^{-3} \div 10^{22} \text{cm}^{-3}$. Some theoretical studies investigating nonthermal melting of silicon [SAP96] and experimental research based on the measurements of reflectivity of excited silicon as function of laser fluence [SoL00] suppose the existence of such high carrier density in a surface region. From the other side, pump-probe spectra monitoring of the particle desorption for femtosecond laser ablation from silicon indicates considerable emission of photoelectrons [CKR04], [Cos07]. Here a question arises about the real carrier density that can be achieved upon femtosecond laser excitation in the surface.

2.2.3. Drawback of the classical theory

The theoretical approach based on a modulated energy deposition was in good agreement with many experimental data published at that time [YPD83], [YSD84]: the "interference" model described very well structures consisting of long, almost parallel lines, resembling very much a typical interference pattern, with periods close to the

laser wavelength. These LIPSS are often called “LSFL” (“low spatial frequency LIPSS”) [DRD09], to distinguish them from the femtosecond laser-induced ripples, termed as “HSFL” (“high spatial frequency LIPSS”), with periods much smaller than the laser wavelength. Such fine ripples constitute the major deficiency of the “classical” approach, because they cannot be explained by an optical interference effect. To overcome this problem, additional interactions were introduced into the model. At first, optical properties of the excited target material were taken into account by an adaptable (by an adjustable density of surface free electrons) refractive index of the surface selvedge [WMF03], [BBM04]. Further, the “surface scattered field” in the classical approach was modified to include short-wavelength irradiation, e. g. by the generation of higher harmonics [BMS05], [CrH07], [DRD09] or excitation of high-frequency surface plasmon polaritons [MiM08], [BRK09], [GCP11]. As a consequence, the actual version of the model proposes *different* interaction mechanisms for different kinds of ripples.

Though some progress has been made, and the models discussed above could approximately account for the ripple periods of sub-wavelength range, they are not appropriate to explain other complex features, as, e. g., the dependence of the ripple period on the absorbed laser fluence, as well as multiple bifurcations, coarsening, and the doubling of periods, all of which show up in femtosecond laser ablation experiments. Despite all updating, the classical approach remains unable to explain a diversity of complex patterns, such as cones, “bubbles” (Fig. 5.17), or larger formations (macro structures) (Fig. 5.20), observed after femtosecond laser ablation. In particular, patterns induced by circularly polarized irradiation (Fig. 2.1 (b), Fig. 5.3) cannot at all be interpreted in the framework of this model.

2.3. Self-organization as origin of LIPSS

Analyzing the experimental observations, especially the variety of typical structures shapes and sizes, as well as their complex morphology, it turns out that the femtosecond laser-induced surface structures are very similar to other self-organized patterns originating from instabilities such as, e. g., ripples produced by ion beam sputtering (IBS) [EAC99], [CCV05], [ZFH05], [CZM11].

A detailed comparison of surface morphologies generated by IBS and fs laser ablation (see Fig. 2.5) reveals very strong similarity in the shapes (bifurcating long linear structures) and ripples wavelength ($\Lambda \sim 200 \div 300$ nm).

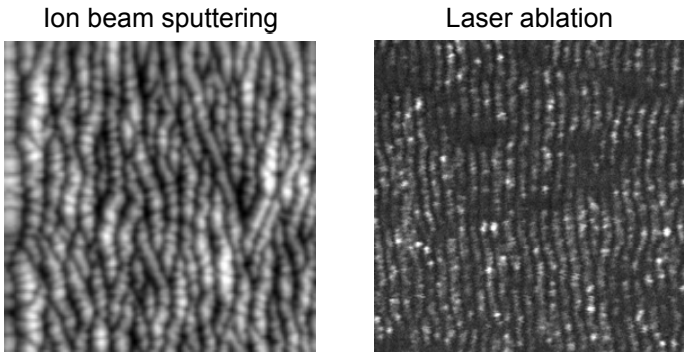

Fig. 2.5: Ripples induced upon Ion beam sputtering and femtosecond Laser ablation. The left image: AFM micrograph of ripple pattern generated on silicon with Ar+ ion beam [EAC99]; the right image: SEM image of ripples structures at the bottom of an ablation crater produced on silicon with 60,000 pulses at 0.4 TW/cm^2 [CKR04]. The size of the images is 2μm×2μm.

In addition to the visual affinity of the patterns, other common features are found such as the dependence of the ripples period on the irradiation dose, namely, on the ions' energy and irradiation time for IBS [CMK94], [ZFH05] and laser intensity and number of pulses in case of laser ablation [CHR02], [KRD05]; or the important role of positive feedback in the development and formation of the pattern [Rei09], [EAC99]; or the coexistence of coarse and fine ripples with abrupt changing of the periodicity ("period doubling") [RCV09]. All this suggests a similar mechanism of ripple formation by energetic ion beam and ultrashort pulsed laser irradiation.

2.3.1. Patterns originating from instability

Pattern formation from instability is very well known as a natural phenomenon, and it is intensively studied in various areas of basic and application science. In nature, ripples can be observed in sandy deserts [MiV03] and on the sea-bottom [HHH01] as a result of interaction between sand grains and wind or shallow wavy water, and even on Mars [MCD98]. In physics, the pattering behavior can be found in different areas of material processing, such as ion-beam sputtering [EAC99], [ZFH05], thin film deposition [TBL98], or as in the present case, as a result of femtosecond pulse laser ablation [HWR00], [BMS05], [SKS05], [MiM06].

After a physical system has been driven into instability, i. e., a state which is not in thermodynamic equilibrium, the system has to move toward a new stable state by some intrinsic nonlinear mechanisms involving positive feedback. The physics of pattern formation can be described within the theoretical framework of nonlinear dynamics. Spatial and temporal evolution of a perturbed system is generally represented by nonlinear partial differential equations, for example equations of the Kuramoto-Sivashinsky/Kardar-Parisi-Zhang type [KuT77], [KPZ86]. The solution of

such equations with corresponding boundary conditions results in pattern formation. Understanding of the physical background in the patterning behavior must include the study of mechanisms how some small effects can govern the dynamics of pattern formation. That is the great scientific challenge.

Attributing the "femtosecond" ripples to the universal phenomenon of spontaneous pattern formation arising from instabilities, we want first to review the well known description of surface patterning by IBS.

2.3.2. Ultrashort pulsed laser induced surface instability

The physical processes of femtosecond laser ablation indicate the generation of a considerable instability at the irradiated surface. The rapid excitation of electrons by the incident laser electric field induces a softening of the atomic bonds [JGL02] through redistribution of the deposited energy on a time scale about of several hundred femtoseconds, leading to a destabilization of the crystal lattice [LEG08]. Additionally, the surface equilibrium order will be disturbed due to emission of individual components (ions, atoms, clusters). As a result, the target lattice is strongly perturbed on a very short time scale[2]; i.e., the system is strongly unstable and very far from thermodynamic equilibrium. This nonequilibrium in the system must rapidly relax via a macroscopic material removal and surface reorganization. The rapid relaxation is provoked by a steep gradient in crystalline order to the surrounding material and occurs too fast to be attributed to any thermal processes [Rei09]. The target is not melted, no evidence of glass /amorphous phases is observed, but reorganization of crystalline fragments. In more details, the situation will be discussed in Ch. 6.

Like a pattern induced by surface bombardment with an energetic ion beam, we attribute such structure formation to a surface self-organization from a high degree of instability induced by irradiation with ultrashort laser pulses. But, in contrast to ion sputtering, when the erosion of the surface takes place *during* ion bombardment and proceeds continuously, femtosecond laser ablation is pulsed process. Energy input and desorption/rearrangement of massive particles are temporally well separated. Consequently, the impact of intense ultrashort pulse on solid surface results in several different regimes shown in Fig. 2.6.

[2] similar to a melt, but not relaxed to thermodynamic equilibrium

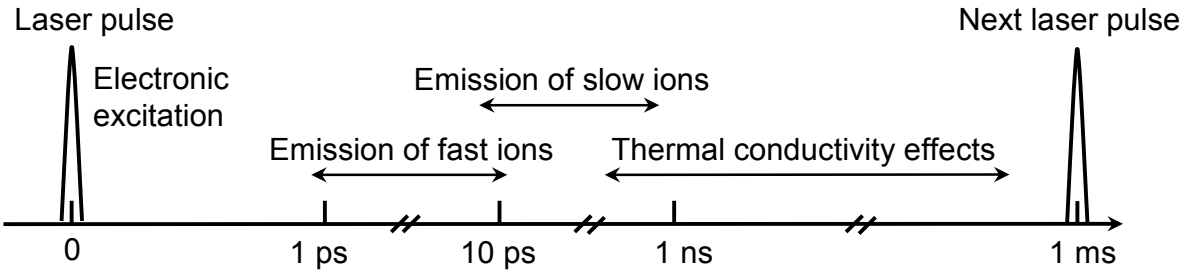

Fig. 2.6: Typical time scales of various secondary processes stimulated by irradiation of transparent dielectrics by a femtosecond laser pulse.

This scheme shows the time scales of secondary processes activated in a transparent dielectric crystal by irradiation with a ≈100 fs laser pulse of 800 nm at intensity well below the single-shot ablation threshold [RCE04]. The incident light first only excites the electrons of the system, their appreciable emission is observed during the pulse. In a second, presumably delayed step, the actual ejection of fast ions (Coulomb/phase explosion) occurs, after a transfer of electronic excitation to the lattice. With the emission of slow/thermal ions, the last step begins, namely, the thermal relaxation on a larger timescale through thermal conductivity effects/thermal self-diffusion of atoms.

2.3.2.1. Evolution of surface profile upon repetitive irradiation

In this subsection we consider the creation of a thin corrugated layer on the surface of the irradiated target upon multiple ultrashort laser pulses. For simplicity, let's restrict ourselves to a dielectric crystal. Initially, the surface of the target is assumed to be ideally plain.

When the laser beam hits a plain surface, a stochastic charge distribution and, hence, an ion emission from randomly located sites can occur in the irradiated area, resulting in the creation of the local defects. A higher absorption probability in the defect states will result in a progressively inhomogeneous surface ionization upon the subsequent laser pulses (cf. sec. 1.3.2). The conception of the corrugated surface layer is shown schematically in Fig. 2.7: small symmetry-breaking irregularities on the initially plain surface develop in the modulated surface layer upon multipulse irradiation. The process is highly nonlinear and boosted by a positive feedback.

After several more laser pulses, a modulated, thin surface film of thickness *a* and modulation height *h(x,y)* builds up (Fig. 2.8). The absorption cross-section of the film is tending towards greater homogeneity with each subsequent pulse. Desorption, however, is not homogeneous and depends on the local surface-curvature.

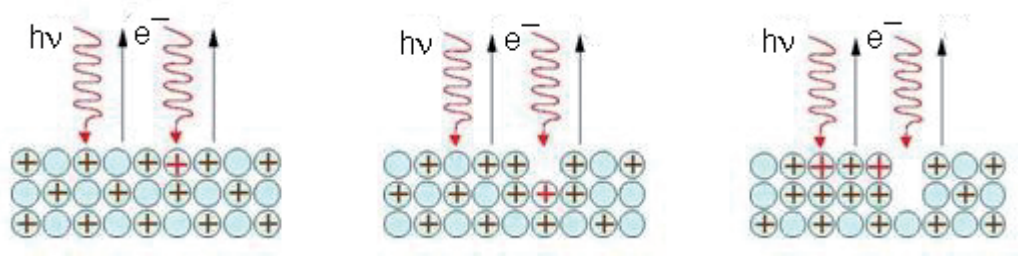

Fig. 2.7: Development of a corrugated surface layer upon multipulse laser irradiation. Incident laser light ($h\nu$) is shown with waved downward arrows; emission of photoelectrons (e^-) is indicated with upward vertical arrows.

Assuming Coulomb explosion, e. g., as the possible ablation mechanism, we can see that for a laser-induced uniform surface charge density, the ion sitting in a valley (Fig. 2.8) has the higher density of (charged) neighbors than an ion on a crest. The higher next-neighbor density results in the stronger repulsion (Coulomb) force and, consequently, in a larger escape velocity of valley-ions, v_{valley}, compared to that from crests, v_{crest}. Similar in silicon and metals: Surface tension in the thin surface film is less in valleys due to higher density of lateral neighbors that results in higher escape probability of valley-ions. So, valleys will be eroded faster than crests; this causes instability of the thin surface film, very similar to the case of ion sputtering (Fig. 3.1).

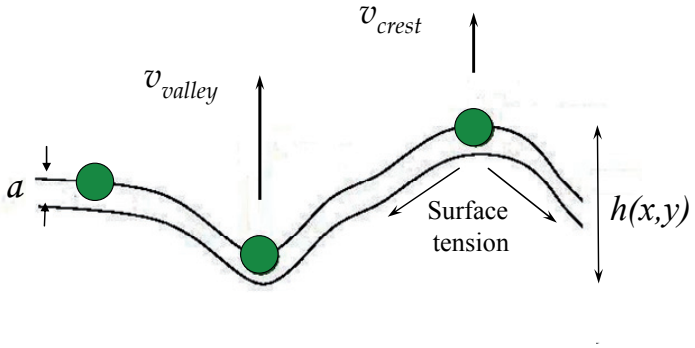

Fig. 2.8: Model for surface height evolution: a is the thickness and $h(x,y)$ is the modulation height of an unstable surface film induced upon repetitive laser irradiation. Velocities of the desorbed ions from the valley (v_{valley}) and from the crest (v_{valley}) are indicated with arrows.

Balancing the surface erosion process, thermally activated self-diffusion tends to smooth the surface again by filling the valleys with diffused crest-atoms. Moreover, in the thin unstable layer the particle on the crest will feel a higher surface tension than in the valley. The tension gradient forces the particles to downhill movement and balances thereby the instability on the surface.

Thus, the time evolution of the growing surface profile can be described by the elementary processes taking place in the system: surface erosion (roughening) due to particle emission and smoothing due to atomic self-diffusion.

2.4. Conclusion

A short review of the development of laser-induced surface structures and the ideas describing the pattern phenomenon have been presented in this chapter. The classical theoretical approach [EHW73], [SYP83] described ripples as the imprint of the optical interference pattern arising on the surface of the irradiated target due to interaction of the incident laser beam with some form of scattered surface waves. The modeling was appropriate for LIPSS induced upon long-pulse irradiation [Bir65], [EHW73], [YSD84], [YPD83].

The application of femtosecond laser irradiation, however, has revealed a large diversity of complex nanopatterns at the modified surface region. It has been established that the peculiar features of "femtosecond pattern" are not compatible with the "classical ripples theory" [SYP83], [YSD84]. Moreover, the ripples exhibit non-trivial surface morphology at nanoscale range, sharing many similarities with other self-organized patterns originating from instabilities. All this provided the preconditions for assuming a non-linear self-organization from laser-induced instability as a responsible mechanism for the pattern formation, similar to the structure formation under ion beam sputtering [BrH88], but the underlying physical mechanisms of energy transfer from laser beam to the target are significantly different.

Meanwhile, the idea of self-organization as driving force of ripple formation is in the good agreement both with theoretical simulations [ZhG00], [JGL02] and with experimental studies of ultrafast spatiotemporal dynamics of femtosecond laser ablation [SBD01], [LEG08], [OON09] and is supported increasingly by a number of scientists [ThC04], [SKS05], [KRD05], [ZGO06], [Lug07], [GRR08].

3. Laser polarization in the model of self-organization

Numerous experimental results have revealed that ripple orientation is strongly dependent on the polarization of the incident laser field. By taking into account that an ultrashort laser pulse is addressing only the electronic system of solids and that the subsequent energy transfer to the lattice occurs on a timescale of electron-phonon relaxation [HSR01] significantly larger than that of the laser pulse duration, an understanding of the puzzling relation between pattern orientation and laser polarization, i.e. the direction of the electromagnetic field vector, becomes very important and interesting.

In the following, this dependence is analyzed within an adopted surface erosion model, based on the description of ion beam sputtering [BrH88]. A continuum theory of erosion by polarized laser irradiation is developed. In particular, the dependence of generated patterns on the laser polarization is considered.

3.1. Pattern formation upon ion-beam sputtering (review)

When a high-energetic ion beam impacts on a target surface, it will penetrate into the solid and transfer its kinetic and potential energy as well as momentum to the lattice atoms through cascades of collisions [Sig69], [Sig73], [Car01]. The volume excited by these ballistic processes is approximately an ellipsoid with the major axis along the incident ion beam direction (Fig. 3.1). During this process, lattice atoms can be displaced from their equilibrium position or, if the transferred energy is sufficient to overcome binding energy, they can be ejected or sputtered from the target.

The volume perturbed by the collisions depends on the energy and mass of the bombardment ions and on the masses of the target atoms. The number of sputtered atoms, or sputtering yield, is a function of the incident ion flux and of the local surface curvature. Erosion of a corrugated surface by an ion beam is shown in Fig. 3.1 (a).

Let us consider the dissipation of energy, deposited at point P, to the target surface. The average energy transferred to O' is greater than at O: $E(O') > E(O)$; that means that the erosion velocity in the valleys is larger than that at the crests, $v(O') > v(O)$ [BrH88]. Thus, the inhomogeneous erosion increases the amplitude of the corrugation and leads to an instability. To complete the surface evolution, thermal atomic self-diffusion activated by the irradiation should be taken into account. The competition between these processes, surface erosion and diffusion of target atoms, results in ripple pattern formation.

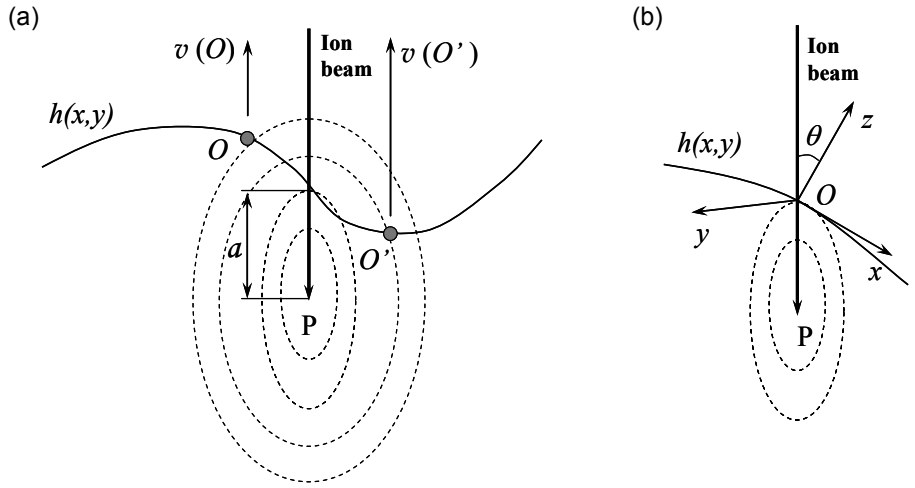

Fig. 3.1: Erosion of a corrugated surface by an ion beam. (a) The incident ion beam (bold solid arrow) penetrates an average distance, *a*, inside the solid and will be stopped at point P due to collisions, losing energy. *O* and *O'* are surface atoms on the crest and in the valley, correspondingly. P is the point of energy deposition; the dotted ellipses show contours of equal energy deposition (after [Sig73]). (b) Ion erosion at point *O* is shown in *local* coordinates (after [MCB02]).

The first theoretical approach, describing ripple formation by ion-beam sputtering, was proposed by Bradley and Harper [BrH88]. The modeling exploits the dependence of the erosion velocity [Sig69], v, on the average energy deposited at a point P(x,y,z) by an ion (Fig. 3.1 (b)). Taking into account that the erosion velocity, v, is a function of incidence angle, θ, and a local surface curvature, R, and adding a surface self-diffusion term, we obtain the time evolution of the growing surface profile $h(x,y)$:

$$\frac{\partial h}{\partial t} = -v(\theta, R)\sqrt{1+(\nabla h)^2} - K\nabla^2\nabla^2 h \qquad (3.1)$$

Now, let us consider the first term on the right-hand side of Eq. (3.1). As indicated in Fig. 3.2, removal takes place in a direction locally normal to the interface. When a particle is removed, the increment, $v\Delta t$, projected along the h axis is Δh. Following the geometry of the problem, from a right triangle we find Δh as (cf. Fig. 3.2):

$$\Delta h = \left[(v\Delta t)^2 + (v\Delta t \tan\alpha)^2 \right]^{1/2} \qquad (3.2)$$

Taking into account that $\tan\alpha = \frac{dh}{dx}$, Eq. (3.2) results in the first term of Eq. (3.1):

$$\frac{\partial h}{\partial t} = v\left[1 + (\nabla h)^2\right]^{1/2} \tag{3.3}$$

The second term on the right-hand side in Eq. (3.1) describes the surface self-diffusion of atoms, where the diffusion coefficient K is given by

$$K = \frac{D_S \gamma \nu}{n^2 k_B T} \exp\left(-\frac{\Delta\varepsilon}{k_B T}\right) \tag{3.4}$$

Here D_S is the surface self-diffusivity, γ the surface free energy per unit area, ν the real density of diffusing atoms and $\Delta\varepsilon$ the activation energy for surface self-diffusion [BrH88].

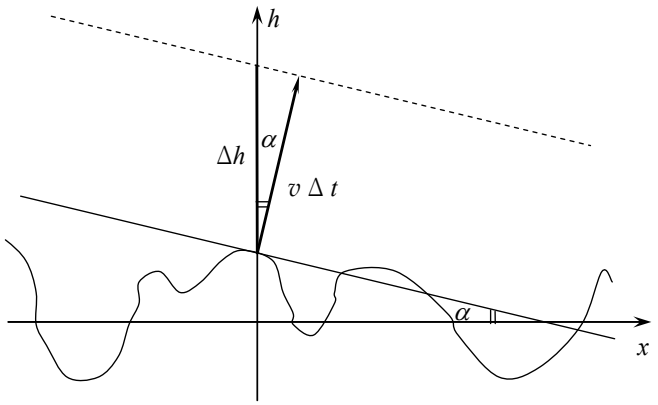

Fig. 3.2: Influence of a surface local curvature on the erosion velocity $v(h)$ (analogous to [KPZ86]).

Eq. (3.1) is an equation of Kardar-Parisi-Zhang type [KPZ86] and its solution predicts the formation of periodic surface structures with orientation and wavelength Λ depending on the incident angle of the ion beam, θ, and, in special cases, depending on the surface temperature, T, diffusion coefficient, K, and the activation energy for surface self-diffusion, $\Delta\varepsilon$:

$$\Lambda(\theta) \propto \frac{K}{\sqrt{T}} \exp\left(-\frac{\Delta\varepsilon}{kT}\right) \tag{3.5}$$

3.2. Model

The geometry of the model is illustrated in Fig. 3.3. The figure shows the laboratory frame (x,y,h) with h perpendicular to the *flat* substrate, the *local* surface frame (X,Y,Z) taking into account surface corrugation with radius R, and the frame (x',y',z')

connected with the incident laser beam propagating in the direction parallel to *z'*, as well as the azimuthal and elevation angles connecting these frames. Though the incidence angle of the beam can vary (cf. Fig. 3.1 (b)), here, for simplicity, we consider normal incidence to the flat surface. The laser beam is incident on the target surface and is absorbed in some point *P*, from where its energy is further transferred (cf. dotted ellipses in Fig. 3.3 and Fig. 3.5) to the neighboring sites. In contrast to the ion-beam sputtering model [Sig69], [BrH88], [MCB02], where energy distribution is isotropic in the plane of the incident beam, i.e. $\alpha = \beta$, the exciting field of polarized laser irradiation induces an asymmetry in the ionized kinetic energy distribution ($\alpha \neq \beta$) that results in a corresponding asymmetric energy transfer [RVV11].

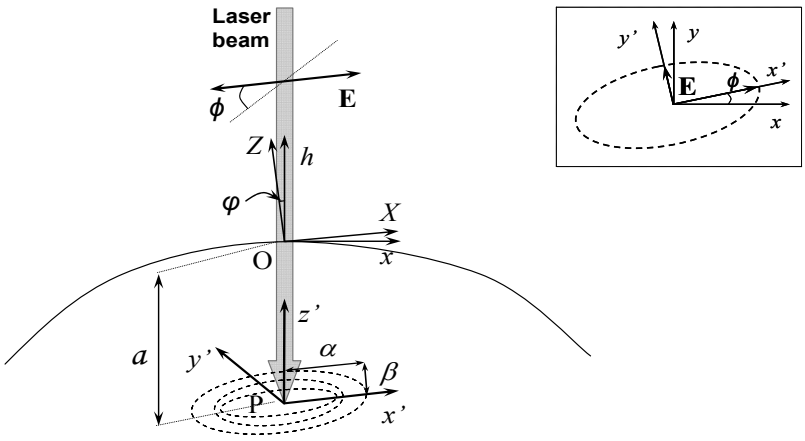

Fig. 3.3: Reference frames for the computation of the erosion velocity: (*x',y',z'*) is the reference frame of the incoming beam, *x'* is parallel to the vector E of the electromagnetic field; (*X,Y,Z*) corresponds to the local coordinate frame, where *Z* is parallel to the local normal to the surface, while (*x,y,h*) denotes the laboratory frame of coordinates with *h* perpendicular to the flat substrate surface. The dotted ellipse is a Gaussian distribution of deposited energy with half-width α, β along *x', y'*, respectively. The energy distribution along *z'* with half-width γ is not shown here. φ is the angle between the local and the laboratory reference frames (corrugation) and denotes the "local" incidence angle; ϕ is orientation of E in the plane of incidence (*x,y*). Insert: view of the plane of incidence.

Following Peter Sigmund's theory of ion sputtering [Sig69], we can relate the erosion velocity normal to the surface to the energy input:

$$v \cong \xi \int_V dr^3 \psi(r) \varepsilon(r) \tag{3.6}$$

where the integration is performed over the volume *V*, including all points, at which the deposited energy contributes to the erosion velocity v at the surface. ξ is a material parameter, $\psi(r)$ takes into account local variations of the deposited energy due to

attenuation, refraction and reflection. In principle, $\psi(r)$ contains all information about spatial beam profile, absorption cross section, and losses along the beam pass to reach $P(r)$. $\varepsilon(r)$ is the fraction of that energy dissipated to the surface after absorption at $P(r)$ and resulting in erosion. To evaluate $\varepsilon(r)$, we have to take into account the dynamics of femtosecond laser-matter interaction.

Similarity of the laser-induced instability on the target surface to the well-known hydrodynamic instability of thin liquid films (cf. sec. 2.3.1) allows us to use an analogous approach as in that case and to describe the time evolution of the surface height profile $h(x,y,t)$, caused by surface erosion [CuB95], with the Eq. (3.1), where the erosion velocity is a function not only of the local surface curvature (φ, R) and of the incident angle of the laser beam (θ) (cf. Fig. 3.2), but depends also on the orientation of the laser electric field denoted by angle ϕ in Fig. 3.3.

3.2.1. The role of anisotropic excitation

The absorbed laser energy results only in an excitation of electrons. In dielectrics and semiconductors, electrons are excited from the valence to the conduction band. These electrons thermalize their kinetic energy first by collisions with the other conduction electrons and then, only subsequently, transfer the energy to the lattice by electron-phonon collisions.

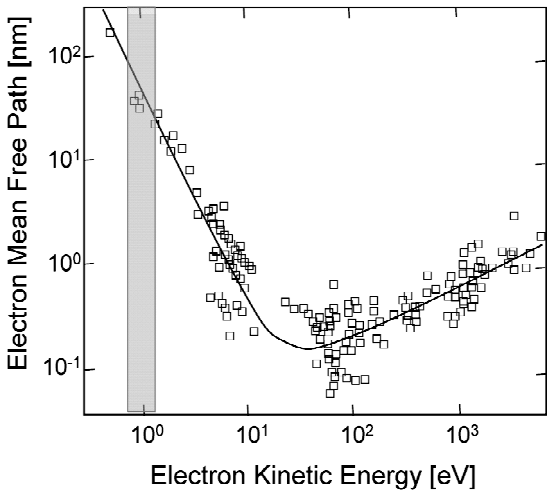

Fig. 3.4: The "Universal Curve" of electron mean free path vs. electron kinetic energy. The grey square indicates the region of typical kinetics energies in the considered situation (from [Rei09]).

One possible origin of asymmetry in such energy transfer is based on the initial photoionization, i.e. the excitation from the valence into the conduction band. It is well known from the photoionization of free atoms that the electric light field results in an asymmetric distribution of electron kinetic energy: the electrons' velocity is larger in

the field direction and less in all other directions. On the other hand, the electron mean free pass strongly depends on their kinetic energy [Zan88] and decreases more than one order of magnitude in the range between 0.5 eV and 10 eV [Rei09], as a consequence of a reciprocal variation of collision − and thus energy transfer − probability (Fig. 3.4).

Consequently, assuming Gaussian velocity distributions for the electrons, we can approximate the contribution of energy absorbed at *P* to the erosion velocity:

$$\varepsilon(r') \propto \exp\left[\left(\frac{x'^2}{\delta_{x'}}\right)+\left(\frac{y'^2}{\delta_{y'}}\right)+\left(\frac{z'^2}{\delta_{z'}}\right)\right] \tag{3.7}$$

Here δ_k are the relative energy coupling cross sections in k direction ($k = x',y',z'$) (Fig. 3.5) and thus reciprocal to the relative mean free path, α, β and γ in Fig. 3.3.

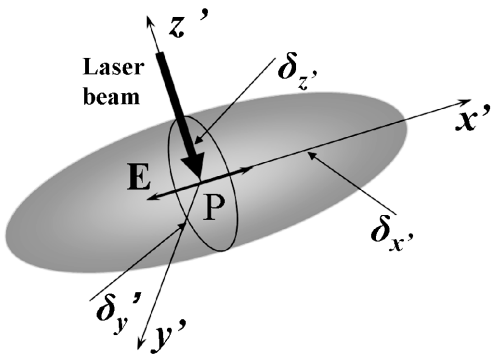

Fig. 3.5: Ellipse illustrates cross sections of relative collisional energy transfer after laser excitation at point P in frame of incoming beam (x’,y’,z’). Linear polarized laser beam propagates along z’; vector E defines direction of linear polarization (E∥x’).

Another possible reason for the initial anisotropy is the resonant polarization dependent excitation of surface plasmon-polaritons (SPPs) on a corrugated interface conductor/vacuum [MiM08], [GCP11], where absorption is largest for E parallel to the *k*-vector of the corrugation.

3.2.2. Evolution of the surface profile

Let’s return to the time evolution of the surface height profile as it was described in section 3.2 and Fig. 3.3. Whereas in Sigmund’s theory [Sig69] the parameters α, β and γ along x', y' and z', respectively, are scaled as $\alpha = \beta \geq \gamma$, in the case of light-matter interaction we no longer have the same constant ratio between these three components. The relation between α and β depends on the characteristics of

irradiation, absorption and dissipation; and γ is a constant that corresponds to a thin layer a (cf. Fig. 2.8 and Fig. 3.3), generally determined by the mean free path of conduction band electrons.

Following Refs. [BrH88], [CuB95] we have to perform the calculation of the erosion rate in the local coordinate system (X,Y,Z). This means that we need to transform the deposited energy $\varepsilon(r)$ (Eq. (3.7)) from (x',y',z') to the local (X,Y,Z) reference frame by means of rotation:

$$\begin{pmatrix} x' \\ y' \\ z' \end{pmatrix} = \begin{pmatrix} \cos\phi\cos\varphi & \sin\phi & \cos\phi\sin\varphi \\ -\sin\phi\cos\varphi & \cos\phi & -\sin\phi\sin\varphi \\ -\sin\varphi & 0 & \cos\varphi \end{pmatrix} \cdot \begin{pmatrix} X \\ Y \\ Z \end{pmatrix} \tag{3.8}$$

and subsequent translation along the beam direction by a. To simplify our consideration we restrict our calculations to the case of small incident angles θ in optically transparent materials. The local correction to the incident energy flux is now given by $\psi(r) = \mathrm{A} \cdot I_0(\cos\varphi + (\partial Z/\partial X)\sin\varphi)$, where A is the generalized absorption coefficient[3] of the material and I_0 is the laser intensity. In order to describe the surface profile in the neighborhood of O (Fig. 3.3), we took into account cross-terms of the type $\sim XY$

$$Z(X,Y) \cong -\frac{1}{2}\left(\frac{X^2}{R_X} + \frac{Y^2}{R_Y}\right) - \frac{XY}{R_{XY}} \tag{3.9}$$

As in Ref. [CuB95]we assume that the radii of curvature R_X, R_Y and R_Z of the surface are much larger than a, which in this case means the distance from the surface to the absorption point P, so that only terms up to first order in a/R_X, a/R_Y and a/R_Z are kept. The integration results in the erosion velocity $v(\varphi, \phi, R_X, R_Y, R_{XY})$ as a function of angles φ, ϕ, and the curvatures:

$$\frac{1}{R_X} = -\frac{\partial^2 Z}{\partial X^2}, \qquad \frac{1}{R_Y} = -\frac{\partial^2 Z}{\partial Y^2}, \qquad \frac{1}{R_{XY}} = -\frac{\partial^2 Z}{\partial X \partial Y}. \tag{3.10}$$

[3] Note that, for multiphoton absorption in transparent media, A will be of the form $A_0 I^{n-1}$.

Now, we examine the evolution of the surface corrugation $z=h(x,y,t)$ with time t, starting from an originally flat configuration (h=0). We rewrite v in terms of the laboratory coordinates (x,y,h) [CuB95]:

$$\frac{\partial h(x,y,t)}{\partial t} = -v(\varphi,\phi,R_X,R_Y,R_{XY})\sqrt{1+(\nabla h)^2} \tag{3.11}$$

We expand Eq. (3.11) in a Taylor series and complete it by adding surface self-diffusion (cf. (3.1)) and the statistical fluctuations of initial surface roughness $\eta(x,y,z)$ (shot noise). Finally, we obtain the equation of motion known as an anisotropic noisy Kuramoto-Sivashinsky [KuT77], equation:

$$\begin{aligned}\frac{\partial h}{\partial t} &= -v_0 + \nu_x\frac{\partial^2 h}{\partial x^2} + \nu_y\frac{\partial^2 h}{\partial y^2} + \nu_{xy}\frac{\partial^2 h}{\partial x\partial y} + \frac{\lambda_x}{2}\left(\frac{\partial h}{\partial x}\right)^2 + \frac{\lambda_y}{2}\left(\frac{\partial h}{\partial y}\right)^2 \\ &+ \frac{\lambda_{xy}}{2}\left(\frac{\partial h}{\partial x}\right)\left(\frac{\partial h}{\partial y}\right) - K\nabla^2\left(\nabla^2 h\right) + \eta(x,y,z),\end{aligned} \tag{3.12}$$

where the coefficients are now the complex functions of two angles ϕ and θ. For the case of normal incidence illustrated in Fig. 3.3, the coefficients take the form:

$$\begin{aligned}\nu_x &= -\frac{Fa}{2\gamma}\left(\frac{\alpha^2}{\gamma^2}\cos^2\phi + \frac{\beta^2}{\gamma^2}\sin^2\phi\right), \\ \nu_y &= -\frac{Fa}{2\gamma}\left(\frac{\alpha^2}{\gamma^2}\sin^2\phi + \frac{\beta^2}{\gamma^2}\cos^2\phi\right), \quad \nu_{xy} = -\frac{Fa}{2\gamma}\left(\frac{\beta^2}{\gamma^2} + \frac{\alpha^2}{\gamma^2}\right)\sin 2\phi, \\ \lambda_x &= -\frac{F}{\gamma}\left[1 + \left(\frac{\alpha^2}{\gamma^2} - 1\right)\left(\frac{\alpha^2}{\gamma^2}\cos^2\phi + \frac{\beta^2}{\gamma^2}\sin^2\phi\right)\right], \\ \lambda_y &= -\frac{F}{\gamma}\left[1 + \left(\frac{\alpha^2}{\gamma^2} - 1\right)\left(\frac{\alpha^2}{\gamma^2}\sin^2\phi + \frac{\beta^2}{\gamma^2}\cos^2\phi\right)\right], \\ \lambda_{xy} &= -\frac{F}{\gamma}\left(\frac{\alpha^2}{\gamma^2} - 1\right)\left(\frac{\beta^2}{\gamma^2} - \frac{\alpha^2}{\gamma^2}\right)\sin 2\phi, \quad v_0 = \frac{F}{\gamma}\end{aligned} \tag{3.13}$$

and the absorbed fluence $F = \frac{I_0\xi\,\mathrm{A}}{\sqrt{2\pi}}\exp\left(\frac{a^2}{2\gamma^2}\right)$, where ξ is a material parameter (cf. Eq. (3.6)).

In order to extract the physical meaning from Eqs. (3.12) and (3.13), we consider, in this approach, the special case $\nu_{xy} = 0$ and $\lambda_{xy} = 0$. That means Eqs. (3.12), (3.13) are

taken in the reference frame rotated by the angle ϕ (cf. insert in Fig. 3.3). Moreover, we neglect here the erosion velocity of the initial flat surface v_0, which does not effect the size of ripples and can be eliminated by the transformation $\tilde{h} = h + v_0 t$.

$$\frac{\partial h}{\partial t} = \nu_x \frac{\partial^2 h}{\partial x^2} + \nu_y \frac{\partial^2 h}{\partial y^2} + \frac{\lambda_x}{2}\left(\frac{\partial h}{\partial x}\right)^2 + \frac{\lambda_y}{2}\left(\frac{\partial h}{\partial y}\right)^2 - K\nabla^2\left(\nabla^2 h\right) + \eta(x,y,z), \tag{3.14}$$

where the coefficients are given now by

$$\begin{aligned} \nu_{x,y} &= -\frac{F}{2}\sigma_\gamma \Omega_{x,y} \\ \lambda_{x,y} &= -\frac{F}{\gamma}\left[1 + \left(\sigma_\gamma^2 - 1\right)\Omega_{x,y}\right] \end{aligned} \tag{3.15}$$

and

$$\Omega_{x,y} = \Delta\left[1 \pm \Pi\right]; \qquad \Delta = \frac{1}{2}\left(\frac{\sigma_\gamma^2}{\sigma_\alpha^2} + \frac{\sigma_\gamma^2}{\sigma_\beta^2}\right); \qquad \Pi = \frac{\sigma_\beta^2 - \sigma_\alpha^2}{\sigma_\beta^2 + \sigma_\alpha^2}; \qquad \sigma_i = \frac{a}{i}(i = \alpha, \beta, \gamma) \tag{3.16}$$

Polarization parameter Π describes an asymmetry of energy distribution in the (*x'y'*) plane; *depth parameter* Δ takes into account energy deposition also along the *z'* axis (Fig. 3.3), connected with the direction of laser beam propagation. Combinations of Π and Δ result in *anisotropy parameter* Ω in Eq. (3.16) which determines the spatial asymmetry in energy distribution at point *P*.

3.2.3. Linear stability analysis

In this section the basic role of polarization and depth parameters, Π and Δ, will be explained by means of a linear stability analysis of Eq. (3.14). For this purpose, we introduce a periodic perturbation $h = h_0 \exp\left[i(q_x x + q_y y - \omega t) + \sigma t\right]$ and obtain the normalized growth rate

$$\Sigma =: \frac{1}{h_0}\frac{\partial h}{\partial t} = -\left[\nu_x q_x^2 + \nu_y q_y^2 + K(q_x^2 + q_y^2)^2\right]. \tag{3.17}$$

From Eqs. (3.15) and (3.16) it follows that polarization and depth parameters contribute to the two tension coefficients $\nu_{x,,y}$, which are negative for normal incidence

and in general are not equal to each other because of the fact that Π increases ν_x and reduces ν_y. Fig. 3.6 shows the linear growth rate Σ along perturbation wave vectors q_x and q_y for various values of parameters Δ and Π. For Δ=0 the uniform state is stable (ν_x=ν_y=0), whereas for nonzero Δ and Π=0 we obtain equal instability along q_x and q_y (ν_x=ν_y= $-(F\sigma_y/2)\Delta$). Distinct from zero, the value of Π induces an asymmetrical instability in the q_{xy}-plane with the wave vector:

$$q_{x,y}^{*} = \sqrt{\frac{F\sigma_\gamma}{4K}\Delta[1 \pm \Pi] - q_{y,x}^{2}} \tag{3.18}$$

An increase of Π shifts the instability to higher values of q_x (ν_x= $-(F\sigma_y/2)\Delta[1+\Pi]$) and suppresses the instability along q_y (ν_x= $-(F\sigma_y/2)\Delta[1-\Pi]$). Thus, for Π~1 the instability along q_y disappears.

From the stability analysis of Fourier modes for Eq. (3.14), we expect the instability for the ripple formation with wavelength $\Lambda_i = 2\pi\sqrt{2K/|\nu_i|}$, where i refers to the x or y direction along which the corresponding ν_i is largest. Thus, in the case of ν_x $<\nu_y<0$, which holds when $0<\Pi<1$, the ripple structure is oriented in x direction with the following wavelength of the surface modulations:

$$\Lambda_{x,y} = 4\pi\sqrt{\frac{K}{F\sigma_\gamma\Delta(1 \pm \Pi)}} \tag{3.19}$$

For the "zero" polarization parameter (Π=0), the wavelength of ripples along x and y axis are equal: Λ_x=Λ_y. An increase of Π slightly reduces Λ_x whereas Λ_y becomes very large for $\Pi \to 1$. Eq. (3.19) has revealed the influence of polarization parameter Π on the experimentally measured ripple characteristics Λ_x, Λ_y (period and bifurcation length). From the relation $\Lambda_x/\Lambda_y = \sqrt{(1-\Pi)/(1+\Pi)}$ the polarization parameter Π and, correspondingly, polarization of the incident laser field, can be determined.

We can consider the polarization parameter as a control parameter that represents a degree of anisotropy in the energy deposition and, therefore, the orientation of ripple formation. Indeed, from Eq. (3.16), Π=0 corresponds to an equal energy deposition (α=β, isotropic energy distribution) along x and y axes, whereas, Π~1 describes the case $\alpha >> \beta$ (energy flow in x, parallel to E).

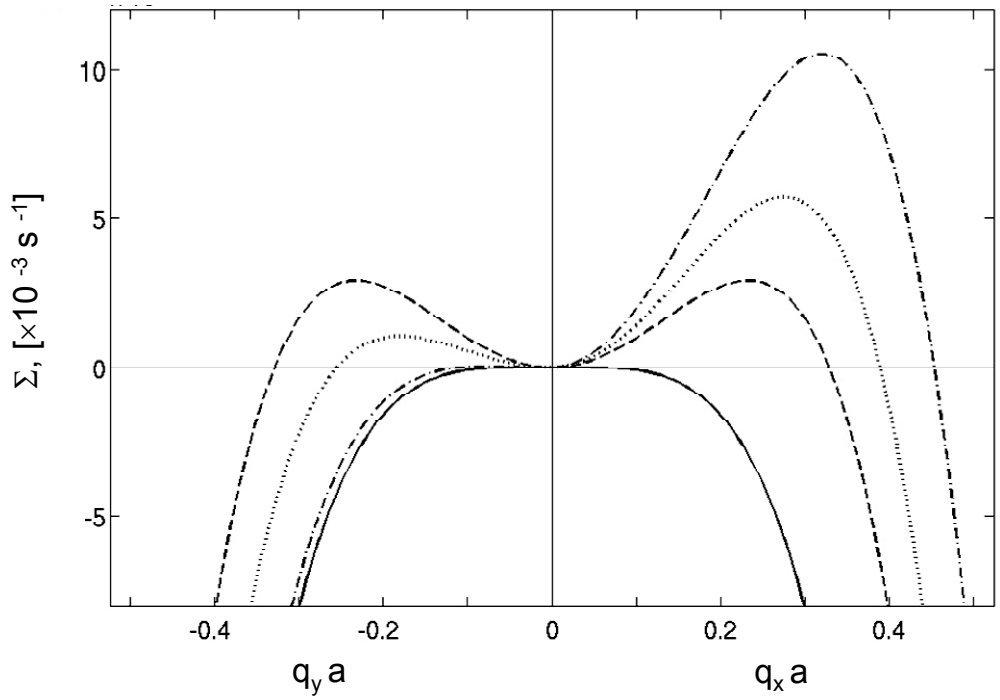

Fig. 3.6: Growth rate Σ as a function of two dimensionless wave vectors $q_x a$ and $q_y a$ for various values of parameters Δ and Π: Δ=0, Π=0 (solid line); Δ=1, Π=0 (dashed line); Δ=1, Π=0.4 (dotted line); Δ=1, Π=0.9 (dash-dotted line).

To summarize, it has been shown that polarization parameter Π, characterizing the symmetry of the deposited energy distribution in the (*x',y'*) plane (Fig. 3.3), determines the orientation and also the morphology of the calculated pattern. The anisotropy in the energy distribution is correlated with the vector E of the incoming laser field in such a manner that E defines the preferred direction of the energy transfer. In the next subsection we discuss a morphological diagram and identify the direction of the preferred energy transfer with the vector of polarization E.

3.2.4. Morphological diagram for the ripple orientation

Another quantity that can change the ripple orientation is the angle of incidence θ. It is very important to note that the orientation of the ripple due to the polarization and that due to the incidence angle θ can compete or work together. Such behavior is one prediction of this theory that has been tested experimentally. The general expressions being too complicated, we present here ν_x and ν_y in the reference frame rotated by angle ϕ:

$$\nu_x = -\frac{F\sigma_\gamma}{2\zeta^2}\left(\frac{\sigma_\gamma^2}{\sigma_\alpha^2}\right)\times$$
$$\left[\cos^2\theta - 2\sin^2\theta\left(1-\frac{\sigma_\gamma^2}{2\zeta}\cos^2\theta\right)\left(\frac{\sigma_\gamma^2}{\sigma_\alpha^2}\right)\right], \qquad (3.20)$$
$$\nu_y = -\frac{F\sigma_\gamma}{2\zeta}\left(\frac{\sigma_\gamma^2}{\sigma_\beta^2}\right)\cos^2\theta,$$

where $\zeta = \cos^2\theta + (\sigma_\gamma^2/\sigma_\alpha^2)\sin^2\theta$ and by using Eq. (3.16) we express the $\sigma_\gamma^2/\sigma_\alpha^2$ and $\sigma_\gamma^2/\sigma_\beta^2$ in terms of Δ and Π:

$$\left(\frac{\sigma_\gamma^2}{\sigma_\alpha^2}\right) = \Delta(1+\Pi) \text{ and } \left(\frac{\sigma_\gamma^2}{\sigma_\beta^2}\right) = \Delta(1-\Pi). \qquad (3.21)$$

In contrast to ion beam sputtering [BrH88], [CuB95], the most important parameter that influences the orientation of ripples in our consideration is the polarization parameter Π. Therefore, we study here the (Π, θ) morphological diagram for different values of σ_y. The boundary in the diagram is defined by $\nu_x(\Pi,\theta) = \nu_y(\Pi,\theta)$ and separates the region I ($\nu_x < \nu_y$), with the ripples' wave vector in *y*-direction, and region II ($\nu_x > \nu_y$), with the ripples' wave vector in *x*-direction.

We start to discuss the diagram from the bottom (the left Insert in Fig. 3.7), where for small θ the wave vector of ripples is aligned along E and is perpendicular to the component of the beam in the surface plane. Thus, for small θ the orientation of ripples is defined by E and the influence of the angle of incidence is not appreciable. With the increase of θ the growing angle of incidence supports the effect of polarization and the wave vector of ripples remains along E, which is shown in the bottom of diagram in the right Insert.

In the case of weak polarization, $-0.4 \le \Pi < 0$, a reorientation of ripples in dependence on θ can be observed for $\sigma_y > 1$. Indeed, one can see from the diagram in the case of Π=0 that the increase of θ from zero (normal incidence) to some finite values reveals two possibilities: the wave vector of ripples is aligned parallel and perpendicular to the component of the incoming beam in the Region I and Region II, respectively; and the border between these two regions is determined by the parameter σ_y. In the case of Π=0 and at normal incidence some isotropic structures are expected in the model. This is also proved experimentally: at non-normal incidence an

arrangement of nano-spheres typical for circular polarization turns into a linear pattern with the wave vector of modulations oriented parallel to the incoming irradiation (Fig. 3.7, Fig. 5.6). This comparison helps us to fix partially the parameter σ_y for the following numerical calculations.

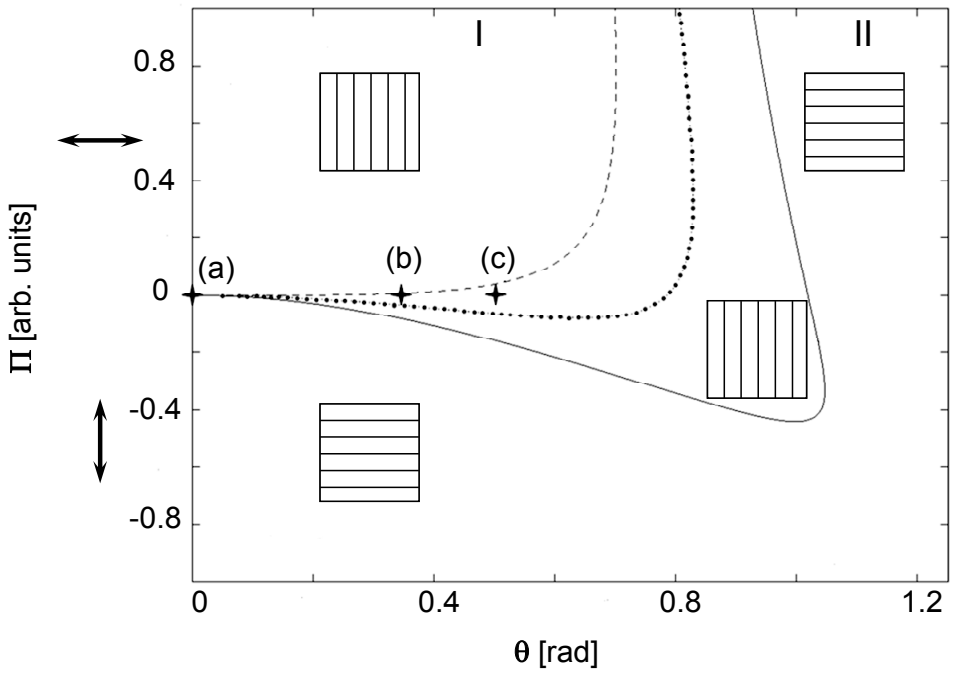

Fig. 3.7: Ripple orientation diagram for different values of σ_y=1; 1.5; 2 (dashed, dotted, solid line, respectively). Region I: $\nu_x<\nu_y$; region II: $\nu_x>\nu_y$. Direction of the vector E is indicated with double arrows. Inserts show the direction of ripples. (a), (b) and (c) correspond to the surface morphologies in Fig. 5.6.

Further, the model allows us to understand the nature of LIPSS, which are oriented parallel to the laser polarization at a relatively large angle of incidence. To see this, we move to the positive values of Π, considering the vector E along the *x* axis. As expected, the polarization aligns the wave vector of ripples along the *x* direction for small θ. The growth of θ can change the direction of ripples for Π>0 at some critical angle θ_c, which depends on σ_y. Nevertheless, one should mention here that the approximation is not valid for a large angle of incidence, where the interaction effects of the laser irradiation with the material surface cannot be neglected. Therefore, in this work the numerical results will be presented only for the normal incidence of the laser beam and we set $\sigma_y \cong 1.5$.

3.2.5. Nonlinear regime

Closer examination of Eq. (3.14) reveals that its time dependence consists of a linear part and nonlinear components. Let us consider the influence of the nonlinear terms λ_x

and λ_y. Such separation of linear and nonlinear behavior in time assumes the existence of a crossover time t_c that separates these two regimes [PKJ99]. In the linear regime up to t_c the nonlinear terms are negligible, whereas they take over after

$$t_c \propto \left(\frac{K}{\nu^2}\right)\ln\left(\frac{\lambda}{\nu}\right) \tag{3.22}$$

and completely determine the surface morphology, which depends on the relative signs of λ_x and λ_y. The transition between the linear and nonlinear regimes is very abrupt, and it is followed by the appearance of kinetic roughening. For $\sigma_y = 1.5$ both λ_x and λ_y are negative and depend on Π. The dependence of the crossover time on the polarization can be presented as follows:

$$t_c(\Pi) \propto \frac{t_c(\Pi = 0)}{(1+\Pi)^2}, \tag{3.23}$$

where t_c is decreased with increasing of Π.

3.3. Numerical results and discussion

The numerical integration of Eq. (3.12) is performed by means of a semi-implicit pseudo-spectral method, where the linear part is considered at the new time step $t+\Delta t$:

$$\begin{aligned}&\left(\frac{1}{\Delta t} - \nu_x\frac{\partial^2}{\partial x^2} - \nu_y\frac{\partial^2}{\partial y^2} - \nu_{xy}\frac{\partial^2}{\partial x\partial y} + K\nabla^4\right)h(t+\Delta t) = \\ &\frac{h(t)}{\Delta t} + \frac{\lambda_x}{2}\left(\frac{\partial h(t)}{\partial x}\right)^2 + \frac{\lambda_y}{2}\left(\frac{\partial h(t)}{\partial y}\right)^2 + \frac{\lambda_{xy}}{2}\left(\frac{\partial h(t)}{\partial x}\right)\left(\frac{\partial h(t)}{\partial y}\right) + \eta(x,y,z)\end{aligned} \tag{3.24}$$

In the Fourier domain Eq. (3.24) is equivalent to

$$H(k,t+\Delta t) = \left(\frac{1}{\Delta t} + \nu_x k_x^2 + \nu_y k_y^2 + Kk^4\right)^{-1} N(k,t), \tag{3.25}$$

where $H(k,t+\Delta t)$ and $N(k,t)$ denote the Fourier transforms of $h(x,t+\Delta t)$ and of the rhs of Eq. (3.24), respectively. An additional inverse Fourier transform will reassemble $h(x,t+\Delta t)$, necessary for the next iteration step, from $H(k,t+\Delta t)$. Moreover, we scale space and time variables in the following way:

$$h = ah', \quad x = ax', \quad y = ay', \quad t = \left(a^2 / I_0 \, \xi \, A\right) t' \tag{3.26}$$

and calculate the dimensionless height of the eroded surface of size $64\pi \times 64\pi$.

3.3.1. Influence of polarization

Surface patterns obtained by numerical integration of Eq. (3.12) and corresponding Fourier images (2D-FTT) are presented in Fig. 3.8. The calculated morphologies for various values of parameters ϕ, Π and simulation time t show that an asymmetric energy deposition can describe the correlation of ripple orientation with laser polarization. Π is the degree of asymmetry in the energy deposition that can be also associated with the polarization degree of laser irradiation. ϕ describes the orientation of the vector E in the laboratory frame *(x,y,h)*. The simulation time t will be measured in arbitrary units (a.u.) and will be discussed in the next section. Note for a later comparison that, in contrast to pulsed excitation in experiment, here the continuum time evolution.

In Fig. 3.8 (a) we observe the surface morphology calculated for Π=1, ($\sigma_\alpha << \sigma_\beta$), t = 800 a.u. and $\phi = 0$. That means the energy distribution along *x'* is much larger than along *y'*. The pattern consists of periodic parallel lines, oriented perpendicular to E. This is similar to the ripples produced by a linearly polarized laser beam (Fig. 5.1 (a)). By rotation of vector E ($\phi = 45°$) for the same values of Π and t, the ripples follow the direction of the incident electrical field (Fig. 3.8 (b)), which is also in good agreement with the experiment (Fig. 5.1 (b)). By the variation of Π, between zero and one ($\sigma_\alpha < \sigma_\beta$), and a fixed angle $\phi = 90°$, we create the configuration of elliptic polarization. The large axis of the polarization ellipse is oriented along y-axis in the laboratory coordinate frame *(x,y,h)* (Insert in Fig. 3.3). As can be seen from Fig. 3.8 (c) (t = 1400 a.u.) the ripples are still aligned to the large axis of the polarization ellipse, again consistent with the experiment for elliptic polarized irradiation (e. g. Fig. 5.2 (c), (g)). For Π=0, ($\sigma_\alpha = \sigma_\beta$), i.e. circular polarization, we have a symmetrical energy distribution with respect to *x'* and *y'*. The calculated surface morphology for t = 3000 a.u. does not possess a linear order, the pattern is uniformly distributed (Fig. 3.8 (d)). A similar kind of pattern, characterized by lack of linear order and consisting of arrays of uniformly distributed dots, is observed with laser ablation with circularly polarized pulses (Fig. 5.3).

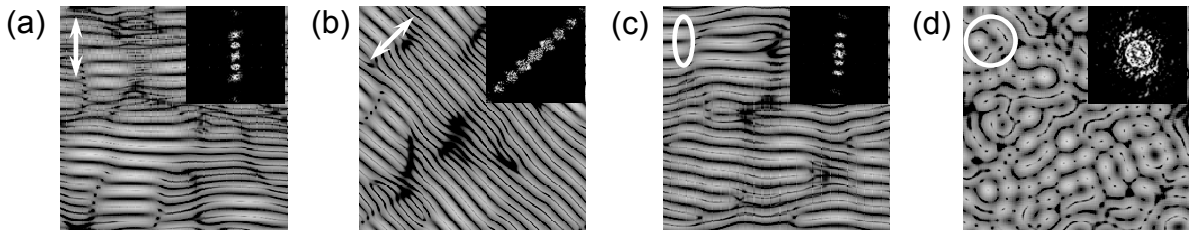

Fig. 3.8: Numerically calculated surfaces of size 64π×64π in a.u., showing the surface morphologies for (a) ϕ =90°, Π = 1, t = 800 a.u.; (b) ϕ =45°, Π = 1, t = 800 a.u; (c) ϕ =90°, Π = 0.5, t = 1400 a.u.; (d) ϕ =90°, Π = 0, t = 3000 a.u.; white double arrows and elliptical figures define the energy distribution in the (*x'y'*)-plane.

3.3.2. Period of numerically calculated pattern

By irradiation of a flat surface with ultrashort laser pulses at an intensity above a threshold value, we induce in the illuminated area a high degree of instability, and pattern formation sets in. From our linear stability analysis of the rate equation (3.14), describing the time profile evolution of the irradiated surface, we expect instability for the "ripple formation" with the wavelength [BrH88]

$$\Lambda_i = 2\pi\sqrt{\frac{2K}{|\nu_i|}}, \tag{3.27}$$

where K is the specific surface self-diffusion coefficient, ν_i are the tension coefficients in Eq. (3.14) and i refers to the direction (x or y) of energy transfer after laser excitation (Fig. 3.3, Fig. 3.5). Assuming the proportionality of ν_i to the incident laser fluence F (Eq. (3.15)), we obtain that the ripple wavelength Λ depends only on the laser energy coupled into the material F and on the specific surface self-diffusion coefficient K:

$$\Lambda \propto \sqrt{\frac{K}{F}}. \tag{3.28}$$

This at first sight confusing relation between ripple wavelength and fluence can be explained by taking into account the dependence of the specific self-diffusion coefficient K on the surface temperature T, describing by the Arrhenius law:

$$K \propto \frac{1}{kT}\exp\left(-\frac{E_a}{kT}\right), \tag{3.29}$$

where E_a is the activation energy for surface self-diffusion. Assuming a linear increase of the surface temperature with the laser fluence [CSB99], $T \propto F$, we can rewrite Eq. (3.28) in the following form $\Lambda \propto \frac{1}{F}\exp\left(-\frac{E_a}{2bF}\right)$, where b characterizes the properties of a high-excited state of material, F corresponds to the laser irradiation dose and E_a is the activation energy for the thermal desorption.

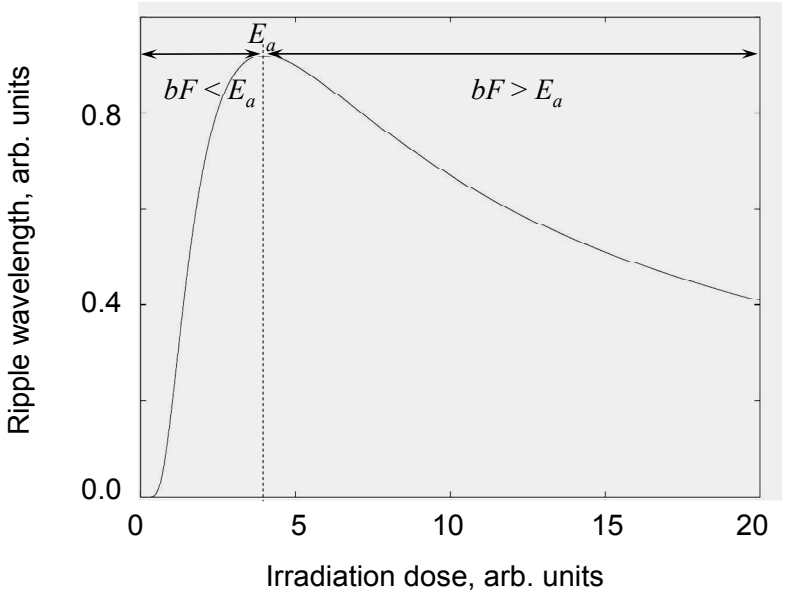

Fig. 3.9: Dependence of the ripple wavelength on the applied irradiation dose.

The graphical interpretation of this Arrhenius-like dependence is shown in Fig. 3.9. Here, we observe an exponential growth of the ripples wavelength with irradiation dose, when $bF < E_a$ (Fig. 3.9). This case corresponds to the "gentle" ablation regime of dielectrics and semiconductors. When the applied irradiation dose exceeds the activation energy for thermal desorption (the region $bF > E_a$ in Fig. 3.9), we expect a decrease of the ripple periods with increasing irradiation dose.

Whereas the numerically calculated surfaces in Fig. 3.8 are of size $64\pi \times 64\pi$ in dimensionless units (h', x', y'), we can return to physical sizes (h, x, y), taking in account the scaling of space variables performed by the calculation (see Eq. (3.26)). Considering the typical irradiation with ultrashort Ti:Sapphire laser pulses (800 nm, 100 fs), we expect the resulting electron kinetic energy to be up to ~1.5 eV and, consequently, the mean free pass for the "hot" electrons increases up to some tens of nanometers [Zan88]. Excited electrons can leave the target at a depth less than their mean free pass, forming the electron's depleted surface layer of thickness a. If we

admit that the value of a is varied from 10 to 40 nm in dependence on the kinetic energy of electrons, the period of calculated structures will be, respectively, in the range from 100 to 500 nm, which corresponds to our experimental observation.

3.3.3. Consideration of a positive feedback in the model

One of the major motivations for application of the self-organized mechanism of ripple formation is the belief that with this model we can understand a number of effects, which cannot be described in the framework of the standard LIPSS theory [EHW73], [SYP83], [MiM08]. In particular, significant pulse-to-pulse feedback effect, which manifests itself in the irradiation dose dependence of the ripple wavelength, is naturally explained by the model.

For the best understanding of the pulse-to-pulse feedback, let's express the temperature dependence of the ripple wavelength in Eq. (3.19), taking into account the specific self-diffusion coefficient K (Eq. (3.29)), in the following form [MCB02]:

$$\Lambda \propto (I\,T)^{-1/2} \exp(-E_a / 2k_B T), \tag{3.30}$$

where I is laser intensity. Keeping in mind the linear dependence between I and the surface temperature T [CSB99] and assuming the activation energy E_a=0.67 eV for the surface diffusion [MKW91] for Si, one can estimate that an increase of I by a factor of two will result in 1.4 times magnification of the ripple wavelength, correlating well with experimental results (e. g. Fig. 5.5 and Fig. 5.15).

It would appear reasonable that this dependence of the ripple wavelength on surface diffusion is responsible for the increase of the features size from the edge to the center in the ablated spot, assuming the Gaussian beam profile. Moreover, the "collective" action of subsequent pulses, leading to a raise of the ripple wavelength with the pulse number, makes itself evident that the surface temperature may increase from pulse to pulse. Numerical calculation based on Anisimov's two-temperature model [AKP74] has been revealed a heating of the irradiated surface approximately on 10 K between first and twentieth pulse separated by 0.1 ms (the first panel in Fig. 5.27).

3.3.4. Time evolution

As shown in subsection 3.2.5, we can analyze the time evolution of the numerically generated pattern, taking in account the existence of the characteristic time t_c that separates linear and nonlinear regimes.

For a simulation time much smaller than t_c we observe some periodical surface modifications (Fig. 3.10 (a)), but the pattern has not completely developed yet. By increasing the time up to $t_c/2$ a refined surface pattern consisting of well expressed parallel lines with numerous bifurcations is observed (Fig. 3.10 (b), cf. also Fig. 3.8). At and beyond crossover time t_c, as illustrated in Fig. 3.10 (c), we notice a coarsening of the ripples. The effect was also observed experimentally (cf. Fig. 5.20 (b), (e)). Whereas Fig. 3.10 (a-c) exhibit a progressive development of surface patterns, for times considerably above t_c (Fig. 3.10 (d)), structures start to collapse (similar to Fig. 5.20 (c), (f)), and kinetic roughening takes place, known from nonlinear dynamics. Though in the model the situation is simplified and we did not investigate the pulse-to-pulse development of ripples, the numerical results show that a progressive evolution of structures occurs only in an appropriate time interval.

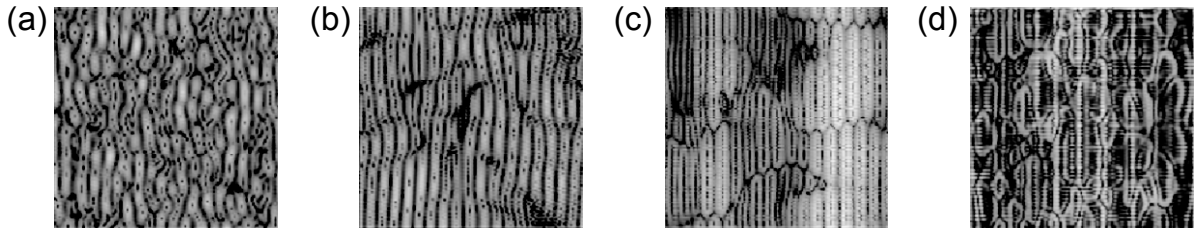

Fig. 3.10: Time evolution of numerically calculated surfaces ($64\pi \times 64\pi$) for $\Pi=1$ and $\phi=0$: (a) $t << t_c$; (b) $t = t_c/2$; (c) $t = t_c$; (d) $t = 2t_c$. (t_c=1600 a.u.).

3.4. Conclusion

The model for self-organized surface pattern formation upon femtosecond laser ablation was developed by introducing a dependence on laser polarization. Sigmund's stochastical theory of sputtering and the model of ion-induced surface pattern formation were adopted to develop of a model for the laser-induced polarization-dependent nanostructures. In this approach the laser electric field causes an asymmetry of the initial electron kinetic energy distribution and the related variation in excitation transfer probability. Polarization breaks the symmetry in electron energy transfer and aligns the surface patterns, corresponding to the main direction of the energy flow.

Here it is necessary to note that our explanation of anisotropic excitation upon femtosecond laser irradiation is linked to asymmetric electron energy transfer as one possible scenario. The microscopic nature of this phenomenon can be more complex and can include other processes that break symmetry in the energy transfer and result in a similar effect.

4. Instrumentation

Ablation experiments were carried out on different target materials under ultra-high vacuum (UHV) conditions using a Ti:Sapphire chirpedpulseamplified (CPA) laser system, delivering ≈100 fs pulses at a central wavelength about of 800 nm.

To structure dielectric targets, freshly cleaved single crystals of CaF_2(111), BaF_2(111), NaCl(111), polished samples of MgF_2, Al_2O_3 and SiO_2 were exposed to multiple irradiation at an intensity well below the single-shot ablation threshold. A sufficient number of pulses also was applied to produce LIPSS on semiconductors (commercial p- and n-doped Si(100) wafers) and metals (molybdenum and tungsten foils), but in this case the applied intensity was kept about the ablation threshold for a single pulse.

After ablation the crater topography was inspected ex-situ by surface sensitive microscopy techniques, such as Optical Microscopy (OM), Scanning Electron Microscopy (SEM) and Atomic Force Microscopy (AFM). Electrical properties of laser modified surfaces were examined by Electrostatic Force Microscopy (EFM) and by Scanning Kelvin Microscopy (SKM). To gain information about the in-depth modifications, conventional and high-resolution transmission electron microscopy (TEM and HR-TEM) was carried out on the ablated samples; collaboration with the Martin-Luther-University Interdisziplinäres Zentrum für Materialwissenschaften, Halle (Germany). Further, Raman and photoluminescence (PL) spectra have revealed additional details concerning bulk structural modifications.

4.1. Laser system

As mentioned above, all ablation experiments presented in this work were performed by using a commercial system of mode-locked Ti:Sapphire laser (Ti^{+3}:Al_2O_3) with regenerative amplification. The principal scheme with parameters characterizing the laser irradiation that was used is shown in Fig. 4.1.

The main part of the system consists of a mode-locked Ti:Sapphire oscillator (Tsunami 3960, Spectra Physics) pumped by a cw Nd:YVO_4 laser (Millenia V, Spectra Physics). The oscillator runs at a repetition rate of about 80 MHz and produces Gaussian pulses with standard output wavelengths from 720 nm to 850 nm; the pump laser pulse width ($\Delta\tau_p$) is about 80 fs.

The femtosecond pulses of only a few nanojoules energy are transferred into a Ti:Sapphire regenerative amplifier (Spitfire, Spectra Physics), where the energy can be increased to over 1 mJ (amplification greater than 10^6). The CPA procedure includes

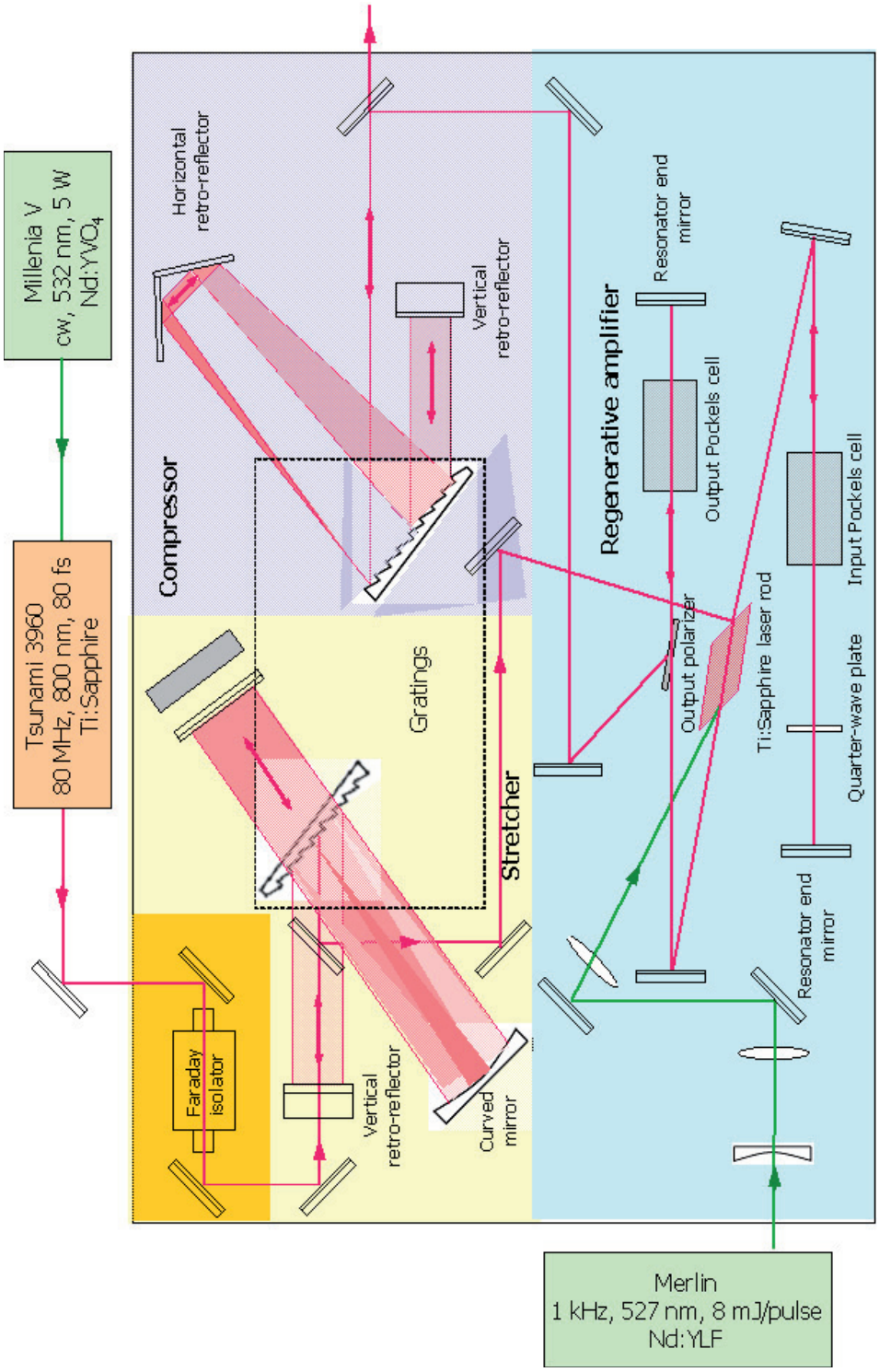

Fig. 4.1: Commercial system of mode-locked Ti:Sapphire laser with regenerative amplification. Merlin and Millenia are pump lasers; Tsunami is an fs-oscillator; a Spitfire Ti:Sapphire fs- amplifier consists of the following main parts: at the entrance there is a system of optical diodes (dark-yellow); after that you see a stretcher (light-yellow), regenerative amplifier (blue) and, finally, a compressor (violet) [Man95].

temporally stretching the input femtosecond pulse, using a single grating ("Stretcher" area in Fig. 4.1) with the subsequent amplification in the multi-pass Ti:Sapphire resonator ("Regenerative amplifier" area in Fig. 4.1), which is optically pumped by a frequency-doubled Nd:YLF laser (Merlin, Spectra Physics). Finally, after recompression in the single grating compressor ("Compressor" area in Fig. 4.1), at the exit of the system we have pulses of 0.75 mJ energy at 1 kHz and of ≈100 fs duration at full width at half maximum (FWHM). The output beam with a diameter of about 5 mm is linear (horizontal) polarized, it has a Gaussian spatial intensity profile and energy pulse-to-pulse stability < 3%.

The pulse width is measured by a Single-Shot Autocorrelator (SSA) Model 409, Spectra Physics. A Gaussian pulse shape with a deconvolution factor of 0.65 is used to determine the pulse width from the width of an autocorrelation trace given by the SSA. A spectrometer has been used to check the wavelength of the output beam.

4.2. Gaussian beam

The focused laser beam has an approximately Gaussian spatial intensity profile that was determined by a CCD camera (Spiricon) placed in the focal plane (Fig. 4.2 (a)).

The electric field variation of a Gaussian beam is given by:

$$E = E_0 \exp\left(-\frac{r^2}{w^2}\right), \tag{4.1}$$

where w is the beam waist across the beam propagation direction, r is the distance from the beam center. The intensity profile of the beam is also expressed by Gauss function:

$$I(r) = I_0 \exp\left(-\frac{2r^2}{w^2}\right), \tag{4.2}$$

where I_0 is the peak intensity that is defined as:

$$I_0 = \frac{P}{\pi w^2} \tag{4.3}$$

where P is the laser pulse power. The fundamental equations [MaW95] describing the Gaussian beam radius $w(z)$ and the wavefront radius of curvature $R(z)$ are:

$$w^2(z) = w_0{}^2\left[1+\left(\frac{\lambda z}{\pi w_0^2}\right)^2\right] \text{ and } R(z) = z\left[1+\left(\frac{\pi w_0^2}{\lambda z}\right)^2\right] \tag{4.4}$$

with w_0 the beam radius at $z = 0$ (i.e. the laser output pupil) and λ the laser wavelength; z describes the coordinates along the propagation direction. The characteristic parameter in both equations is known as the Rayleigh range z_r:

$$z_r = \frac{\pi w_0^2}{\lambda}. \tag{4.5}$$

It is also referred to as the depth of focus when focusing a Gaussian beam, or as the confocal parameter $b = 2z_r$ (see Fig. 4.2 (b)), i.e. the size of the interval *(-z_r, z_r)*. In fact, the wavefront radius of curvature R has its minimum value at $z \leq |z_r|$.

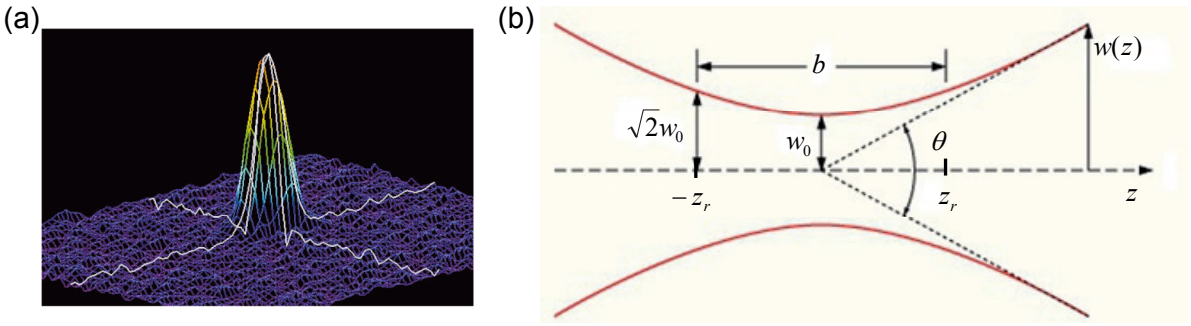

Fig. 4.2: (a) Intensity profile of a focused laser beam (800 nm) recorded by a CCD camera; (b) Gaussian beam parameters associated with angular divergence.

For the interval $0 \leq z \leq z_r$, the beam waist varies between $w_0 \leq w \leq \sqrt{2}w_0$. The half divergence angle of the beam for $z >> z_r$, i.e. far from the focal point, as it follows from the first Eq. (4.4), is given by

$$\theta \approx w/z \approx \lambda/(\pi w_0) \tag{4.6}$$

Eq. (4.6) characterizes the diffraction limited divergence of the laser beam. In the same way, for lenses with a focal distance f much more than a Rayleigh range z_r ($f >> z_r$), we can derive a beam waist at focal point w_0 from the known beam radius $w(z)$ and the focal length of a lens:

$$w_0 = f\lambda/\pi w\,. \tag{4.7}$$

In our case, a laser beam (800 nm) with a diameter of about 5 mm is focused by a convergent lens of +300 mm focal length to a spot with a diameter of about 100 μm with a confocal parameter $2z_r \approx 7$ mm.

4.3. Experimental setup

The principal scheme of general experimental setup is shown in Fig. 4.3. The beam is focused by a 300-mm focal length lens onto the front side of the target, which is placed in an ultra-high vacuum (UHV) chamber ($\approx 10^{-9}$ mbar).

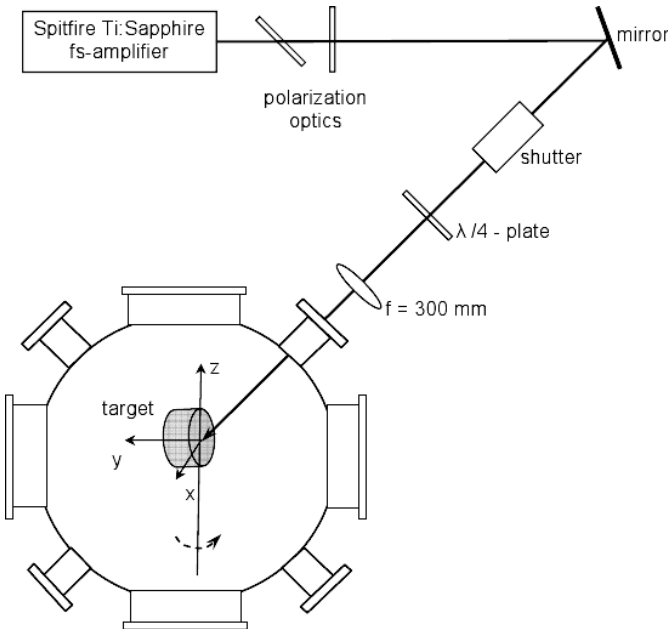

Fig. 4.3: Principal scheme of general experimental setup. The laser pulse is focused onto the front side of the target, which is placed in a UHV chamber. The target can be translated in x, y and z directions and rotated around the z-axis to vary the laser beam incident angle.

The irradiated target can be translated with micrometer precision in x-,y- and z-direction, and the incident angle of the laser beam is varied from 0° up to 45° by rotation of the target about the z-axis.

The laser energy is continuously adjustable with polarization optics. An electromechanical shutter is employed to precisely control the number of pulses and the time interval between successive pulses. Different states of polarization (linear, circular or elliptical) and a rotation of the plane of polarization are obtained by using a λ/4- and a λ/2-plates.

4.4. Sample analysis

The laser-modified surface morphology was inspected by using an Atomic Force Microscope (AFM) NT-MDT Solver P47H, and a Scanning Electron Microscope Zeiss EVO 40. To gain more information about the modification of the crystal lattice, the formation of new phases and the generation of extended defects inside of the sample upon laser ablation, Raman spectroscopy, and Photoluminescence spectroscopy were applied as well as Transmission Electron Microscopy. More details about these techniques will be elucidated in Ch. 6.

4.4.1. Atomic Force Microscope Solver P47H

Atomic Force Microscopy (AFM) was applied to investigate the morphology and the local properties of solid surfaces with high spatial resolution. The working principle of AFM is based on the measurement of interaction forces between a sharp tip at the end of an elastic cantilever and the sample surface [Mir04]. As the probe is moved across the surface, the bending of the cantilever (Δz) due to the tip-sample interaction reflects the topography, as shown in Fig. 4.4 (a).

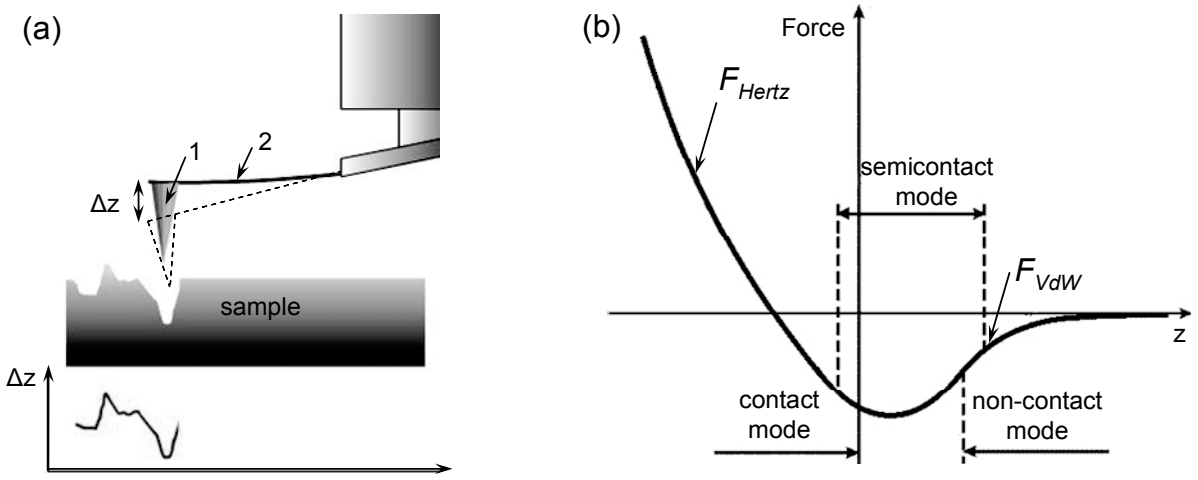

Fig. 4.4: (a) Schematic diagram showing the principle of operation of the AFM: (1)–probe tip; (2)–cantilever; Δz – is the tip displacement corresponding to the bending produced by the interaction with the surface; (b) Probe-surface interaction force (after [Mir04]).

4.4.1.1. Typical forces

The cantilever can be bent not only by the direct tip-surface interaction, but also by far-ranging forces such as Van der Waals, electrostatic, magnetic, etc. For this work, only the most important forces will be considered. The resulting interaction force as a function of the tip-surface separation is presented in Fig. 4.4 (b).

At tip-sample separations of the order of several tens of angstroms, the major contribution is the Van der Waals (VdW) force. In a dipole-dipole approximation, this intermolecular attracting force is related to the tip-surface distance z as $F_{VdW} \sim 1/z^6$. For macroscopic tip and sample geometries, for instance a spherical tip above the half-space, the distance dependence of the force on the distance is lower. A typical approximation is $F_{VdW} \sim 1/z^2$.

When the cantilever tip contacts the surface, repulsive forces due to elastic deformations in the contact zone, so-called Hertz forces, start to act. The Hertz problem solution [LaLd87] relates the force F_{Hertz}, acting on the cantilever tip, and the penetration depth ($-z$) by $F_{Hertz} \sim (-z)^{3/2}$.

Electrostatic interaction between the tip and the sample can appear rather often. These forces can be both attractive and repulsive. If we consider interaction of the conductive coated tip with a semiconducting sample, the tip-sample capacitive force can be written, according to [Mir04] as:

$$F_z = -\frac{1}{2} U^2 \frac{\partial C}{\partial z}, \tag{4.8}$$

where U is the voltage between tip and sample and C is the tip-sample capacitance. A constant dc voltage U_0 and a variable ac voltage $U_\omega \sin(\omega t)$ can be applied between the tip and the sample, and, taking into account a potential distribution $\phi(x,y)$ on the surface, we can find the resulting effective tip-surface voltage U:

$$U = U_0 - \phi(x,y) + U_\omega \sin(\omega t). \tag{4.9}$$

Using the trigonometric relation $\sin^2(\omega t) = (1 - \cos(2\omega t))/2$, we obtain from Eqs. (4.8) and (4.9) that F_z is a sum of a constant component (a), a component at frequency ω (b) and a component at 2ω (c):

$$\begin{aligned}
F_{z,\omega=0} &= -\frac{1}{2}\frac{\partial C}{\partial z}\left[(U_0 - \phi(x,y))^2 + U_\omega^2\right] \quad (a) \\
F_{z,\omega} &= -\frac{\partial C}{\partial z}\left[(U_0 - \phi(x,y))U_\omega \sin(\omega t)\right] \quad (b) \\
F_{z,2\omega} &= \frac{1}{4}\frac{\partial C}{\partial z}\left[U_\omega^2 \cos(2\omega t)\right] \quad (c)
\end{aligned} \tag{4.10}$$

A registration of the constant component of the tip-sample capacitive force (Eq. (4.10) (a)) reveals information about the amplitude variation of the electrostatic force acting on the tip. The component at the frequency ω (Eq. (4.10) (b)) characterizes the contact potential difference between tip and surface. A detection of the cantilever oscillation amplitude at frequency 2ω (Eq. (4.10) (c)) allows to map the derivative of the capacity with respect to the z-coordinate [Rat11].

4.4.1.2. Modes of operation

Depending on the type of excitation−mechanical or electrical−of the cantilever, and the tip-sample distance, several modes of operation can be carried out. Only the techniques that were applied for sample analysis in the dissertation are discussed below.

In contact mode the tip touches the sample. Van der Waals attraction forces, and capillary, electrostatic and repulsion elastic forces are acting between the tip and the surface and compensate each other in equilibrium. By scanning, the surface topography is recorded by registration of the cantilever deflection due to the action of repulsive forces.

In semi-contact, or tapping, AFM mode, cantilever oscillations are mechanically excited with a frequency near to the resonant frequency ω_0 with oscillation amplitudes of about several tens of nanometers (~50 nm). During scanning, the oscillating cantilever tip touches the surface periodically. In this mode, the tip-surface interaction consists of Van der Waals forces and the short-range repulsive forces, which begin to act during the tip-surface contact. Thus, the oscillation amplitude is a direct measure of the tip-sample separation, allowing for a precise mapping of the sample surface. In addition, the monitoring of the oscillation phase provides the opportunity to estimate local elastic properties [Mir04].

Similar to the previous technique, in non-contact mode the cantilever is also mechanically excited close to the resonance frequency, but it oscillates at low amplitude. The vibrating cantilever probes the surface in the region of long-range forces and the local force gradients induce a shift in the resonance frequency and thus in its oscillation amplitude and phase [MWW87].

Non-contact mode is applied in Electrical Force Microscopy (EFM) to register the long-range capacitive forces (Eq. (4.8)). EFM is used to register the amplitude variation of the electrostatic force acting on the tip. The measurements were carried out in an amplitude mode [RRV06]. The scanning is performed in the standard double-pass technique [Mir04]. During the first pass the topography image is recorded in semicontact mode as it was described above. In the second pass the cantilever is

excited by the applied ac voltage $U_\omega \sin(\omega t)$ and the EFM phase contrast, measuring the force on the tip, is recorded [Rat11].

Electrical excitation of the cantilever is implemented in Scanning Kelvin Microscopy (SKM) that allowed measuring the contact potential difference ϕ_{CP} between tip and surface [NOW91]. This method is based also on the double-pass technique like EFM, but at the second scan a feedback system of the microscope regulates dc voltage U_0 until the electric force component at frequency ω (Eq (4.10) (b)) vanishes. This is possible when U_0 is equal to the local contact potential between tip and sample:

$$U_0 = \phi_{CP} = \phi_T - \phi_S , \qquad (4.11)$$

where ϕ_T and ϕ_S are work function of tip and sample. In this configuration, mapping U_0 reflects the distribution of the surface potential along the sample surface.

4.4.2. Scanning Electron Microscope (Zeiss EVO 40)

The Scanning Electron Microscope (SEM) permits the characterization of surface topography modifications of a wide range of materials on a nanometer scale. For the AFM measurement the depth of structures is a critical parameter which limits the investigation; for the SEM this restriction disappears. That is a big advantage in our case and considerably simplifies the analyses of samples.

Generally, samples investigated by SEM should be of appropriate size, stable in the vacuum and electrically conductive. Metallic and semiconducting samples studied in this work satisfy these conditions without any preparation. To investigate nonmetallic materials and to obtain high-resolution images we should cover the samples with a very thin layer of metal. There are two usual methods for coating nonmetallic samples with a conducting layer: sputter coating and vacuum deposition.

The sputter coater is the preferred coating instrument because this method is relatively easy, quick and inexpensive. The sputter coating is done under partial vacuum. Molecules of argon gas (Ar) are ionized in the high voltage field between the cathode and the anode. The Ar^+-ions are accelerated to the cathode that is made of the coating metal. The ions sputter the cathode target and the negatively charged metal atoms accelerate to the anode upon which the sample has been placed. The greatest disadvantage of sputtering is heat damage of the structured samples.

The other method of coating is evaporation of a metal in a vacuum. The process is performed in a vacuum chamber. An appropriate amount of a metal is placed on a tungsten wire. The tungsten wire filament is heated to the vaporization point of the

coating metal that condenses on the sample. In this case we can avoid the heat damage of the structured sample.

In the SEM, the area to be analyzed is irradiated with a focused electron beam. The types of signals produced from the interaction of the electron beam with the sample include secondary electrons, backscattered electrons, characteristic x-rays, and other photons of various energies [GNJ08]. In our case the image of the structured surface is created by the registration of secondary and backscattering electrons because these vary primarily as a result of differences in surface topography.

5. Control parameters in pattern formation process

Laser ablation of various target materials has revealed a great diversity of self-organized nanostructures in the irradiated area, with feature size (respectively, periods) depending on the laser intensity and the number of pulses applied. A wide assortment of nanopatterns from homogeneous distributed nano-spheres to highly periodic linear arrangement can be observed at the bottom of the ablated crater. Experiments with linear, circular, and elliptical polarized light indicate that the laser polarization determines the orientation and shape of the ripples, but surface defects can be even stronger as a control parameter for pattern orientation than polarization. In this chapter we discuss the role of these parameters by producing controllable self-organized surface nanopatterns by femtosecond laser ablation.

5.1. Laser polarization as control parameter

Multi-pulse laser ablation experiments on dielectric targets with linearly polarized light have revealed the strong coupling between orientation of LIPSS and laser beam polarization: the fine sub-wavelength ripples are always perpendicular to the incident laser electric field.

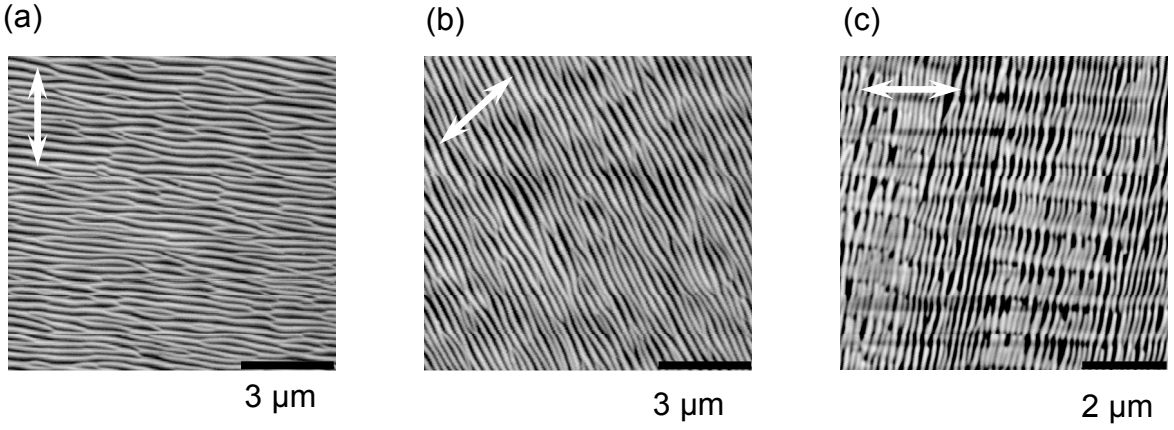

Fig. 5.1: Influence of rotation of laser electric field (double arrows) on the ripples orientation. SEM micrographs of fragments from ablation spots produced on CaF_2 by using of linear polarization at 8.3 TW/cm^2: (a, b) 5,000 pulses; (c) 300,000 pulses.

Moreover, a rotation of the laser beam polarization induces a corresponding rotation of the generated surface structures, as shown in Fig. 5.1 (b). Additionally, with an increase in the irradiation dose (i.e. 3×10^5 pulses in Fig. 5.1 (c)), the fine ripples can be overlapped by secondary structures of substantially bigger wavelength and aligned parallel to the beam polarization. All these features have been reported since the late

1990s [HVW99], [RCH02], [CHR03] and they were regularly observed by the present author as well.

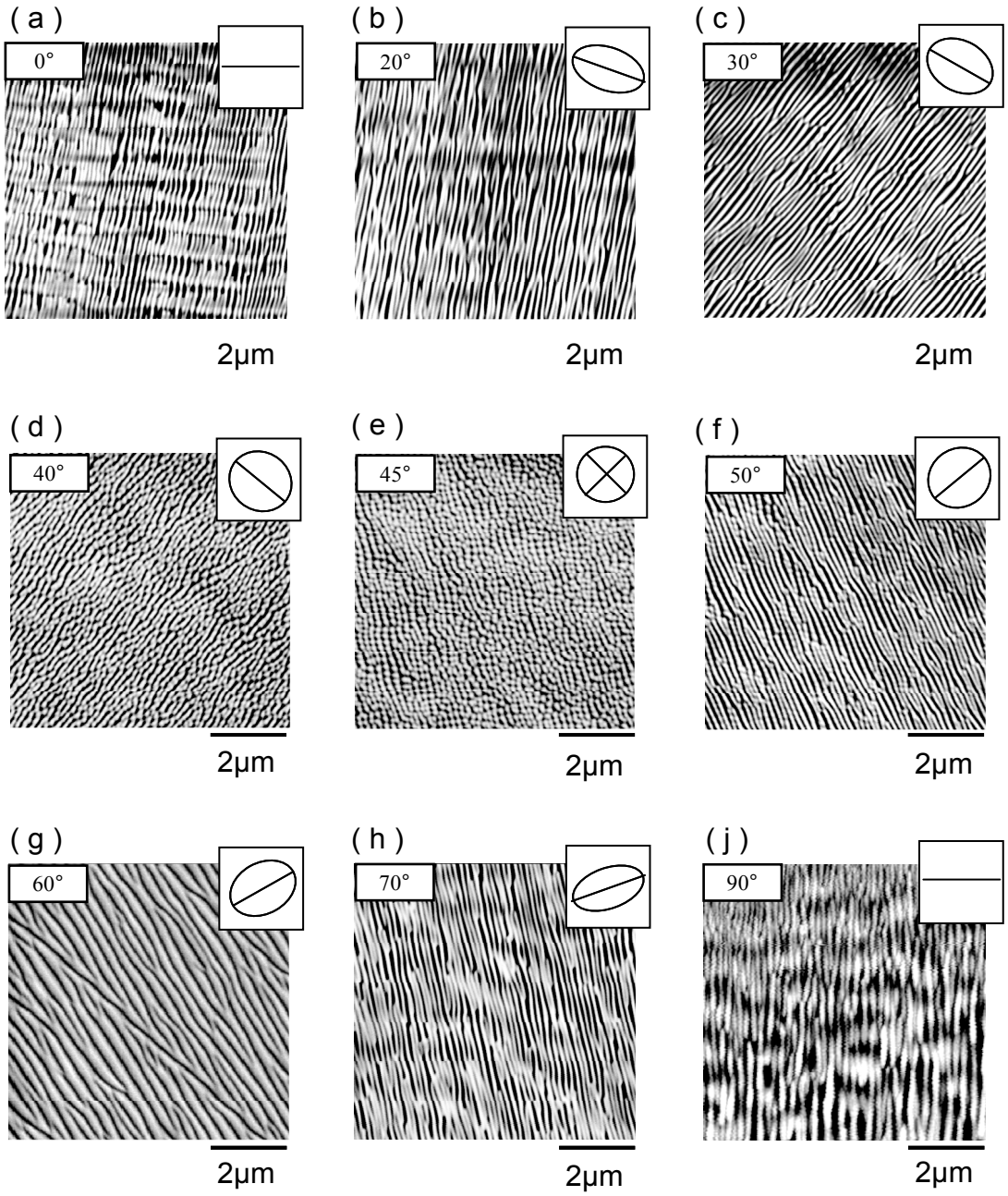

Fig. 5.2: SEM images of ripples, produced with elliptical polarized laser beam on the surface of CaF_2. The rotation angle of the quarter wave plate is indicated in each upper left corner. The calculated polarization ellipse is presented in each upper right corner. All patterns except (g) und (j) were produced by accumulation of 300,000 pulses of intensity 1.8 TW/cm². Spots on (g) and (j) were generated by 5,000 pulses of 8.3 TW/cm² (Note the significantly larger ripples wavelength).

5.1.1. Ripples induced by elliptically polarized laser beam

The influence of laser polarization was studied in detail in a series of experiments using elliptically polarized light with variable ellipticity.

Some details from a central part of ablation spots produced on CaF_2 are shown in Fig. 5.2. The degree of elliptical polarization is determined by the rotation angle of the quarter wave plate, which is designated in the upper left corner of SEM micrographs (Fig. 5.2). The rotation angle of the quarter wave plate was changed step by step from 0° to 180°. In Fig. 5.2 is shown only the first half of the rotation interval (0°-90°), the second half being a mirror image of the first one. Polarization ellipses according to the rotation angle of the quarter wave plate are calculated through the sum of two components of the incidence electromagnetic wave:

$$E = e_x E_x \cos(\omega t) + e_y E_y \cos(\omega t + 2\varphi) \tag{5.1}$$

and they are depicted in the upper right corner of the SEM micrographs.

Referring to Fig. 5.2, the orientation of the ripples strongly depends on the direction of the major axis of the polarization ellipse. On all pictures the orientation of the ripples is perpendicular to the major axis. Micrograph (e) reveals a homogeneously distributed pattern produced with circularly polarized light. In the case of circular polarization, both components in electromagnetic wave are equal in magnitude and no dominant direction of polarization is observed.

Detailed analysis of ablation patterns presented in Fig. 5.2 demonstrates also another significant dependence of ripple morphology on the degree of polarization. From Fig. 5.2 (a)-(e) and (j)-(e) it follows that the ripple length (distance between bifurcations) is strongly related to the ratio between the long axis and the short axis of the polarization ellipse. This observation cannot be explained in the framework of the conventional ripple theory [DSY82], [SYP83]. Instead it gives strong support to the model of self-organized structure resulting formation from instability [RCB06], [RHW00]

5.1.1.1. Pattern induced upon circularly polarized irradiation

When two components of the incident electric field (Eq. (5.1)) have exactly the same amplitude and 90° of phase difference, this is the special case of elliptic polarization, namely, circularly polarized irradiation (Fig. 5.2 (e)).

Summarizing numerous experimental results, we can conclude that for circularly polarized light the representative pattern is characterized by a lack of the linear order typical for elliptical or linear polarization independent of material. An excellent example is presented in Fig. 5.3. The pattern consists of uniformly distributed nanoparticles. A cross section analysis of the generated AFM images has revealed that the nanoparticles have almost spherical form with an average diameter about of ~100

nm. A Fourier transform analysis of the AFM images (inserts in Fig. 5.3) confirms the homogeneity of the pattern.

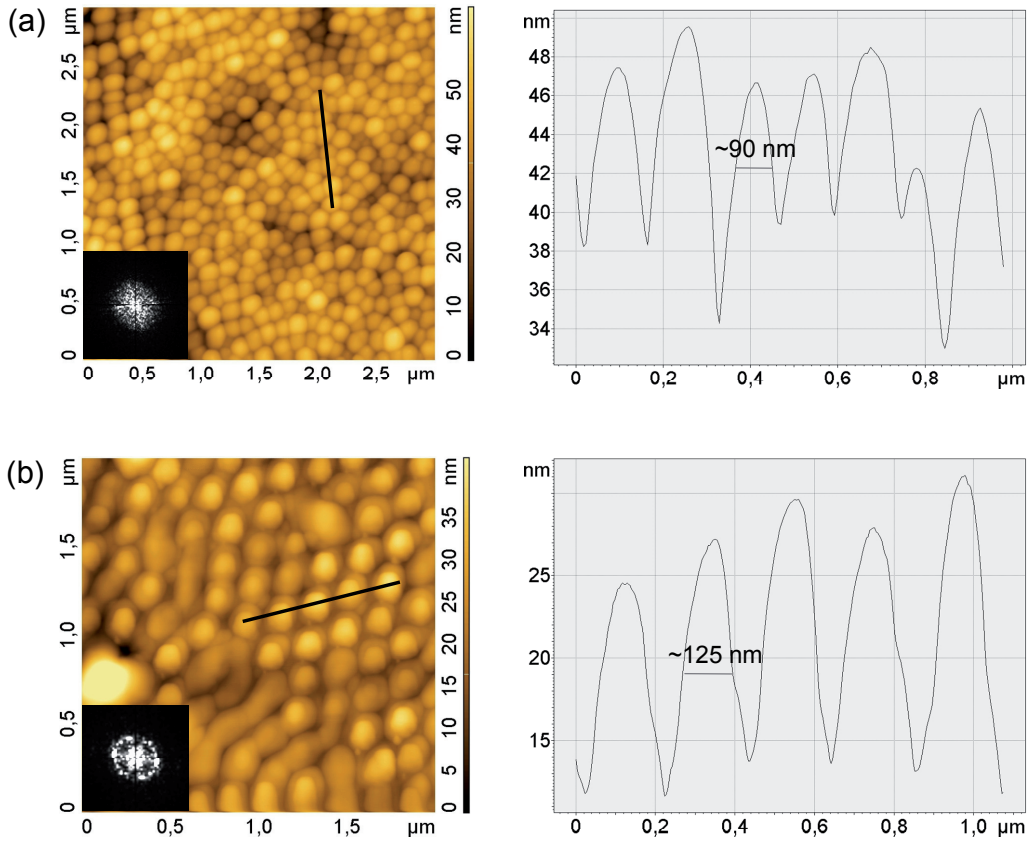

Fig. 5.3: AFM micrographs and Fast-Fourier transforms (FFTs) (inserts in the lower left corners) from details of the structured area produced with circularly polarized light on (a) CaF_2 (5,000 pulses@7.9 TW/cm²) and (b) Si (1,000 pulses@1.0 TW/cm²); the corresponding depth profiles of the lines indicated in the topography panels give the ripple's spatial features.

An extensive study of ablation patterning on various target materials upon circularly polarized irradiation has shown that the nanostructures can be successfully developed only by applying a sufficient number of pulses at low intensity. The surface morphologies exhibit features similar to those observed with the use of linear polarized light, namely: the size of the structures depends on the irradiation dose and on the local intensity of the laser pulse, but coupling between the laser polarization and the orientation of nanostructures is lacking (Fig. 5.2 (e), Fig. 5.3).

Further, the formation process of the homogeneously distributed pattern is very sensitive to the laser electric field and to the quality of the surface target. Appearance of any artificial ellipticity in the incidence laser field, for instance, due to multiple reflections or a deviation from a normal incidence, leads to a corresponding alignment of the pattern, as shown in Fig. 5.4. Here, long ordered chains of spherical

nanoparticles of a diameter of about 100 nm are formed. The basic arrangement of nanospheres is covered with an additional, coarser overstructure. A Fast-Fourier transform of the topography image indicates the high regularity of this complex nanopattern.

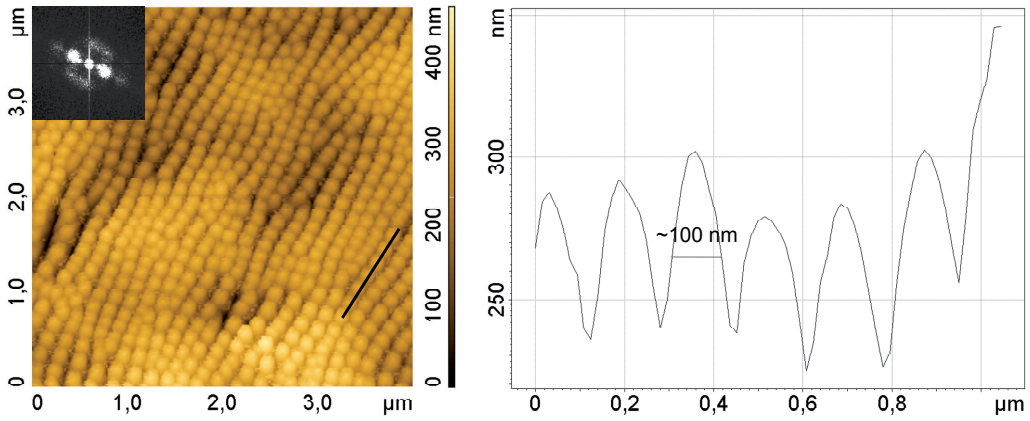

Fig. 5.4: AFM images with FFT (insert in the upper left corner) of surface patterns from a crater center produced on CaF_2 with 300,000 pulses of circular polarization at intensity of 2.0 TW/cm². Depth profile of the line indicated in the topography panel reveals the following pattern features: modulation depth is in the range 50÷80 nm, distance between two peaks (period) is about of 150 nm and dot diameter ≈100 nm.

Another reason for the linear order in patterns induced with circularly polarized light may be extended surface microdefects. Scratches or cleavage steps tend to override the influence of polarization and lead to infringement of the homogeneous distribution of the nano-spheres, as can be seen on the left side of the CaF_2 microphoto in Fig. 5.3 (nanoparticles are aligned along the surface defect) and in Fig. 5.13 (b, c).

5.1.1.2. Rotation sense of circular polarization

Ripple morphologies generated on CaF_2 with *left* and *right* circularly polarized light are presented in panels (a) and (b) of Fig. 5.5, correspondingly. The nanopatterns consist of short segments/nanoparticles with a diameter about of 100÷150 nm, arranged in well-defined long parallel lines with periods in the range 200÷300 nm, with many intersections and bifurcations. The linear ordering in the pattern indicates an artificial ellipticity of the laser electric field, which can be caused, for instance, even by the slightest deviation of the laser beam from the normal incidence. Despite the different sense of polarization (*left/right*), the orientation of the long periodic arrays is the same in (a) and (b) (Fig. 5.5).

Summarizing all ablation results obtained with *left* and *right* circularly polarized irradiation, we can conclude that the orientation and shape of the surface structures is

not influenced by the rotation sense (*left/right*) of the laser electric field vector. Therefore, the circularly polarized laser irradiation is considered further without paying any attention to the rotation sense.

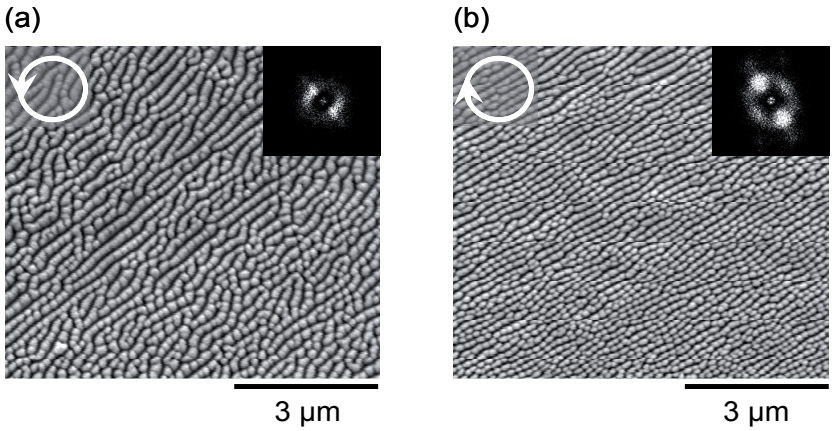

Fig. 5.5: SEM micrographs with FFT (insert in the upper right corner) from a central region of ablation spots on a CaF_2 surface generated by applying of 5,000 pulses at intensity of 8.0 TW/cm² of (a) left and (b) right circularly polarized light. Rotation sense of the electric field vector is indicated in the upper left corner.

5.1.1.3. Angle of incidence

To study systematically the effect of a non-normal incidence of a circularly polarized beam, a series of experiments was performed on a CaF_2 target.

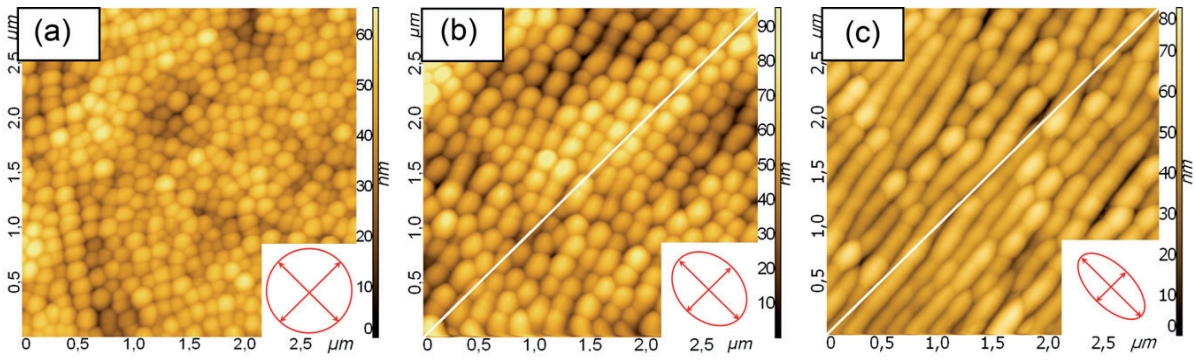

Fig. 5.6: Artificial ellipticity at the irradiated surface of CaF_2: incident circular polarization turns into "elliptical" (the projection of the electrical field is presented at the bottom right corners) by increasing of the angle of incidence from 0° (panel (a)) to 30° (panel (c)), the angle of incidence in panel (b) is 20°. The white lines indicate the plane of incidence. Irradiations condition: I = 7.9 TW/cm²; 5,000 pulses.

The angle of incidence of a laser beam was varied gradually from 0° up to 30° in 5° steps. As shown in Fig. 5.6, the shape of the surface structures and the feature size are

very sensitive to the changing of circular polarization. For normal incidence (Fig. 5.6 (a)), the typical nano-sphere pattern is well developed. At the slightest deviation of the laser beam from the normal incidence the character of the surface pattern is changing, it is becoming aligned. For an incidence of 20° (Fig. 5.6 (b)), the spherical nanoparticles are transformed into the oblong ones and oriented perpendicular to the long axis of the projection ellipse depicted at the bottom right corner at the second panel in the figure. For 30° incidence, long parallel ripples of the same orientation are produced and the pattern resembles the structure formation induced by elliptically polarized irradiation, as can be seen in Fig. 5.6 (c).

By changing the angle of incidence of a circularly polarized beam we introduce a corresponding asymmetry of the laser electrical field at the sample surface. In other words, we transform the circular irradiated spot geometry into an elliptical one (Fig. 5.7); the corresponding projections of laser electrical field are depicted in the inserts (at the bottom right corners) in Fig. 5.6. The spot diameter in the plane of incidence is decreased whereas the diameter perpendicular remains unmodified. Correspondingly, for circular polarization, the field is unaltered in the direction perpendicular to the plane of incidence whereas it is attenuated in all other directions. Additionally, a phase shift at the surface is introduced because on one side (in plane of incidence) of the spot the incident wave front arrives earlier than on the opposite side.

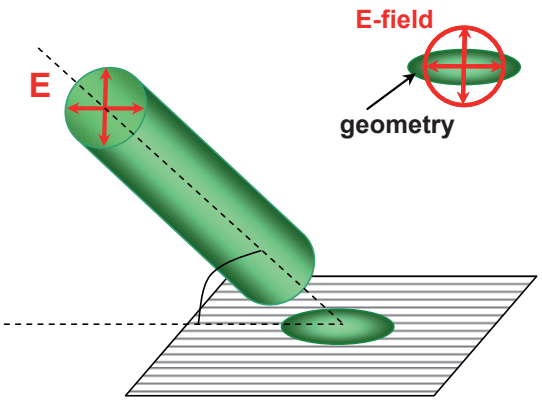

Fig. 5.7: Artifcially introduced ellipticity for originally circularly polarized laser field.

This clearly changes the polarization at the target surface by introducing an additional ellipticity. Thus we created the stronger component of the E-field (perpendicular to the plane of incidence) that dictates the orientation of the generated structures. The larger the angle of incidence, the stronger is the ellipticity introduced by this effect, as can be seen from Fig. 5.6.

5.1.1.4. Eccentricity

Let us introduce eccentricity, ε, as a relation between the long/major axis, a, (high field) and the short/minor axis, b, (weak field) of the laser electric field ellipse, namely, the *polarization ellipse*:

$$\varepsilon = \sqrt{\frac{a^2 - b^2}{a^2}}\,. \tag{5.2}$$

Experimentally the stepwise variation of ε is achieved by rotating the optical axis of the λ/4-plate with respect to the incident polarization. Then, the major axis of the polarization ellipse corresponding to the elliptically polarized laser field is rotated step by step by means of the λ/2-plate. The dependence of ripple direction on the ellipticity of the incident laser field has been systematically studied.

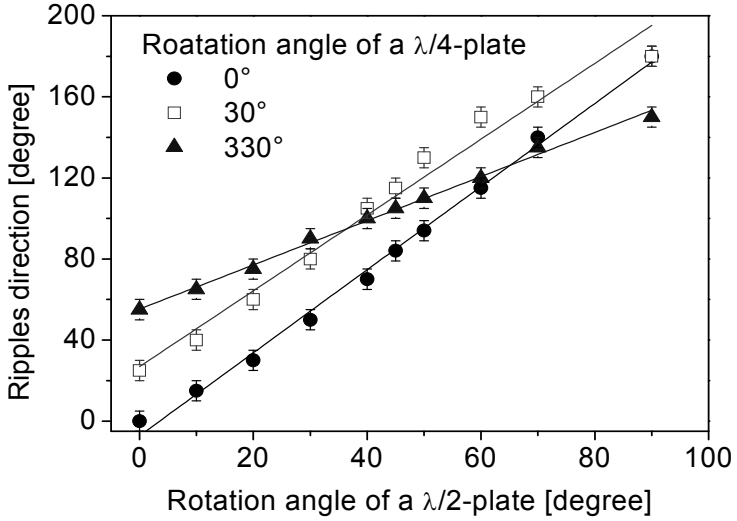

Fig. 5.8: Dependence of ripple direction on the direction of the major axis of the polarization ellipse.

First, we observe that the orientation of the ripples is directly proportional to the rotation angle of the λ/2-plate (Fig. 5.8) and, accordingly, ripples strictly follow the major axis, a, of the polarization ellipse, as has been already shown in the previous subsection. Further, the black and the red lines in the graph have an almost identical slope, which points to the same rate of ripple rotation for linearly (the λ/4-plate at 0°) and elliptically (the λ/4-plate at 30°) polarized light, respectively. Finally it can be noted that the red line is mirror-symmetric to the blue one that reflects the symmetry of the left-/right-elliptically polarized field; the corresponding position of the λ/4-plate was 30° and 330°.

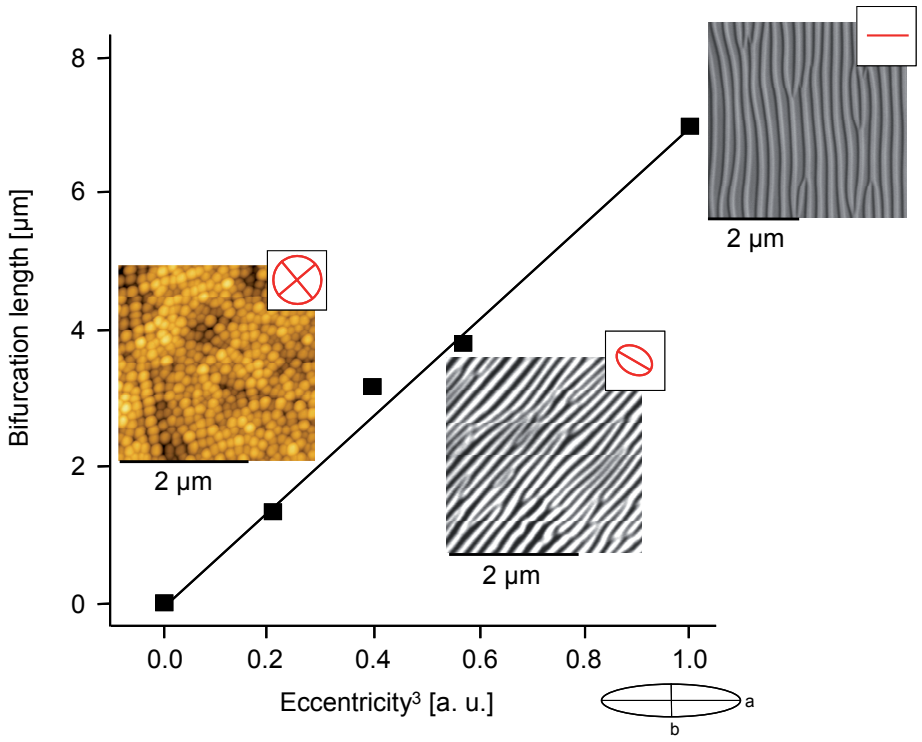

Fig. 5.9: Dependence of average bifurcation length on the ellipticity of the incident laser field. The ellipse with the long axis, *a,* and the short axis, *b,* is the polarization ellipse.

In addition to the orientation of the generated pattern, the typical structure length, i.e. the length of ripples between two bifurcations, was studied with varying ellipticity, ε. With increasing ε, the average bifurcation length increases significantly (Fig. 5.9) – from spherical, randomly arranged nanoparticles at circular polarization (ε=0) over ordered nano-sphere arrays at small ellipticity (the middle panel in Fig. 5.6), short linear strings at intermediate ellipticity (ε=0.5), to long almost parallel lines at linear polarization (ε=1).

5.1.1.5. Varying of the input polarization

The next set of experiments was performed to study the influence of the input polarization for elliptically polarized light on pattern characteristics.

To make clear the procedure of the experiment, the position of the wave plates in the general experimental setup is shown in Fig. 5.10. We vary the input polarization by rotating the optical axis of the λ/2-plate with respect to the incident polarization for elliptically polarized light. Ellipticity of the laser beam was changed by the position of the λ/4-plate at 30°, 45° and 60°.

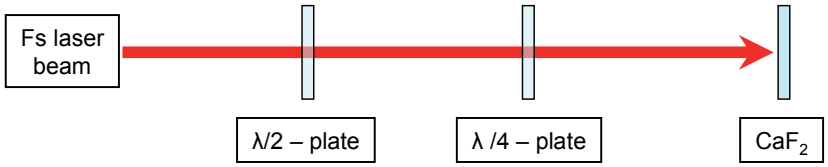

Fig. 5.10: Schematic of the experimental setup to study influence of the input polarization for elliptically polarized light.

As shown in Fig. 5.11, we can create an incident laser field of any modification depending on the points of interest (see calculated ellipses at the upper right corners). Form and orientation of the resultant polarization ellipse define the main features of the laser induced pattern. These results are summarized in Fig. 5.12, which displays the correlation between the direction of the input polarization and the ripple orientation for different polarization states determined by the rotation angle of the λ/4-plate.

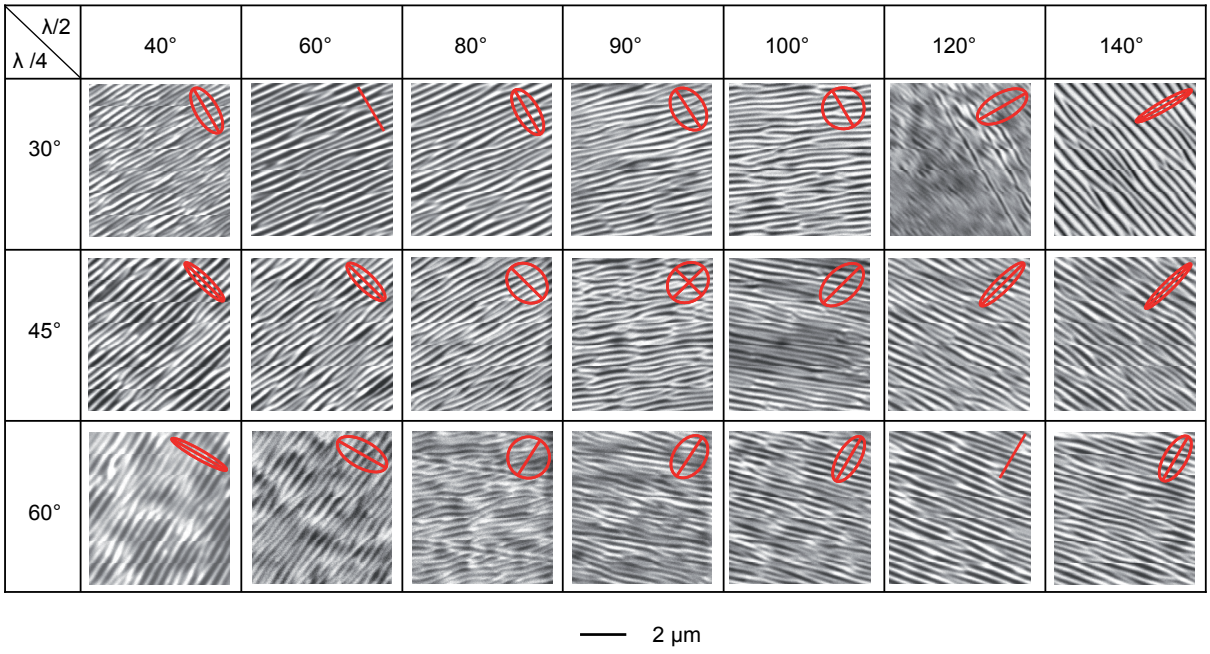

Fig. 5.11: SEM micrographs of nanopattern generated upon ablation (5,000 pulses, 8.2 TW/cm²) on a surface of CaF_2 show that ripple orientation follows the major axis of the polarization ellipse. At the upper right corners the calculated electric field is depicted.

One can see that all three curves have the same behavior: ripples do not change their orientations for the rotation angle of the λ/2-plate in the intervals [0°-60°] and [120°-180°], and, the direction of ripples in the first interval changes abruptly to become a mirror-reflected direction in the second interval. The interval where the orientation of ripples is rotated is relatively narrow and corresponds to the nearly circular polarization of the laser electric field. In this region, pattern is characterized by a short

bifurcation length in comparison to the "stable" regions (Fig. 5.11 (λ/4=60°, λ/2=80°) vs. (λ/4=60°, λ/2=40°) or (λ/4=60°, λ/2=140°)).

Controlling the incident laser field in this way, it is possible to generate a nanopattern with pre-defined features: it can be, for instance, almost parallel lines of any orientation in dependence on the direction of the incident electric field, or a web-like pattern, or ripples with particular desired bifurcation length. This method is very simple to implement and results can be reliably reproduced.

To summarize, it has been shown that not only the structure orientation but also the degree of order, indicated by the bifurcation length, is controlled by the laser polarization. This investigation has revealed complementary evidence on the important role that the direction of the laser electric field plays in self-organized structure formation upon femtosecond laser ablation, even though this takes place only a relatively long time after the laser pulse.

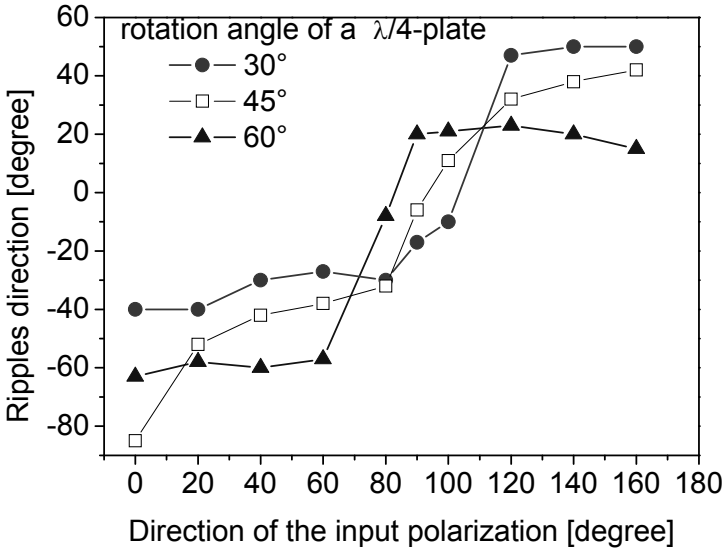

Fig. 5.12: Ripple direction plotted against the input polarization for a various positions of a λ/4-plate.

5.2. Surface defects

Cleavage steps and scratches on a surface of single crystals are an unavoidable effect of sample preparation. While such macroscopic defects on the investigated surface are unwanted, on the other hand, they have helped to manifest some very interesting features of self-organized structure formation.

It has been found that, initially, not only the parameters of the laser electric field can determine the structure orientation. The artificially induced scratch on a cleaved surface of CaF_2 in Fig. 5.13 (a) with width about of 1.0 μm aligns ripples independently of polarization; in this case the ripples are generated parallel to the

scratch. The next micrograph shows the development of the pattern on the same target by irradiation of the defect area with 120,000 pulses of circular polarization at very low intensity about of 1.9 TW/cm^2 (Fig. 5.13 (b)): the pattern is interrupted by the defect line and we observe ripples oriented perpendicular to it. On the last photo (Fig. 5.13 (c)) the typical nanopattern for circular polarization is produced on a cleaved surface of NaCl (111). It consists of homogeneously distributed nanospheres, but in the defect region the nanospheres are aligned by the defect line, similar to the case illustrated in Fig. 5.13 (a).

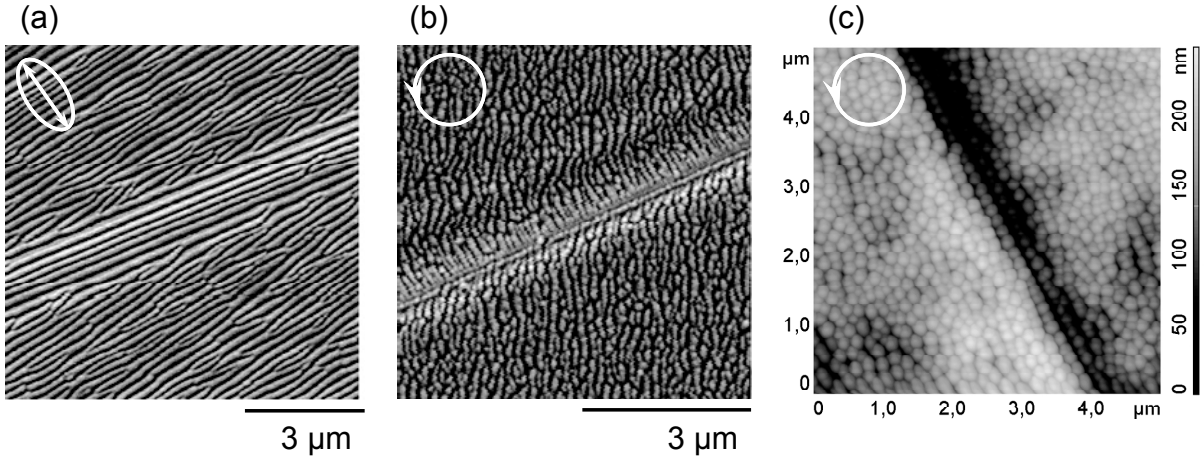

Fig. 5.13: Influence of extended surface defects (scratches, cleavage steps) on the orientation of nanostructures: (a) CaF_2 (111) target irradiated with 5,000 pulses of elliptically polarized light at laser intensity 8.3 TW/cm^2; (b) CaF_2 (111) target irradiated with 120,000 pulses of circularly polarized light at laser intensity 1.9 TW/cm^2; (c) NaCl (111) target irradiated with 5,000 pulses of circularly polarized light at intensity 7.9 TW/cm^2.

The influence of a surface roughness on the ripples orientation is illustrated in Fig. 5.14. A polished surface of MgF_2 was irradiated at laser intensity well below the single-shot ablation threshold of ≈20 TW/cm² [SJL07]. AFM scanning of the original non-irradiated surface of MgF_2 has revealed the presence of defect lines with depth about of 10÷20 nm, which can be seen also outside of the structured area in Fig. 5.14 (a). After irradiation with as few as 5 pulses of linear polarization, ordered arrays of nanospheres are observed, oriented parallel to surface scratches (Fig. 5.14 (b)). The same result, namely, ordering of the nanospheres along the defect lines, we have registered in the ablation spot produced under the same irradiation conditions with circularly polarized irradiation (Fig. 5.14 (c)). Comparison of (b) and (c) in Fig. 5.14 indicates that at an initial stage the direction of structures is defined only by surface defects. In this case the positive feedback, depending on the number of pulses, is too weak and the effect of laser polarization as an order parameter is not noticeable.

An accumulation of the pulse number up to 20,000 (Fig. 5.14 (d)) results in a formation of a nanopattern typical for a circularly polarized laser beam, that is, one with a feature size about of 200÷400 nanometers. Thus, an increasing irradiation dose (a number of pulses) increases the feedback and, then, results in favority the polarization effect on the self-organized pattern formation, as well as the pattern coarsening.

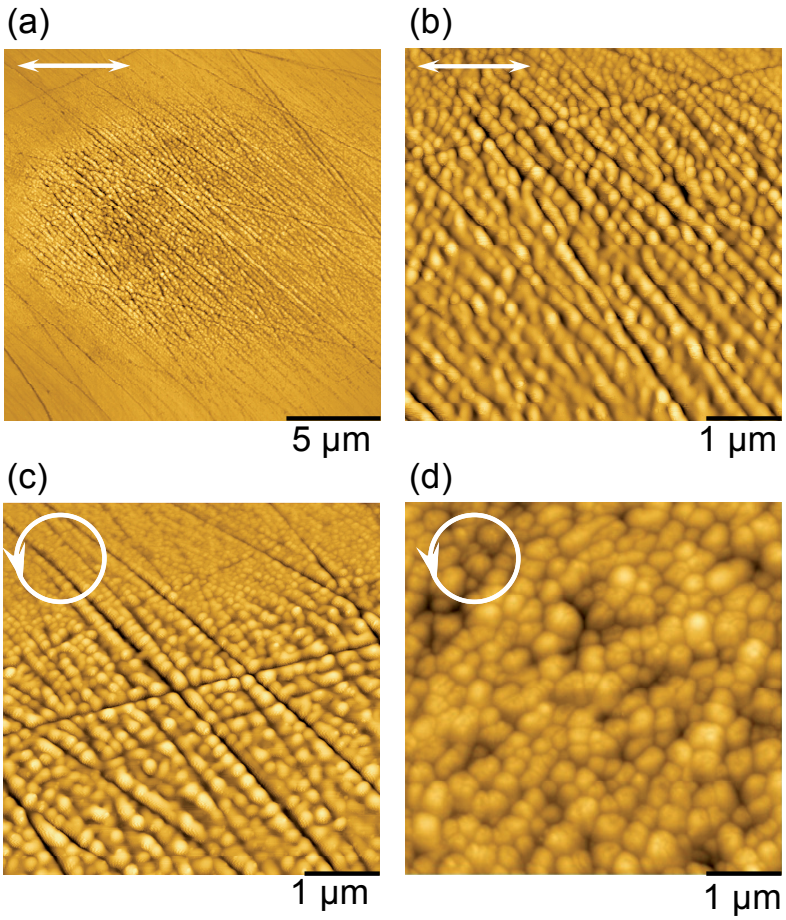

Fig. 5.14: Effect of a surface roughness on the pattern orientation: a polished surface of MgF_2 (111) was irradiated at laser intensity 7.2 TW/cm^2. (a) Overview of a typical ablation spot induced with 5 pulses of linear polarization. (b) Detail from the center of the spot shown in (a). (c) Detail from an ablation spot induced with 5 pulses of circularly polarized irradiation. (d) Detail from the center of ablated crater generated with 20,000 pulses; note the increased ripple size in (d).

Obviously, the extended macroscopic surface defects play an important role as an order parameter. Moreover, the influence of surface defects on structure orientation is significantly stronger than that of the polarization. Experiments have shown also a distinct role of positive feedback in the pattern formation process, and that a well developed surface morphology with typical polarization dependent characteristics can be observed only under irradiation with a considerable number of pulses.

5.3. Irradiation-dose dependence

One of the general peculiarities of self-organized structure formations is a strong dependence of the feature size on the deposited energy dose [CHR03]. The more energy applied to the system, the higher is the degree of disorder induced there. With energy dose, we regulate the degree of instability in the system and, correspondingly, the nanostructure size (cf. Eq. (3.30) and Ch. 3.2.5).

In our case the amount of applied energy to induce self-organized structures can be estimated in terms of an irradiation dose I_D, defined as a function of the product between laser intensity I and number of pulses N: $I_D \propto f(I \cdot N)$. The irradiation dose I_D can be changed by variation of one of the parameters, laser intensity I or number of pulses N.

5.3.1. Dependence on the local intensity of laser beam

A repetitive irradiation of silicon at laser intensities below the single-shot ablation threshold (1,000 pulses at 1.6 TW/cm²; at normal incidence) results in a typical ablation spot with a diameter of about of 110 µm.

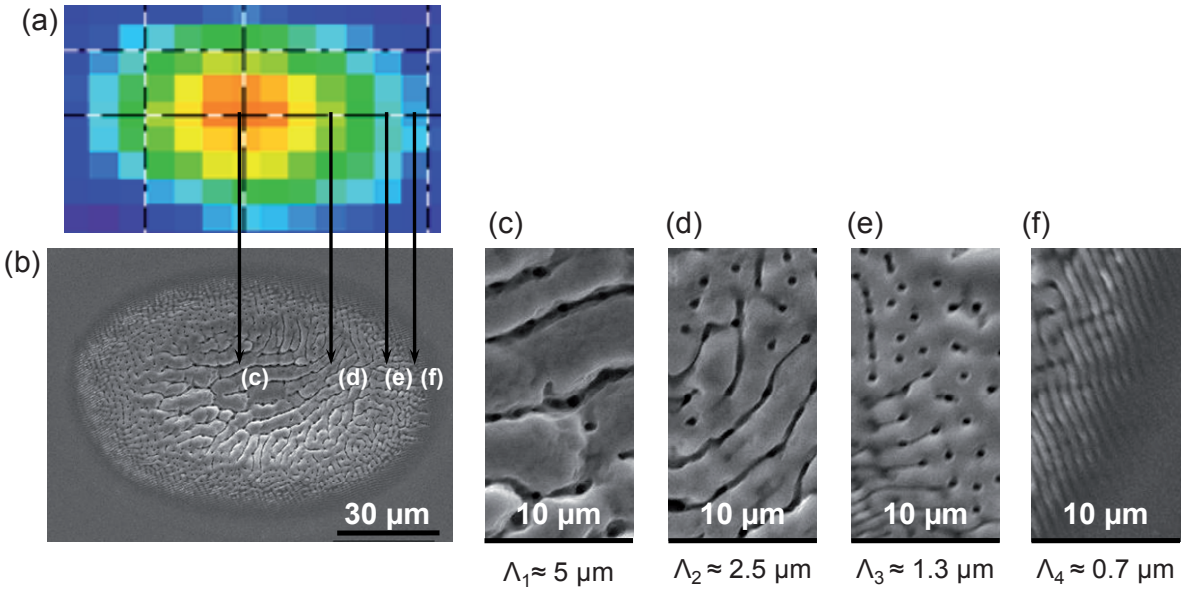

Fig. 5.15: (a) a laser spot of ~ 60 µm (FWHM) diameter with a Gaussian intensity profile is compared to (b) the ablation spot on Si (100) obtained after 1000 pulses at intensity 1.6 TW/cm²; details (c) – (f) present a variation in ONE spot of the feature size from the center (c) to the edge (f) dependent upon near Gaussian the local intensity distribution of the laser beam.

The focused laser beam delivered by the laser system has nearly a Gaussian spatial intensity profile (Fig. 5.15 (a)). The Gaussian intensity distribution results in a significant variation of deposited energy across the irradiation spot cross-section that

causes considerable variations in the nanostructures feature size within it (Fig. 5.15 (b)). It is valid for all non-metallic samples: at the middle of ablated area the size of the structure is larger in comparison with the edge region.

Moreover, the feature size does not smoothly follow the beam profile. It changes gradually at certain threshold intensities exhibiting a period doubling (Fig. 5.15 (c-f)) [RCV09] that is typical for self-organized structures originating from instability.

5.3.2. Single and multipulse irradiation

We can vary irradiation dose by keeping laser intensity constant and changing only the number of applied laser pulses. As discussed above, the self-organized nanopattern, normally, will be well developed only upon the action of a considerable number of pulses, but the initial surface modifications are detected already after the first pulse.

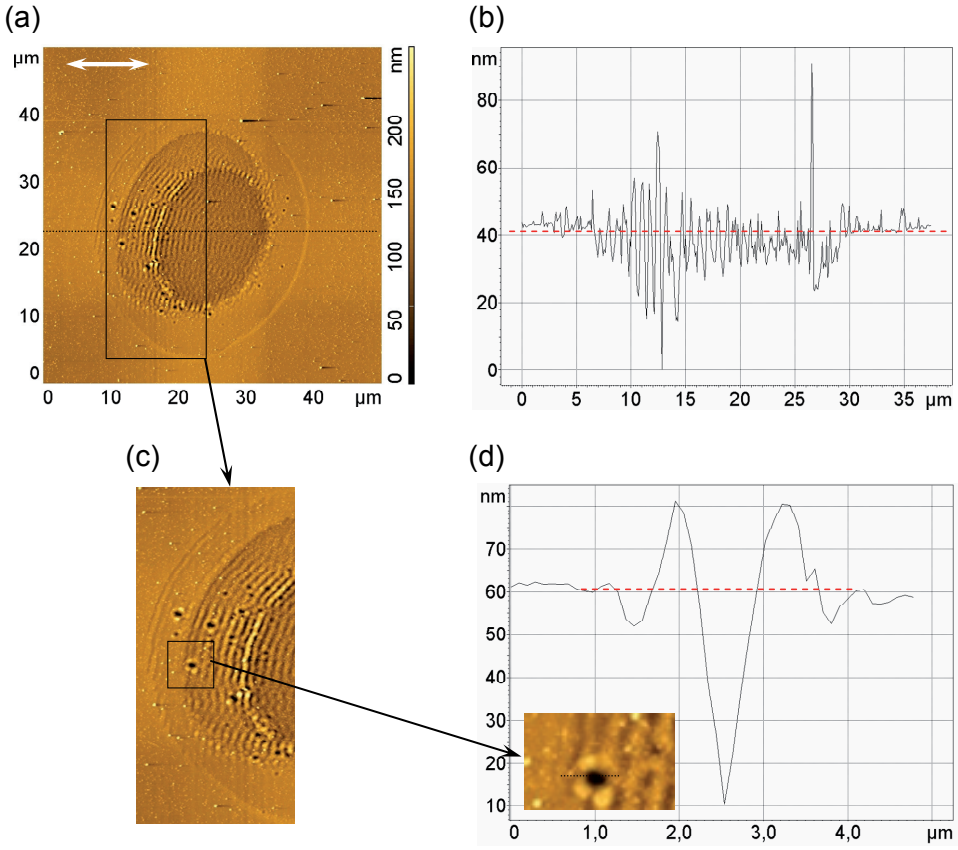

Fig. 5.16: (a) AFM micrograph of ablated spot produced with a very small number of pulses at 1.8 TW/cm² on Si surface with associated depth profile (b) recorded along the dotted line; (c) magnified section of the structured area with corresponding depth profile (d) along the marked line (see insert in (d)): note the particular feature of deep, narrow holes. The double arrow in (a) indicates a direction of laser polarization; the dashed line in (b) and (d) shows the position of the pristine and structured Si surface, correspondingly.

To study the effect of cumulative irradiation we compare single and multipulse ablation experiments on Si (100) and CaF_2(111).

An overview of the typical damage morphology generated by using only very few laser pulses on a Si surface is given in the AFM micrograph in Fig. 5.16 (a). The ablation spot was produced with linear polarized irradiation (double arrow) at intensity I = 1.8 TW/cm², which is about that of the single-shot ablation threshold (I_{th} =2 TW/cm²). The slightly asymmetric form of the spot can be explained by the slight deviation of the laser beam profile from radial symmetry. The micrograph presents an almost circular central part of the damage spot (diameter about of 17 μm), where the applied laser pulses are spatially overlapped.

The central part of the modified area is covered with a series of concentric ripples (Fig. 5.16 (c)). Generation on the surface of such radially expanded concentric waves can be explained by the strong recoil pressure (a few hundred of atmospheres) of the ablated material driving a shock wave into the target [CHR02]. The corresponding depth profile of the ablation spot measured by AFM and shown in Fig. 5.16 (b) has revealed surface modulations at the middle part with a periodicity about of 600 nm, oscillating around the original surface layer with an amplitude of some tens of nanometers.

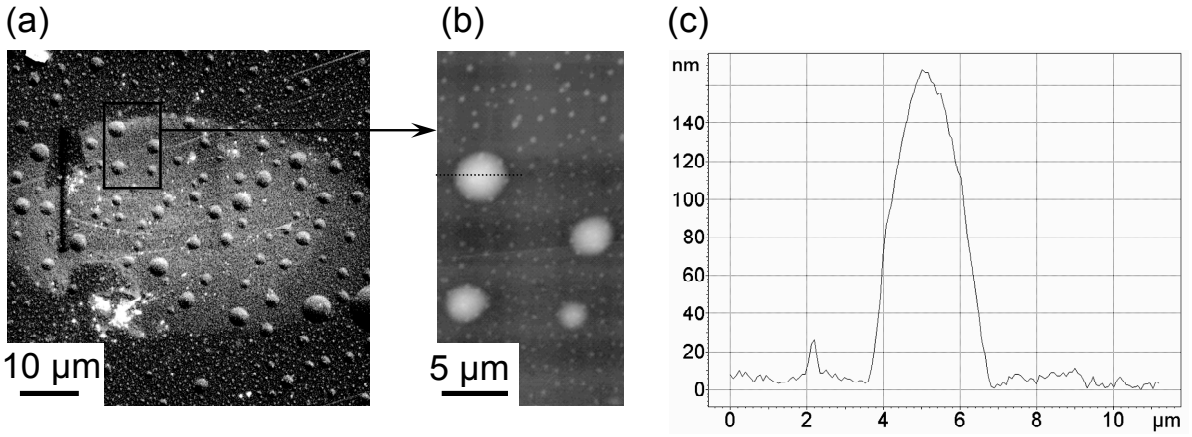

Fig. 5.17: (a) SEM micrograph of laser modified area on CaF_2 surface obtained by applying 100 pulses at intensity 8.2 TW/cm²; (b) magnified AFM image of the region indicated in (a) with a corresponding depth profile along the marked line (c).

Another interesting feature of the laser modified area on Si is shown in the magnified details in Fig. 5.16 (c), namely, the formation of holes with diameter ≈1 μm and depth ≈50 nm, as shown in the depth profile in Fig. 5.16 (d). Edges of the holes rise up to 20 nm above the surface level, which points to the sideways expulsion of the (melted) material. This process could result, for instance, from plasma formation in the lattice defect states and its subsequent expansion creating a strong recoil pressure inside of crystal [MCN96]. After multipulse irradiation the holes at the middle of the ablation crater will be replaced by other structures, but at the edge of the modified area

one can still find some of them. Formation of such holes has been frequently attributed to a locally enhanced carrier density, due to either an inhomogeneous beam profile ("hot spots") or locally enhanced absorption (imperfections in crystal) [BBM04], [BBK02]. In-situ control of the beam profile by CCD camera in our experiments gives us reliable information about the quality of the pulse and excludes the generation of "hot spots". The scenario of inhomogeneous energy absorption due to local imperfections in the crystal lattice looks plausible in this case.

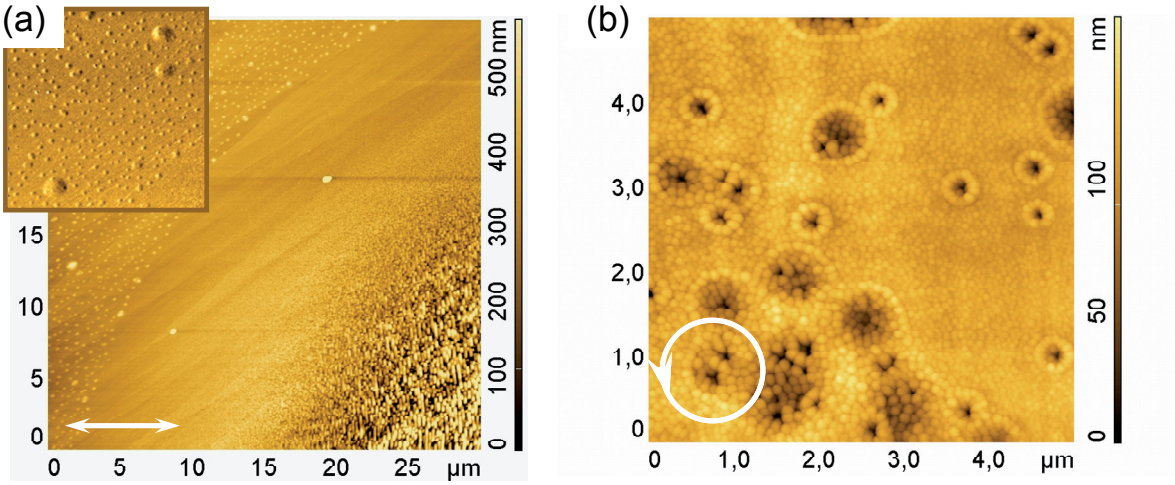

Fig. 5.18: Multipulse femtosecond ablation of CaF_2. (a) Part of ablation crater produced with 2,000 pulses of linear polarization@5.1 TW/cm² at 100 Hz laser repetition rate. Insert (10µm×10µm) exhibits the bubble-structure outside of the ablated area; note ripples formation at the spot center (lower right edge of the panel). (b) Details from the spot edge produced with 10,000 pulses of circular polarization@8.3 TW/cm² at 1 kHz laser repetition rate. The direction of the laser polarization is indicated by arrows in the bottom left.

A similar investigation was performed on dielectrics. Calcium fluoride was irradiated with linearly and circularly polarized pulses at an intensity of about of 8.2 TW/cm², well below the single-shot ablation threshold (I_{th} =30 TW/cm²). Already after the first few pulses, the irradiated surface is modified and nano-bubbles of 200÷300 nm diameter and 20÷40 nm in height are observed. By applying 100 pulses at the same intensity, the irradiated spot as well as its vicinities are covered with a large number of these bubbles, as shown in Fig. 5.17 (a), where the diameter of some bubbles reaches several micrometers and the height is above 150 nm (Fig. 5.17 (b, c)).

By increasing the number of pulses up to several thousand, the typical ripple formation oriented corresponding to the direction of the incident laser field is observed in the center of the ablation spot, and only at the edge of the modified area the original bubbles can be still seen (Fig. 5.18 (a)).

At a still higher irradiation dose (10,000 pulses of circular polarization at 8.3 TW/cm²), the bubbles at the edge region develop to the more complex type of structures (like flowers), as shown in Fig. 5.18 (b). It seems very probable that the "flowers" originate from the bubble-formation with holes in the middle. The depth of the new formations is from 100 up to 150 nm, which is comparable to the bubble height (cf. Fig. 5.17 (c)).

As in silicon, the origin of the bubbles can be related to the nonthermal lattice deformation induced by a recoil pressure due to plasma formation and its subsequent expansion.

In the literature, such morphologies have been reported by Bashir *et al.* [BSH11] as a typical surface modification of dielectric material by a single 25 fs laser pulse. They attributed these structures to pressure-induced compressive stress due to fast laser heating and subsequent relaxation.

The results on Si and on CaF_2 demonstrate that the initial surface modifications (the holes and the bubbles) occur in the irradiated area already after the first laser pulse. At increased irradiation dose, linear periodic structures develop or arrangements of nano-spheres, corresponding to the incident laser electric field. Despite the different optical properties of the irradiated targets, the origin of these structures can be explained by surface self-organization from a strong laser-induced instability [RVR10].

5.4. Multipulse feedback effect

The important role of positive feedback in the ripple formation process has been repeatedly discussed in the literature [YSD84], [TKM07], [RCB06], [CGB12]. In *nonlinear dynamics*, self-organized structure formation originating from high-grade instability is assisted by positive feedback during continuing excitation, resulting in increasing nonlinearity of the effect [BeN01].

In this chapter, the role of the positive feedback in ripple formation is investigated. It is shown that by multipulse irradiation of the silicon surface, the feedback results in an increase of the modified surface area as well as of the feature size and the complexity of generated patterns. Taking into account that femtosecond laser excitation proceeds by individual, well-separated energy pulses, the background physics of this long-lived coupling becomes a very intriguing problem. To shed more light on the feedback mechanism in surface structuring by multipulse femtosecond laser ablation, the effect of temporal pulse separation for constant total incident dose (number of pulses times pulse energy) is studied.

5.4.1. Effect of irradiation dose

Experimental observations indicate that the ablation patterns are fully developed only after a sufficient number of applied laser pulses [BBK02], [RCB06], [MiM07]. This is once again demonstrated by ablation of a Si sample with 50,000 pulses at 2.6 TW/cm². We find in the ablation area (diameter about of ~ 200 µm) (Fig. 5.19 (a)) not only typical ripple structures normal to the laser polarization close to the edge of the irradiated area (Fig. 5.19 (c)), but also a modulation at the central crater walls which is also embossed by the polarization: In Fig. 5.19 (b) one can see the center of the crater covered with linear fine in-depth structures oriented at right angle to the incidence laser field polarization. The outer region is also structured with a very fine zigzag pattern (Fig. 5.19 (d)).

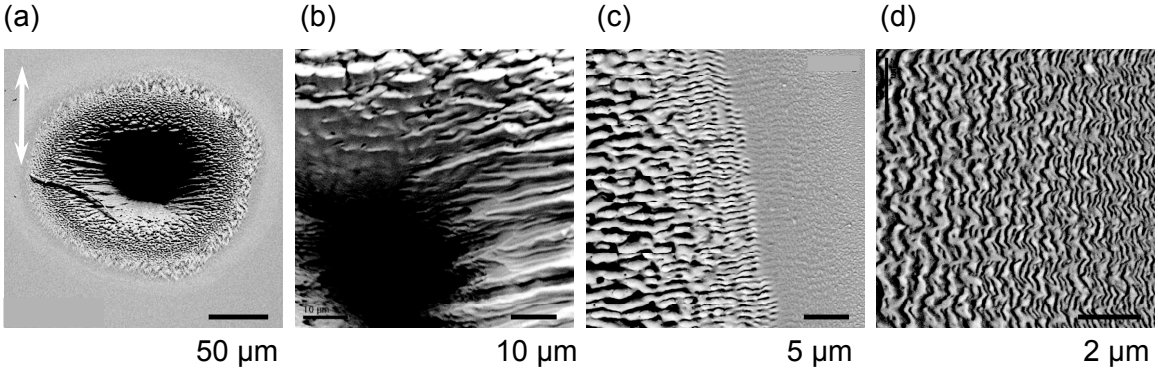

Fig. 5.19: SEM micrographs of ablated spots on Si (2.6·TW/cm^2; 50,000 pulses); the arrow indicates the direction of laser polarization; the length of the scale bars is given below the panels; (a) general overview of the crater; (b) details from the center; (c) fine ripples at the edge; (d) zigzag patterns at the edge/outside.

To check the positive feedback, ablation spots were generated with different numbers of applied pulses. As shown in Fig. 5.20, the central patterns become bigger and more complicated with an increasing number of incident pulses. Already after 3,000 pulses of linear polarization, a homogeneous, rhombic pattern has developed in the middle of the ablated spot (Fig. 5.20 (a)). For circular polarization with the same irradiation dose the central pattern is of radial symmetry (Fig. 5.20 (d)). The correlation between laser polarization and the form/orientation of patterns is getting stronger with increasing number of pulses. After 5,000 pulses an influence of laser polarization is getting more imprinted in the patterns (Fig. 5.20 (b,e)). At irradiation with 10,000 pulses we see, for linear polarization, a long central cleft (Fig. 5.20 (c)) oriented in the direction of laser polarization, and the crater walls are covered by in-depth structures. In the case of circular polarization, the crater form appears like a

funnel with radial symmetry (Fig. 5.20 (f)). Generally, with increasing pulse number, the fine features coalesce to coarser ones, the patterns in the central region begin to collapse.

For a more quantitative analysis we systematically varied the number of incident pulses at constant intensity (2.6 TW/cm^2) and constant repetition rate (1 kHz) and measured both the modified area and, in the central spot region, the ripple density, defined as the number of elementary segments of patterns per unit area. The result, obtained from averaging the data of several series of identical experiments, is presented in Fig. 5.21.

Detailed analysis has revealed that the modified area increases monotonously to a certain irradiation dose (10,000 pulses), after that the changes become fewer and the process reaches saturation (Fig. 5.21 (a)).

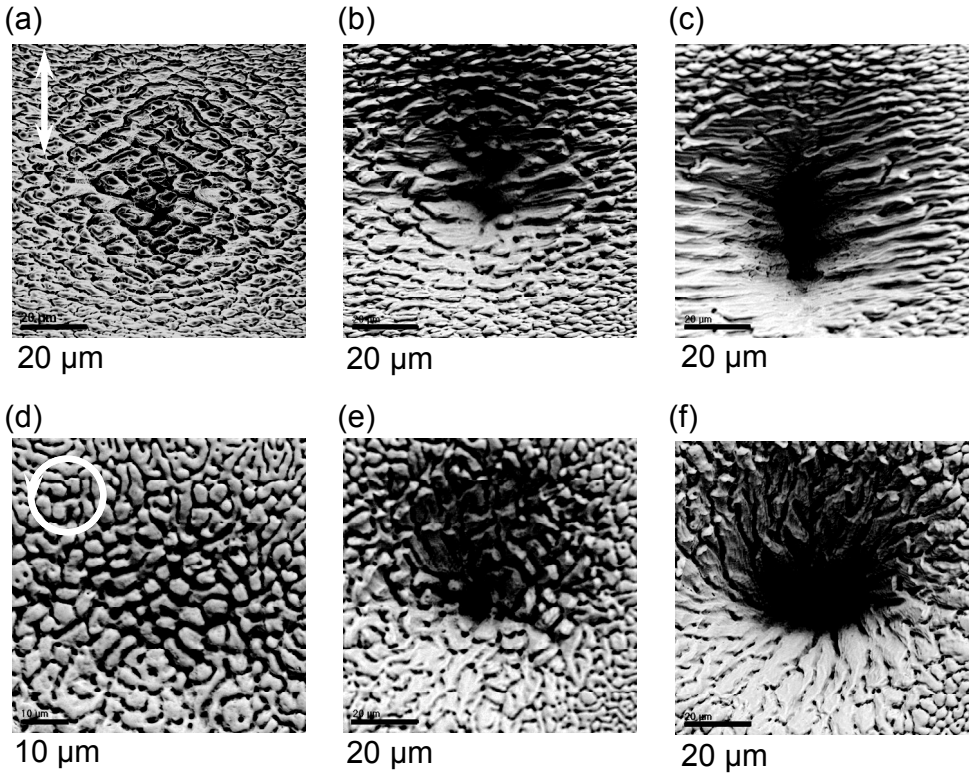

Fig. 5.20: Pattern development at the center of ablated crater (Si); laser intensity I=2.6·TW/cm^2. Upper panels: linear polarization (double arrow), lower panels: circular polarization (circle arrow); (a,d) 3,000 pulses, (b,e) 5,000 pulses, (c,f) 10,000 pulses.

Variation of ripple density with number of pulses presented in Fig. 5.21 (b) is rather complicated. One can specify only the general tendency: pattern becomes coarser with increasing irradiation dose. One should mention here that ripple density/feature size does not vary monotonously with an increasing number of applied

pulses, but in steps, as shown with red dashed line in Fig. 5.21 (b); that reflects the experimentally observed effect of period doubling in ripple formation. In non-linear dynamics, period doubling is characteristic of the structures originated as a result of a relaxation of the system from instability.

In fact, we find the expected feedback effect: similar to the intensity dependence across the spot cross section (cf. Fig. 5.19) we find a regular increase of modified area and of ripple feature size (inversely proportional to ripple density) – with increasing accumulated dose. In a first approximation, the data can be fit by an exponential dependence on the number of pulses N:

(5.3)

$$A = A_0(1 - \exp\{-cN\})$$

for the modified area A, and

(5.4)

$$D = D_0 \exp\{-bN\}$$

for the ripple density D. The pulse number is a measure of accumulated dose $E_{acc} = \alpha N E_{pulse}$ where α is the coupling constant and E_{pulse} is the pulse energy.

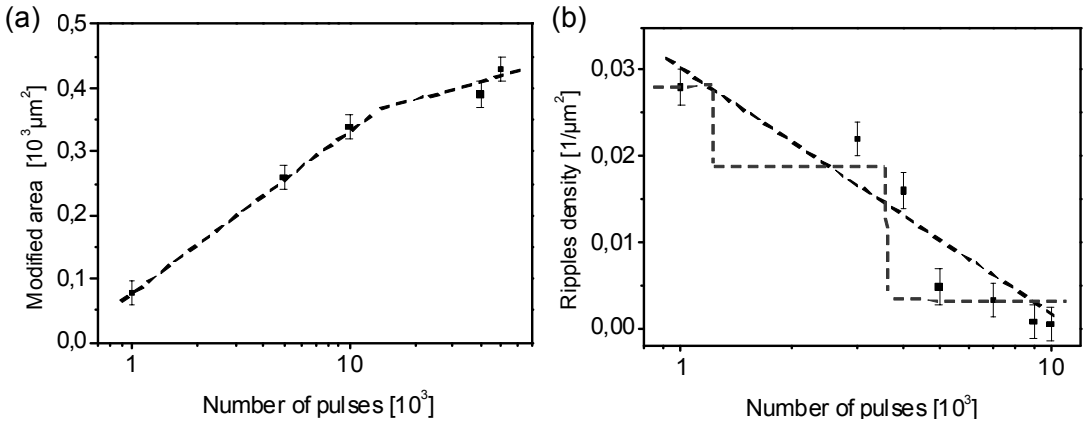

Fig. 5.21: Multipulse ablation of Silicon at laser intensity I=2.6 TW/cm^2. Dependence of (a) ablation area and (b) ripple density on number of pulses. In (b) the straight line is a linear fit to the data (Eq. (5.4)); the stepped fit reproduces the nonlinear period doubling.

The results (Fig. 5.19-Fig. 5.21) support the assumption that the incident pulses do not act individually and independently, but add to the effect of the previous pulses. While the first incident laser pulse and the subsequent desorption of particles create a state of nonequilibrium, the subsequent pulses interact with this "soft" surface and thus act, in a way, collectively [CER06], [RCE07]. The influence of the time separation

between successive pulses is detailed in the next subsection. In respective experiments, the pulse repetition rate is varied, keeping the total incident dose NE_{pulse} fixed.

5.4.2. Effect of pulse separation

When changing the pulse repetition rate from 1 kHz to 1 Hz, i.e. the pulse separation time from 0.001 s to 1 s, the observed patterns change in a way suggesting that at longer separation the accumulated dose is less than at short separation: The complexity is more developed at 0.001 s (Fig. 5.22 (a)), the ripple density is higher at 1 s (Fig. 5.22 (b)).

Again, this effect has been studied systematically and the summarized results of a series of ablation experiments on Si surface are presented in Fig. 5.22 (c). The results demonstrate the dependence of ripple density on pulse separation time for different pulse energy (25 and 32 μJ). The development of surface structures induced by pulses at 25 μJ is more clearly detectable than at 32 μJ. The strongest growth of the ripple density (approximately 60 % of the total amount) happens by changing the time interval between pulses from 0.001 up to 0.01 s. For 25 μJ pulses, the further increase of pulse separation time up to 1 s is accompanied by monotonic increasing of pattern density.

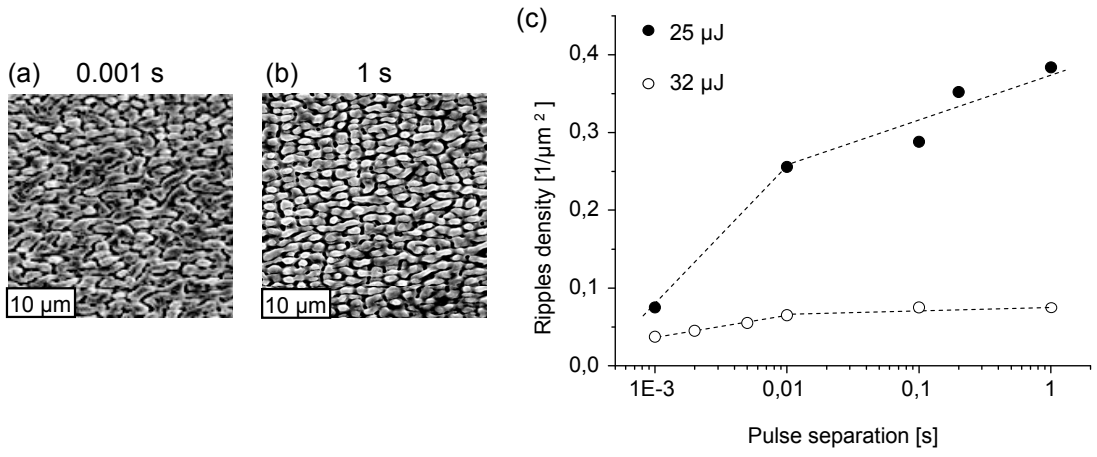

Fig. 5.22: Pattern development at the centre of ablated area on Si surface for a pulse separation time of (a) 1 ms, and (b) 1,000 ms; laser intensity I = 2.6·TW/cm^2 (32 μJ/pulse); 1,000 pulses. Dependence of ripple density on pulse separation time is shown in (c).

The size of structures induced by pulses at higher energy (E_{pulse} = 32 μJ) varies gradually with increasing pulse separation time. With growth of the time interval between pulses from 0.01 s up to 1 s we can hardly register any changes in the ripples density. To understand this insensibility of the pattern density to the pulse separation

time one should take in account that the energy applied per pulse is at about the ablation threshold for silicon (F_{abl} = 0.3 J/cm^2) and it exceeds by 1.7 times the melting threshold (F_m = 0.15 J/cm^2) [CSB99]. In this case the nonthermal melting will be initiated in the irradiated material and the lifetime of the laser induced perturbation can be long enough to be not strongly affected by a variation of the pulse separation time.

The dependence between pulse separation time and modified area shown in ablation experiments on Si and CaF_2 surfaces (Fig. 5.23): Modified area decreases with increasing time interval between successive pulses. By comparison with Fig. 5.21 (a) we can associate the increase of pulse separation with a decrease of coupling efficiency (Fig. 5.24).

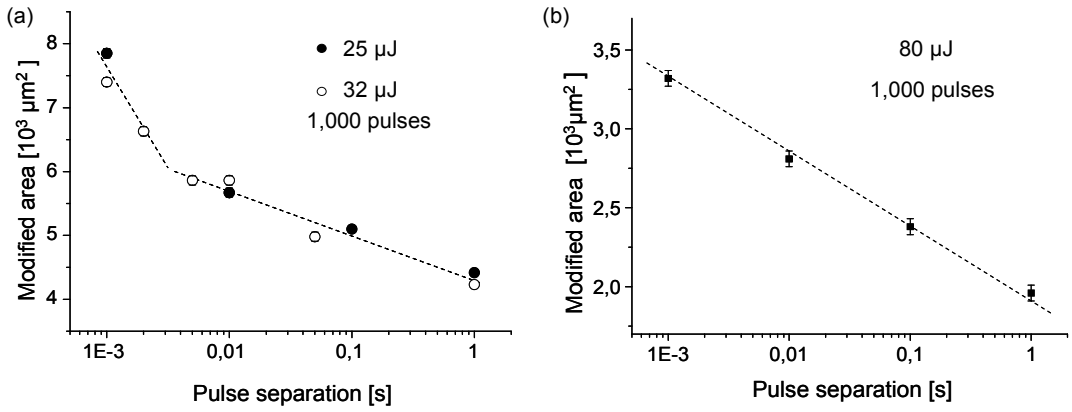

Fig. 5.23: Dependence of modified area on pulse separation time: (a) Si; (b) CaF_2.

In the case of Si, when pulse separation time Δt increases from 0.001 to 0.01s, we detect an abrupt decrease of modified area and feature size of 25% (c.f. Fig. 5.23 (a) and Fig. 5.22 (c)). For Δt from 0.01 to 1 s monotonic decrease of both characteristics were registered.

The same effect, namely, reducing of the modified area with increasing time interval between successive pulses, has been established also on CaF_2 (Fig. 5.23 (b)), though the feature size (ripple period) remained invariable (Fig. 5.25).

An analysis of these results suggests that there are various types of feedback mechanisms between pulses. One should be of thermal character due to electron-phonon coupling. This is more pronounced at a short pulse separation (less than 0.01 s) [RVR10]. Other processes have exhibited very long lifetime pointing, e. g., to the formation of some quasi-particles in the perturbed area like color centers in dielectrics [HWW90].

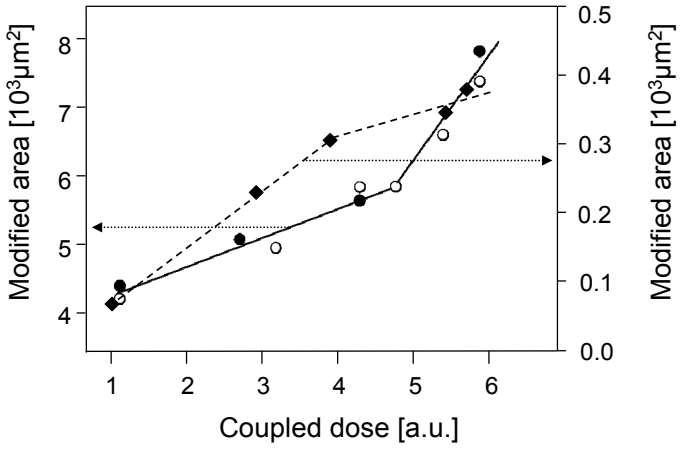

Fig. 5.24: Dependence of modified area on coupled dose. The solid line with scale bar on the left hand side corresponds to Fig. 5.23 (a); the dashed line with scale bar on the right hand side presents experimental data from Fig. 5.21 (a).

In these experiments it has been shown that, indeed, the increase of pulse separation appears to lower the effective dose. For both ripple density (Fig. 5.22) and modified area (Fig. 5.23), the feedback is reduced but still present, even at times as long as 1 second. A comparison between Fig. 5.21, Fig. 5.22 (c) and Fig. 5.23 confirms the similar effects of increasing dose and reducing pulse separation time. Obviously, the system exhibits an unexpectedly long memory of the perturbation and nonequilibrium lasting up to 1 ms.

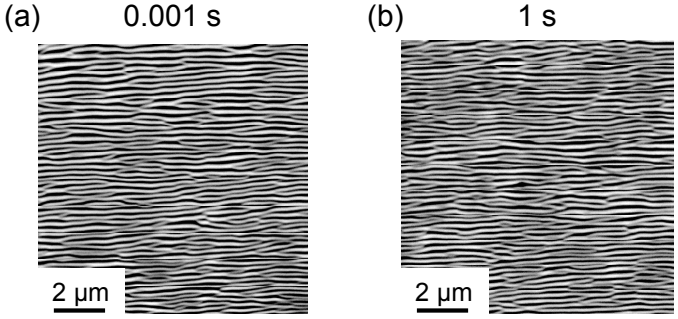

Fig. 5.25: Details from the central part of ablated craters generated on CaF_2 (2,000 pulses; 4.2 TW/cm^2) for a pulse separation time of (a) 1 ms, and (b) 1s. Ripple period in (a) and (b) is ≈200 nm.

5.4.3. Numerical calculations

In this subsection, a possible origin of positive feedback and the long perturbation lifetime is studied. To shed more light on the microscopical changes in material we tried to model a response of silicon on the “collective” action of repetitive irradiation with femtosecond laser pulses.

For the beginning, we propose that free carriers generated in material by the "first" laser pulse may live long enough to be still present when the next pulse arrives.

Thus, they could enhance the coupling of the second pulse, resulting in a step-by-step increase of the perturbation.

Based on Anisimov's two-temperature model [AKP74], assuming different temperatures T_C for carriers and T_L for lattice immediately after the laser pulse, the laser-silicon interaction can be described by the following differential equations [KTV07]:

$$\rho \cdot c_L \cdot \frac{\partial T_L}{\partial t} = div(k_L \cdot grad(T_L)) + \frac{3k_B \cdot n \cdot \rho \cdot c_L}{3k_B \cdot n + \rho \cdot c_L}\left(\frac{T_C - T_L}{\tau_E}\right) \qquad (a)$$

$$\frac{\partial n}{\partial t} = div(D \cdot grad(n)) + \alpha \cdot \frac{I}{h \cdot \nu} + \beta \cdot \frac{I^2}{2h \cdot \nu} - \frac{n - n_0}{\tau_C} \qquad (b)$$

$$\frac{\partial U}{\partial t} = div\left(\frac{U}{n} \cdot D \cdot grad(n)\right) + \left(\frac{h \cdot \nu - E_{gap}}{h \cdot \nu} \cdot \alpha + \frac{2h \cdot \nu - E_{gap}}{2h \cdot \nu} \cdot \beta \cdot I + c \cdot n\right) \cdot I \qquad (5.5)$$

$$+ E_{gap} \cdot \frac{n}{\tau_{C,Auger}} - \frac{3k_B \cdot n \cdot \rho \cdot c_L}{3k_B \cdot n + \rho \cdot c_L}\left(\frac{T_C - T_L}{\tau_E}\right) \qquad (c)$$

$$\frac{\partial I}{\partial x} = -(\alpha + \beta \cdot I + c \cdot n) \cdot I \qquad (d)$$

Eqs. (5.5) (a)-(d) describe lattice temperature T_L, free carrier density n, carrier energy U and the attenuation of lasers intensity I inside the silicon sample, respectively. The carrier energy U and carrier temperature T_C are related by $U = 3k_B \cdot n \cdot T_C$. The increase of lattice temperature T_L (Eq. (5.5) (a)) is determined by the lattice heat conduction and lattice-plasma energy exchange. The temporal evolution of free carrier density n Eq. (5.5) (b)) includes diffusion, generation through linear and two-photon absorption and recombination of the carriers. The change of carrier energy U (Eq. (5.5) (c)) takes into account the diffusion of energy by carrier diffusion, the increase of U due to the excess of photon energy $h\nu$ over the energy gap E_{gap}, free carrier absorption, Auger recombination and the lattice-plasma energy exchange. The last equation (Eq. (5.5) (d)) presents the attenuation of lasers intensity I inside the silicon sample due to linear, two-photon and free carrier absorption. Material parameters for silicon included in Eqs. (5.5) are listed in Appendix.

To reduce the complexity, an effective nonlinear absorption coefficient β is introduced by numerical integration of Eq. (5.5) (b) for an incident Gaussian pulse. Here, we neglect diffusion and recombination during the absorption step that is justified by the short duration of the laser pulses. Fig. 5.26 depicts the resulting

evolution of optical absorption length (left) and the nonlinear absorption parameter (right).

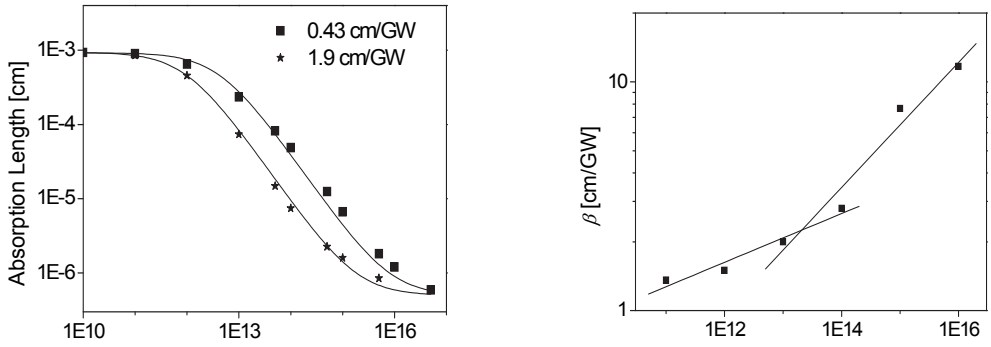

Fig. 5.26: Influence of the incident laser intensity on the effective nonlinear absorption coefficient. The optical absorption length can be well fitted with an average value of absorption coefficient (left graph), since the parameter's dependence on intensity is moderate (right graph).

The actual calculations are based on a finite elements approach in 1D, applying the values of lattice temperature, carrier density and energy at a certain point in time (the pulse-to-pulse delay) as initial conditions for a possible next run. This procedure was repeated several times simulating multipulse irradiation.

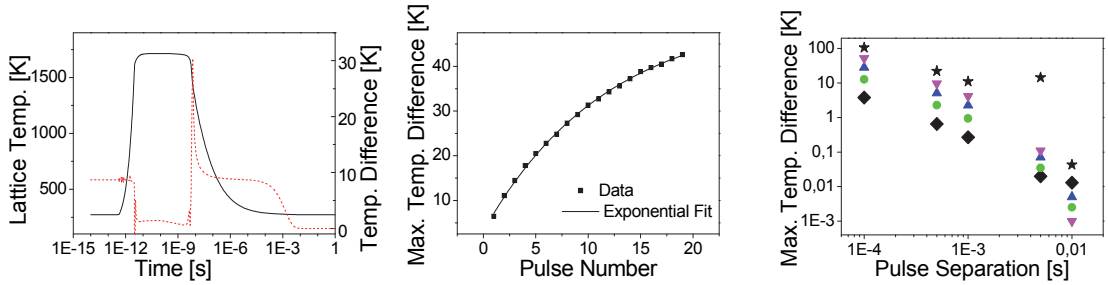

Fig. 5.27: (a) Surface temperature (black solid) and temperature difference between first and twentieth pulse (red dashed) separated by 0.1 ms. (b) temperature difference (red dashed line in (a)) vs. pulse number. (c) Temperature difference vs. pulse-to-pulse delay (fluence decreasing from top [★] to bottom [◆]).

The resulting evolution of surface temperature is shown in Fig. 5.27: well after the laser pulse, the surface appears to be molten for up to several nanoseconds. Thereafter, the surface cools down because of thermal energy redistribution by diffusion and boundary losses. When applying additional laser pulses, however, the temperature in the cool-down phase is increased (dashed trace in Fig. 5.27 (a)). The dependence of the temperature raise on the pulse number appears to be exponential, approaching a maximum for high pulse numbers (Fig. 5.27 (b)). These maxima are displayed in Fig. 5.27 (c) for different pulse-to-pulse delays and fluencies. They

decrease with pulse separation by a power law with an exponent of about 1.5, suggesting thermal diffusion.

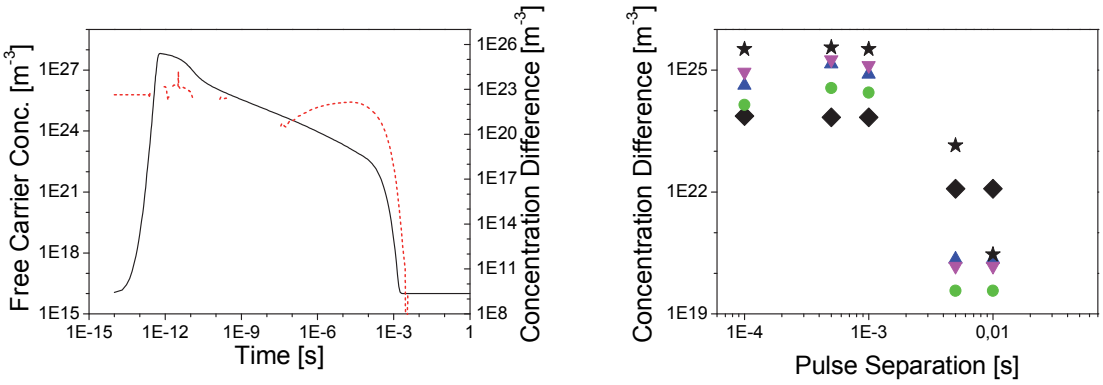

Fig. 5.28: (a) Evolution of the near surface carrier density (black trace) and the difference between first and twentieth pulse (red dashed trace). (b) The dependence of the difference on pulse-to-pulse delay exhibits a sudden drop at about 1 ms, indicating that recombination processes are dominant.

The carrier density exhibits a behavior similar to that of the temperature: after the laser pulse it decreases due to diffusion, followed by a sharp drop due to recombination (Fig. 5.28 (a)). While the certain feedback is also detectable here (dashed trace in Fig. 5.28 (a)), the feedback time appears to be lower compared to that for the temperature since there is an abrupt decrease in the concentration difference when increasing the delay above 1 ms (Fig. 5.28 (b)).

Numerical calculations suggest that free carriers can provide a certain feedback on the short time scale (less than 1 ms), but the main effect is due to the induced lattice perturbation, decaying very slowly by a thermal diffusion process.

5.5. Peculiarities of nanostructures on metallic targets

The present section is focused on properties of ripples induced upon ultrashort pulsed laser ablation on metallic targets. Generally, the direction/shape dependence of ripples on laser polarization observed on dielectrics and semiconductors is also confirmed for metals (Fig. 5.29, Fig. 5.30).

SEM micrographs of a typical ablation spot on a surface of molybdenum (Mo) are presented in the upper panels of Fig. 5.29. The ablation spot, obtained after 500 pulses of linear polarization at a quite high intensity $I \approx 2.5$ TW/cm^2, which is twice that of the single-shot damage threshold [HBC06] ($I > E_a$, see Ch. 3.3.2), has a diameter about of 120 µm. Magnified sections from the center and the edge reveal linear, periodic structures of an average period about of 500 nm and aligned perpendicular to the laser polarization. The same result (ablation spot of diameter ~ 100 nm; ripples period ~ 500 nm) was observed on a surface of tungsten (W) (see the

bottom panel (Fig. 5.29)) after irradiation of the target with 30,000 pulses at laser fluencies well below the ablation threshold (I= 1.2 TW/cm^2) [BSC10].

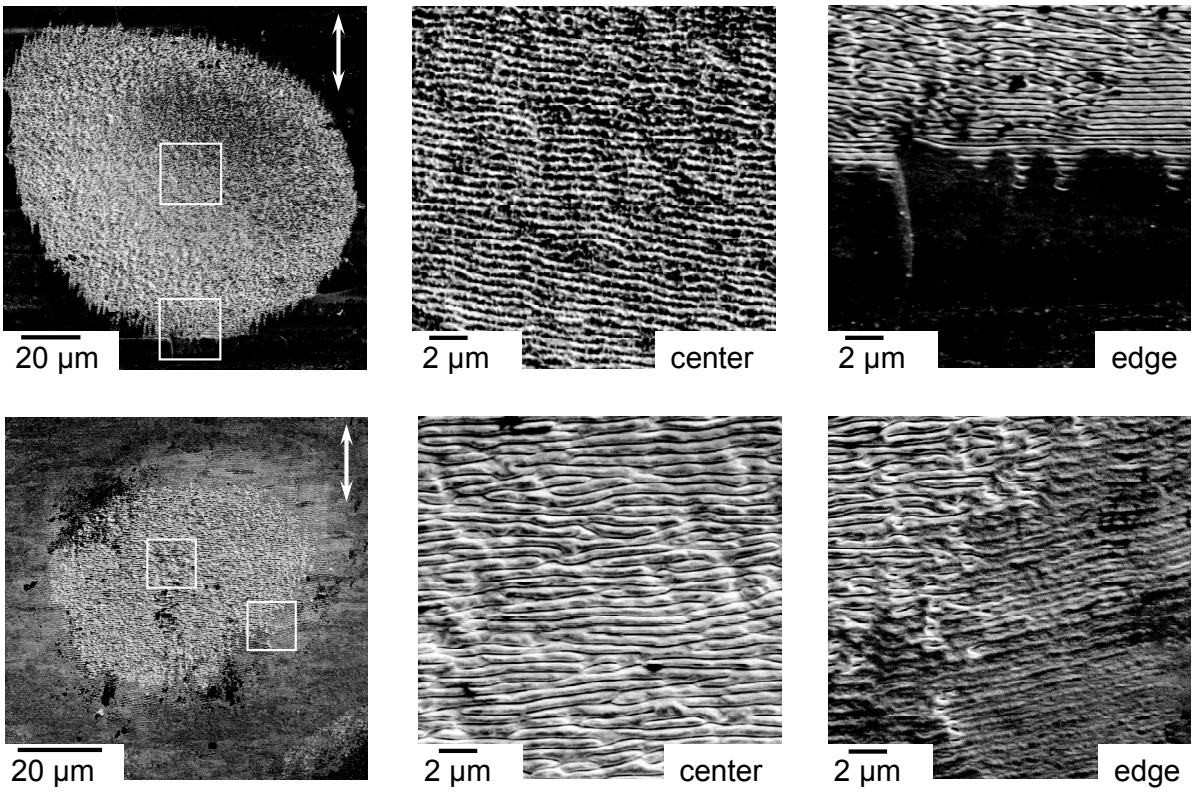

Fig. 5.29: Surface morphologies of ablated craters on molybdenum (upper panels) and tungsten (bottom panels) are generated with linear polarized laser pulses. The polarization of the incident laser field is indicated by double arrows.

From these experiments one can conclude that the lateral *spacing* of the laser induced structures *does not depend* on the Gaussian spatial beam profile, i.e. ripple period is the same within an ablation spot. On the other hand, the *depth* of the modulations is considerably changed depending on the local laser intensity. This peculiar feature is presented in the last photo (lower panel) in Fig. 5.29: structures on the edge of the ablation spot are very shallow in comparison to the central part (cf. details from the center and the edge).

Next, a nanopattern on a surface of molybdenum was produced upon multipulse irradiation with circularly polarized light. The pattern evolution in dependence on the applied irradiation dose was investigated in these experiments. Fig. 5.30 (a) and (b) display several morphological features of a Mo surface ablated with different irradiation doses.

The action of 500 pulses of circular polarization at low intensity 1.3 TW/cm^2, just around the single-shot ablation threshold [HBC06], leads to the formation of an ablated

spot with the modified area of approximately 120-µm-diameter, where only the central part is structured (Fig. 5.30 (a)). A magnified detail from the center exhibits the uniformly distributed pattern consisting of fine grains aligned in short linear arrays with a lateral spacing about of 500 nm.

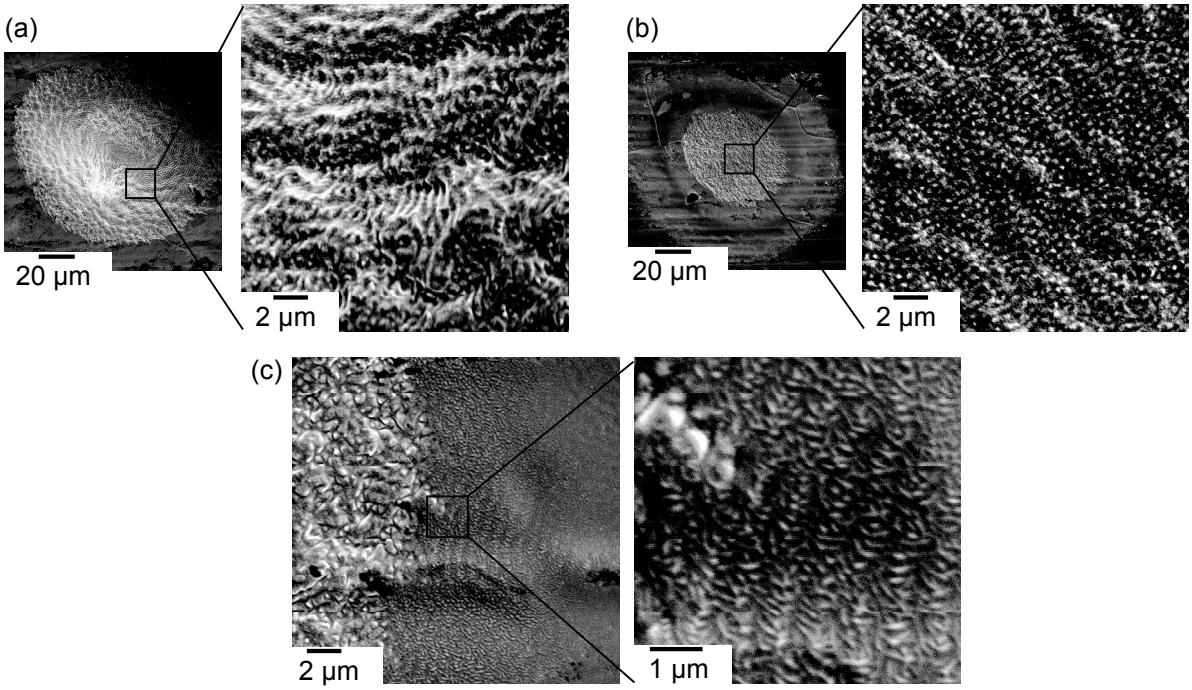

Fig. 5.30: SEM micrographs of nanopatterns on Mo generated with circularly polarized laser pulses. (a) and (b) Ablated spots with enlarged details from the central part induced under irradiation conditions 500 pulses@I=1.3 TW/cm^2 (a) and 1,000 pulses@I=2.4 TW/cm^2 (b), respectively. (c) Evolution of patterns outside of the irradiation spot at increased number of pulses (20,000 pulses at I=1.3 TW/cm^2).

At higher intensity, 2.4 W/cm^2 for 1,000 pulses, a funnel-like crater of a diameter about of 120 µm with a radial symmetry is formed, as shown in Fig. 5.30 (b). The increased irradiation dose leads to a coagulation of fine ripples and results, finally, in more complex self-organized pattern. The crater is covered with a fine nanopattern, which is overlapped by secondary wave-like structures with a period of some microns that can be seen in the magnified details from the central region.

By increasing the number of pulses up to 20,000 at low intensity (1.3 TW/cm^2), significant material modifications such as cracks and wavy deformations well outside of the irradiated area were observed (Fig. 5.30 (c)). Moreover, the outer region is covered by a web-like pattern (see details in Fig. 5.30 (c)), extending far beyond the visible boundary of the laser spot. The pattern does not depend on the laser

polarization. The same effect of the material modification and structure formation far beyond the irradiated area was observed also on silicon (Ch. 5.4, Ch. 6.3).

5.6. Conclusion

Numerous experimental data on femtosecond laser ablation have confirmed that one of the main control parameters for laser-induced periodic surface structures is laser polarization. Generally, for elliptically polarized light, the orientation of obtained patterns is determined by the major axis of polarization ellipse. Moreover, the length of the ripples, varying from long, almost parallel bifurcating lines at linear polarization to random arrangement of nanospheres at circular polarization, depends on the ellipticity of the incident laser field.

Further, an important role of the extended surface defects and surface roughness in pattern formation process has been experimentally established. Influence of the surface defects is even stronger than laser polarization. Taking into account these observations, one can suggest that the structure formation may be related to strain fields in the irradiated target, possibly induced by plasmon coupling between metal colloids and thus accounting for a polarization memory [RVC08].

The evolution of laser-induced surface patterns upon multipulse irradiation (cf. Fig. 5.21 (b), Fig. 5.22), known as a coarsening of the ripples (see Ch. 3.3.4), is experimentally observed on all investigated materials (e.g. Fig. 5.14 (d)), Fig. 5.15, Fig. 5.19, Fig. 5.30). Moreover, detailed examination of the ablation morphologies at high irradiation dose has revealed that the different features are recalling the preceding lower-dose patterns. SEM micrographs from the central part of ablation spots on silicon (Fig. 5.31) illustrate the pattern evolution at increased number of pulses: the low-dose ripple pattern ($\Lambda \approx 700$ nm), perpendicular to the laser electric field (panel (a)) reorganizes into macro-ripplets ($\Lambda \approx 3$ μm), parallel to the laser polarization (panel (b)). Similar effect, namely, the coalescence of very fine structures to coarser and more complex features, is observed independent of material (Ch. 5.1, 5.3 and 5.5). This supports one general formation process for different kinds of ripples, as in self-organized structure formation.

Multipulse feedback plays an important role in the pattern formation process. Experimental study of the influence of pulse-to-pulse separation time indicates an unexpectedly long-term presence of the feedback, involving times up to one second and more before individual pulses act independently. With increased time intervals between successive pulses the feedback becomes weaker. The corresponding

microscopic mechanisms responsible for the long-term perturbations are still under discussion.

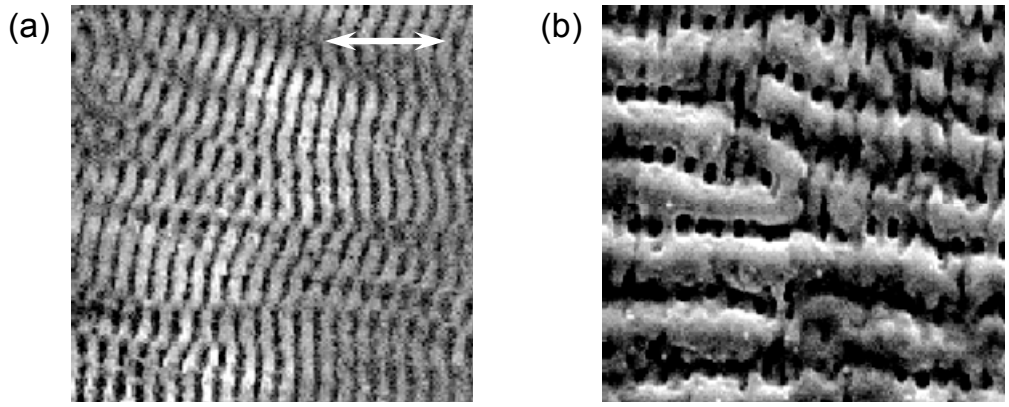

Fig. 5.31: Evolution of ripple nanopattern in the central part of ablation spots generated on silicon at 2.15 TW/cm² at (a) 10 pulses and (b) 50 pulses, respectively. The panel size is 15 μm. The double arrow in (a) indicates the polarization.

In addition, the influence of such laser parameters as orientation and degree of ellipticity of the laser polarization and coupled irradiation dose are analyzed in framework of our theoretical approach and the numerical results are in good qualitative agreement with the experiment.

Despite some peculiar morphological characteristics of ripples on metallic targets, the above-listed control parameters for LIPSS generated on dielectric and semiconducting materials can be also referred to metals. These common controlling parameters for ripples produced on the various targets strongly support our model of self-organized surface formation from laser-induced instability as a common/uniform structure formation mechanism.

6. Impact of nanostructure formation on material properties

In-depth analysis of laser-ablated sample may contribute to a better understanding of the underlying physical mechanism in pattern formation. In this chapter, the surface sensitive studies (AFM, SEM) on structured silicon samples will be supplemented by a cross-sectional analysis of the irradiated area. These measurements reveal the complex microstructural modification of a crystal lattice upon laser irradiation, as well as the possible changes outside the ablated area.

6.1. Electrical properties of nanostructures

In this study the influence on electrical properties is investigated by electrostatic force microscopy (EFM). The measurements are performed in the standard double-pass technique [Mir04]. The basic principles of these methods are described in Ch. 4.4.1.

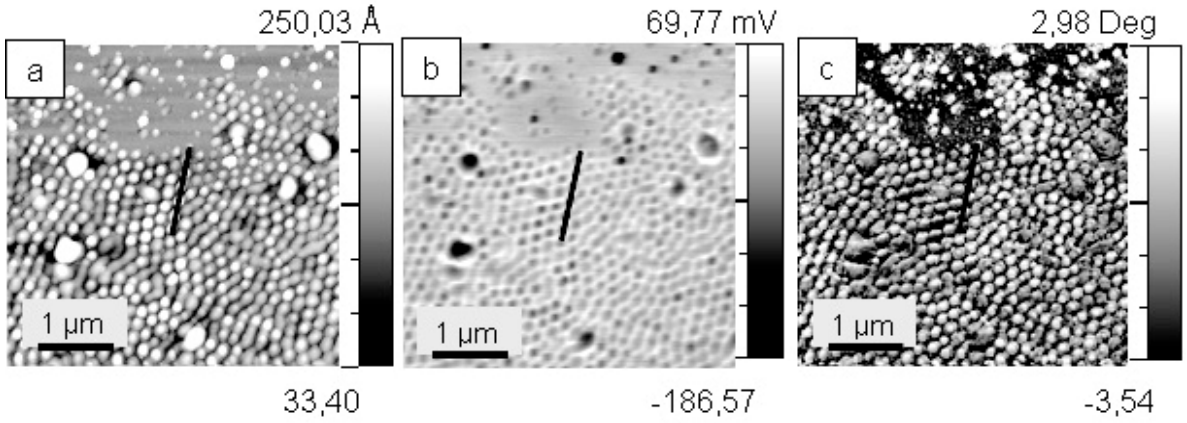

Fig. 6.1: Scanning Probe Microscope micrographs from an ablated spot on p-Si (100). The crater was generated with 1,000 pulses of right circularly polarized light at 1.1 TW/cm². (a) Topography of the investigated area. (b) Distribution of the contact potential on the sample surface. (c) Map of the EFM phase shift by biased voltage (-1 V).

A detail of the ablation crater in the AFM micrograph (Fig. 6.1 (a)) together with the corresponding profile line (Fig. 6.2 (a)), presents the topography of laser-induced patterns on p-Si ($N_A \approx 10^{15}$ cm^{-3}). The ablated crater was produced by 1,000 pulses of intensity 1.1·TW/cm^2 with circularly polarized excitation. The pattern consists of nano-spheres with an average diameter of about 150 nm arranged in long chains with a period ~180 nm. The height of these structures averages between 10 and 40 nm.

A distribution of contact potential (CP) on the structured surface is presented in Fig. 6.1 (b) and Fig. 6.2 (b). A comparison between the topography pictures in Fig. 6.1 (a) and Fig. 6.2 (a) and CP in Fig. 6.1 (b) and Fig. 6.2 (b) shows the CP varying between -186.57 mV at the crests of the nanospheres and +69.77 mV in the valleys.

Astonishingly, the contact potential difference on the structured surface is more than 250 mV (see scale in Fig. 6.1 (b), (b) curve in Fig. 6.2).

A possible origin of the variation of CP could be segregation of p-dopant into valleys (as it will be shown later in Fig. 6.9, the valleys are filled with amorphous silicon) and depletion of holes in crests. This charge separation could occur during the "soft" nonequilibrium state [RCB06] induced by laser irradiation. Moreover, the ablation process changes the crystalline structure of the material. Raman spectroscopy investigations on an identical sample have revealed the existence of phase transformations within the ablated crater in silicon (Ch. 6.2, [CKR04]). Different phases can differ considerably in electrical properties from the initial material and can show a different potential [BTW70].

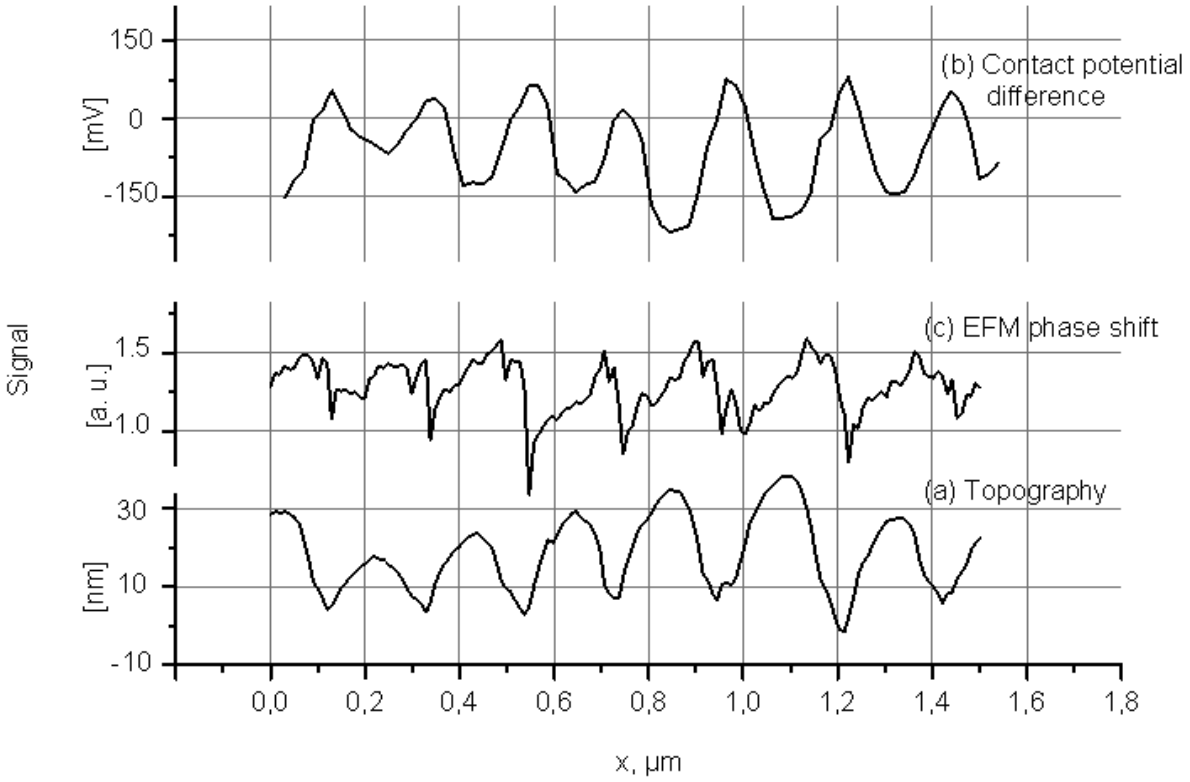

Fig. 6.2: Cross-sections of the areas indicated with thick black lines in Fig. 6.1. (a) is profile line showing the cross-section of the ripple topography, respective to the Fig. 6.1 (a). Curve (b) presents the cross-section of indicated area in Fig. 6.1 (b) (contact potential difference), and curve (c) is the corresponding profile line of EFM phase shift in Fig. 6.1 (c).

The EFM phase shift image is presented in Fig. 6.1 (c) with a corresponding profile line in Fig. 6.2 (c). The phase shift is determined by a derivative of capacitive electric force acting between cantilever and sample or a second derivative of cantilever-sample capacity:

$$\Delta\phi \propto -\frac{1}{2}\cdot\frac{\partial^2 C}{\partial Z^2}\cdot\left(U_0-\phi_{CP}\right)^2. \qquad (6.1)$$

The relative fluctuation of the EFM phase shift is comparable with CP changes (Fig. 6.1 (b) and (c)), but a quantitative analysis is impossible due to the possibility of local capacitance variations.

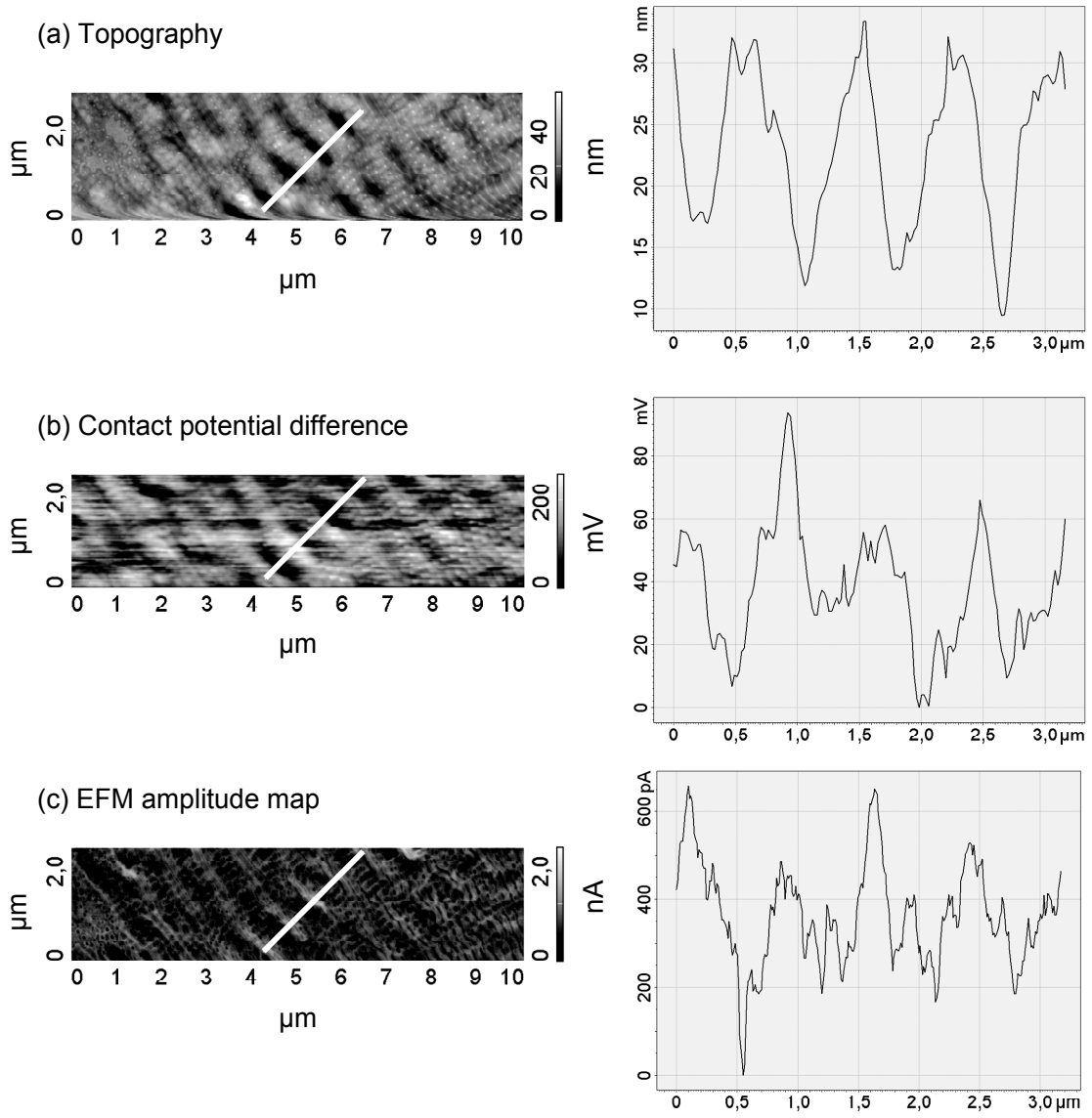

Fig. 6.3: Micrographs from an ablated n-Si sample (500 pulses@1.4 TW/cm²). The topography (a), contact potential difference (b), and the EFM amplitude map (c) with the corresponding cross-sections of the areas indicated with thick white lines.

To better understand the background physics and to explain the observed changes of surface potential, n-doped silicon ($N_D \approx 10^{15}$ cm^{-3}) was investigated under similar

conditions. In contrast to p-doped material, the surface charge in n-Si is expected to be significantly lower and the surface is not depleted, causing a lower potential variation [WRK03], [NiB82].

The results are shown in Fig. 6.3, presenting the topography (a), CP difference (b) and the EFM amplitude maps (c) with the corresponding profiles of the areas indicated with thick white lines. In comparison to results on p-doped silicon (Fig. 6.1), the contrast of CP difference signal (Fig. 6.3 (b)) seems to be inverted and the EFM amplitude (Fig. 6.3 (c)) is approximately proportional to a change in surface potential. Unfortunately, the presence of capacitance variations in the EFM amplitude signal makes a quantitative evaluation of the measured data impossible.

The CP difference is correlated with the topography map, as shown in Fig. 6.3 (cf. (a) and (b)); an increase of the potential corresponds to the heights of the nanopattern, a result that is opposite to the results obtained on p-doped silicon. All the factors discussed above strongly confirm the segregation-scenario.

In conclusion, electrical measurements on the ablated silicon surface have revealed the possibility to create an ordered nanoscaled pattern of the electric surface potential. The potential variations are in the order of about 100 mV. Two main processes can be responsible for this phenomenon, dopant segregation during the ablation with a subsequent self-organized nanostructure formation and a crystal phase transformation of the silicon upon ablation, completely changing the material properties.

6.2. Raman spectroscopic analysis

Raman spectroscopy is a very sensitive method for examining local atomic arrangement and vibrations in solids. To study the microscopic structural changes associated with a laser-induced surface modification upon ablation, micro-Raman (μ-Raman) analysis was performed on the laser treated targets.

The optical setup for μ-Raman measurements was employed in backscattering geometry. The system consisted of a DILOR XY triple spectrometer, combined with an optical microscope with a spatial resolution of 0.58 μm, and a continuous wave, diode pumped Nd:YVO_4 laser (COHERENT Verdi, 532 nm). An objective lens with a magnification of 100 with a numerical aperture of 0.95 was used to focus the laser beam to the spot size of approximately 1 μm on the front face of the investigated sample. The lateral position of the Raman measurements could be varied by a motorized translation stage of 0.2 μm resolution. The spectrometer was on-line

calibrated against a mercury lamp to control temperature shift of the devices with an accuracy of 0.05 cm^{-1}.

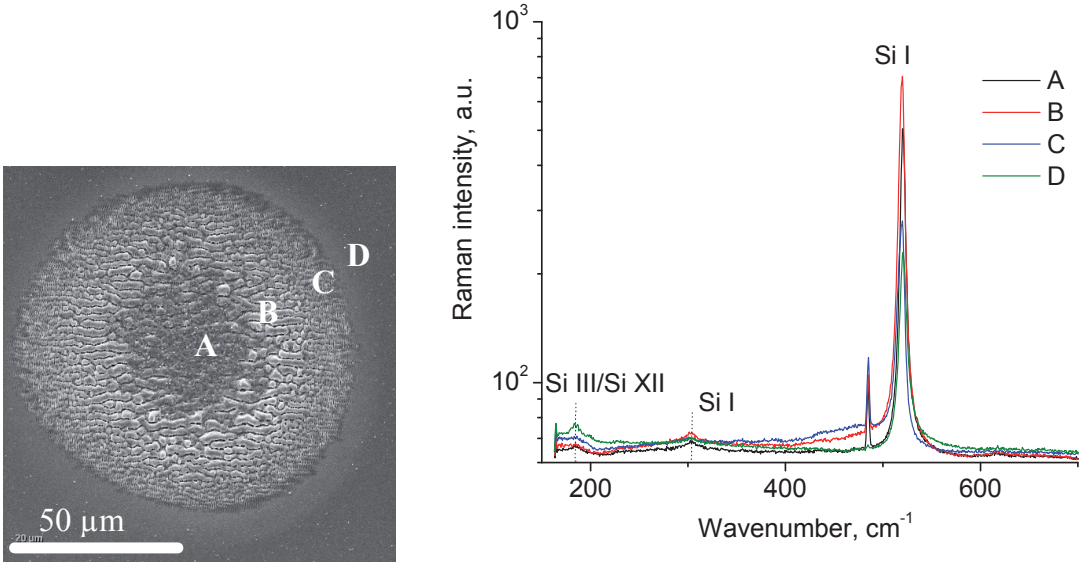

Fig. 6.4: (left) SEM image of the ablation spot on Si(100) (100 pulses, 4.7 TW/cm²) and (right) Raman spectra recorded at different locations across the spot as labeled by letters A, B, C, D.

A typical ablation spot (diameter ~ 100 µm) (Fig. 6.4) was produced by 100 pulses of linear polarization at an intensity of about 4.7 TW/cm² on crystalline silicon. The estimated average depth of the crater is about 0.5 µm. The spot is covered with different types of structures. The letters A, B, C and D in Fig. 6.4 indicate the position of the Raman measurements. The corresponding spectra, taken over a large frequency range, give an overview of the structural modifications in the irradiated material.

The dominant peak in the spectra is centered at ≈520 cm^{-1} und originates from the transverse optical (TO) phonon mode of the perfect crystal [BBM04], [YUK10], corresponding to the diamond structure (Si-I). The small shift of about 1-2 cm^{-1} in the position of the peak can be caused by residual stress in the structured area (A, B, C) in comparison to the unexposed material (D) [DeW96]. The spectrum recorded at the crater bottom (A) is very similar to the spectrum from the unexposed area (D); it reveals high-pressure bcc (Si III) and rhombohedral (Si XII) phases [CKR04], [BBM04] in addition to crystalline silicon (Si I). The signal from the crater bottom is, however, rather poor to exhibit the changes of the crystal structure that are expected in this very strongly modified region. The narrow peak at 485 cm^{-1} in spectra near to the main signal was caused by the scattering signal from the calibration mercury lamp [RRV06].

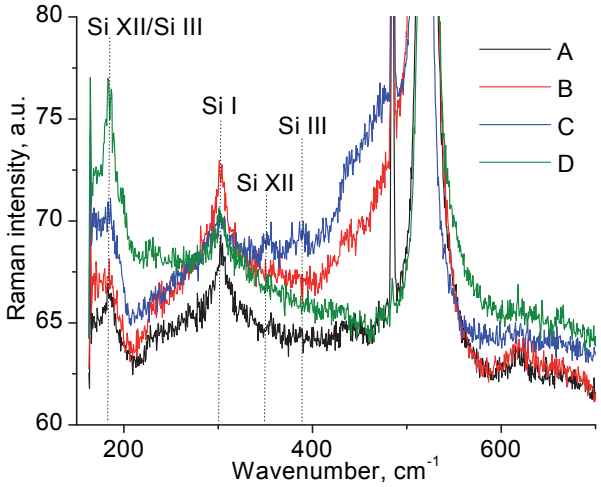

Fig. 6.5: Details of weak peaks in the Raman spectra of irradiated silicon (A, B, C) in comparison to the non-irradiated sample. Colored traces correspond to the same positions as in Fig. 6.4.

Individual details in the Raman spectra of the structured areas A, B and C in comparison to the non-irradiated material (D) are indicated in Fig. 6.5. The signal from the coarse structured area (position B) has revealed an amorphous fraction (a-Si) between 425 and 500 cm^{-1} and at the region of Si III/Si XII peak at 170 cm^{-1}. Measurements at the spot edge (position C) exhibit additional polymorphous peaks (Si III, Si XII) between 350 and 400 cm^{-1} in addition to the growing contribution of a-Si. Such polymorphs are usually attributed to the high-pressure lattice deformations [KOS04]. Indeed, taking into account the high kinetic energies (≈100 eV) of the expelled ions [HWR00] that result in the recoil pressure of some tens of megapascals [CKR04], we expect the appearance of the pressure-induced metastable phase in the ablated area.

Reviewing all Raman data recorded in regions with various types of structures, it has been established that the a-Si is basically deposited at the crater edge, in the heat-affected zone. The finding is further corroborated by TEM analysis of ripple formation on silicon (see Ch. 6.3).

The absence of an amorphous component in the center of the irradiated spot cannot be caused by recrystallization of the amorphous phase; if that were so, we should register a formation of polycrystalline there that is not detectable in the Raman signal (cf. spectrum A in Fig. 6.5). The absence of a homogeneous amorphous layer in the irradiated area allows us to assume that the ripple formation occurs very far from thermodynamic equilibrium. Moreover, the appearance of the metastable phases in the spectra confirms the presence of very steep gradients of pressure and temperature

caused by the ablation that, in turn, causes a steep gradient in crystalline order to the surrounding target material [Rei09].

Motivated by the valuable information about the crystalline changes in silicon during ablation and structure formation, μ-Raman spectroscopy has been applied to the structured insulators to check the possible modifications of the crystal structure.

Raman measurements have been carried out on the ablated area of CaF_2, produced with 5,000 laser shots at an intensity of about of 7.9 TW/cm^2. In Fig. 6.6 one can see the investigated crater (OM microphoto), where the letters A, B, C and D show the position of individual Raman spectra.

In contrast to silicon, Raman investigations on CaF_2 do not show any remarkable material modifications. The detailed analysis of the spot has revealed the appearance of a single Raman peak at ~ 325 cm^{-1} in the ablated region, corresponding to the cubic crystal structure. The same result, namely, the presence of a crystal peak, has also been observed by analysis of the ablated sample of BaF_2.

Here we see that dielectric crystals (CaF_2, BaF_2) do not exhibit any high pressure or temperature induced phase modifications that we found in silicon. This confirms once more that laser-induced nanopattern formation occurs very far from thermodynamical equilibrium via explosive ablation and self-organization.

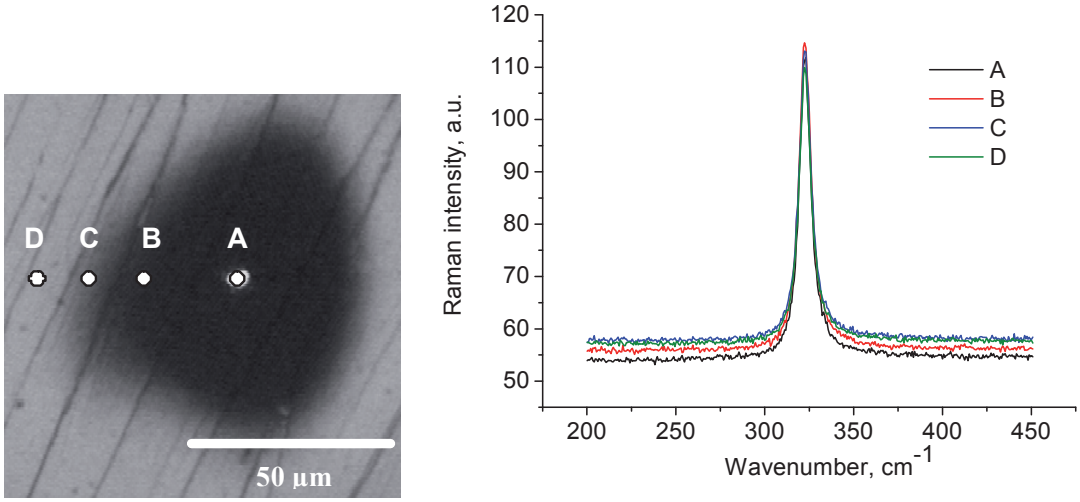

Fig. 6.6: Raman measurements on the ablated area of CaF_2 (5,000 pulses at 7.9 TW/cm^2). (right) Raman spectra from different regions across the ablation spot as indicated by the letters in the optical microscope picture (left) from the center (A) to the edge (D).

6.3. Cross-sectional analysis

Cross-sectional morphology, phase transition and lattice defects associated with laser induced nanopatterns on single crystalline silicon were analyzed by transmission

electron microscopy (TEM). Special attention was paid to the pattern evolution from the centre to the edge within the one ablation spot. Such information can help to understand self-organizing mechanisms leading to occurrence of nanostructures.

6.3.1. Technique

In this study a typical ablation spot (Fig. 6.7) was produced on a commercial *p*-doped Si(100) wafer with 1,000 pulses (Laser system, 100 Hz repetition rate) of linear polarization at an intensity of 1.1 TW/cm², which is well below the single-shot ablation threshold for silicon.

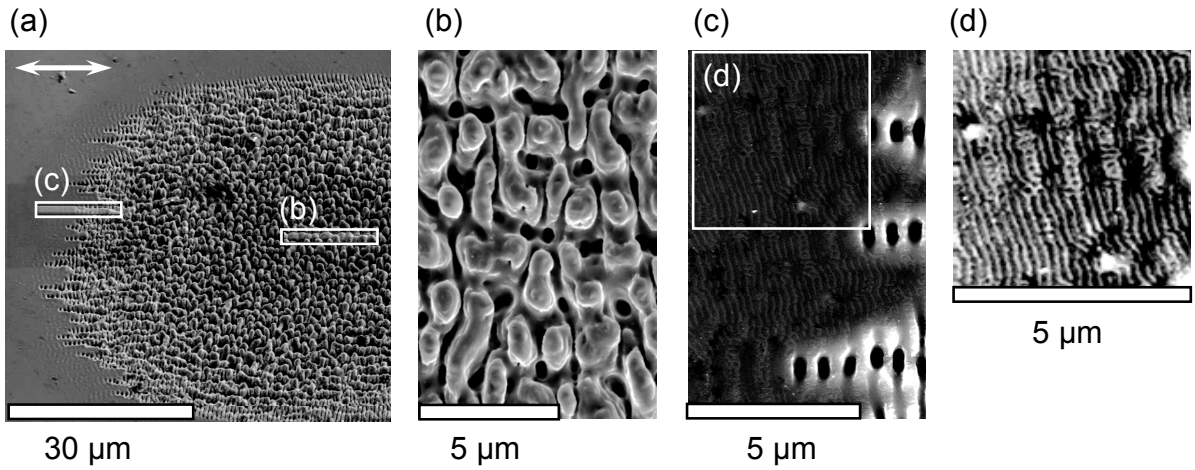

Fig. 6.7: SEM micrographs of details (a) of a typical ablation spot generated with 1,000 pulses at 1.1 TW/cm²; areas selected for TEM investigation are shown in (a) by the white rectangle masks; (b) structure of the central part, (c) surface modulations in the edge and (d) magnified detail of the outer region of the ablated crater marked by the white square in (c) (the contrast is changed to emphasize the fine surface modulations). Double arrow in (a) indicates direction of laser polarization.

Two areas have been chosen for the cross-sectional analysis, as shown in Fig. 6.7 (a). While at the center we register a typical pattern formation for ablated silicon, consisting of the rather flat crests separated by very deep tranches (Fig. 6.7 (b)), the edge pattern exhibits together with well known linear periodic structures oriented perpendicular to the laser electric field (Fig. 6.7 (c)), tiny surface undulations (Fig. 6.7 (d)). Important to note, the undulations are found in the outer region of the crater, which was outside of visible laser spot. The lateral size of these features is about of 100-200 nm and the depth amounts to 10 nm.

In order to investigate the in-depth cross section of the selected areas, two lamellae have been taken off from the center and the edge of the ablation spot (Fig. 6.8) using a FEI Nova Nanolab 600 Dual-Beam workstation, a combination of focused ion beam (FIB)/scanning electron microscope. In practice, first a protection Pt layer

was deposited exactly on the selected (2 µm×10 µm) cut-out regions. Then further material was removed from both sides of the Pt-covered areas by FIB, after that the lamellae were cut free and thinned using a low FIB current until achieving the sample thickness of about 100 nm. High resolution TEM (HR-TEM) of the prepared cross-section samples was carried out using a JEM 4010 transmission electron microscope at an acceleration voltage of 400 kV.

6.3.2. Results

SEM images of the electron transparent cross-section samples from the center and edge of the ablated spot are presented in Fig. 6.8 (a) and (b), correspondingly. Two layers of the protection Pt mask on the top of the sample can be clearly distinguished through their contrast. Similar to analysis with surface sensitive methods (SEM, AFM), we can conclude that at the middle of the spot the in-depth structural modifications are more massive than at the edge, where changes are periodic and not deep.

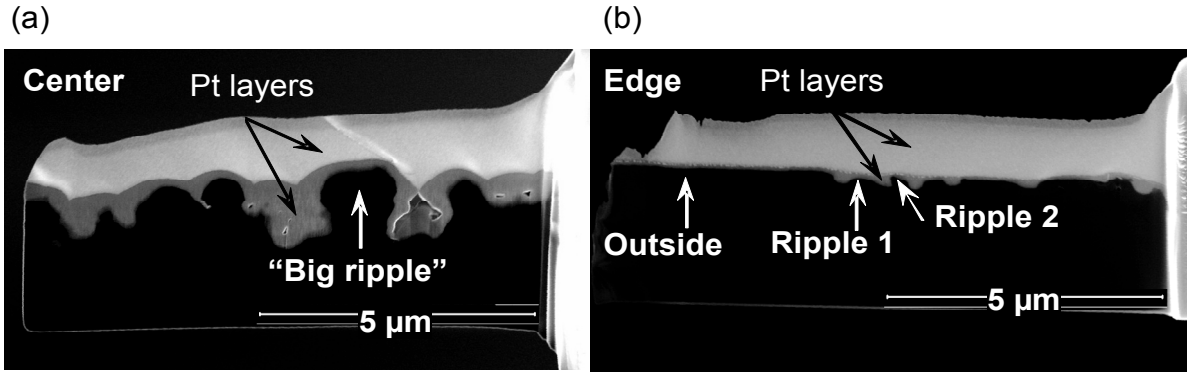

Fig. 6.8: Magnified SEM images of the lamellae prepared for TEM analysis from center (a) and edge (b) of the ablated spot, as shown in Fig. 6.7.

The first investigated detail is shown by the arrow in Fig. 6.8 (a) as "big ripple." An overview of the "big ripple" is generated in bright field TEM (BF-TEM) mode (Fig. 6.9 (a)). The head, or crest, of the ripple exhibits a heavily distorted crystalline material. No amorphous silicon or silicon oxide could be detected at the interface between the top of the "head" and the Pt layer. The fact that the ripples still consist of – though heavily distorted – crystalline material excludes a classical thermal melting as a possible way of structure formation, supporting explosive nonthermal character of material modification (cf. Ch. 2.3.2: *surface reorganization from laser-induced instability*).

The detailed inspection (HR-TEM) of the "head" (Fig. 6.9 (b)) has revealed such extended defects as twin boundaries, stacking faults, dislocation and grains with different lattice orientation. Only in the tranches between the ripples, see "shoulder"-region in Fig. 6.9 (c), very thin about of 20-30 nm amorphous silicon layer can be found (cf. Raman analysis in Ch. 6.2).

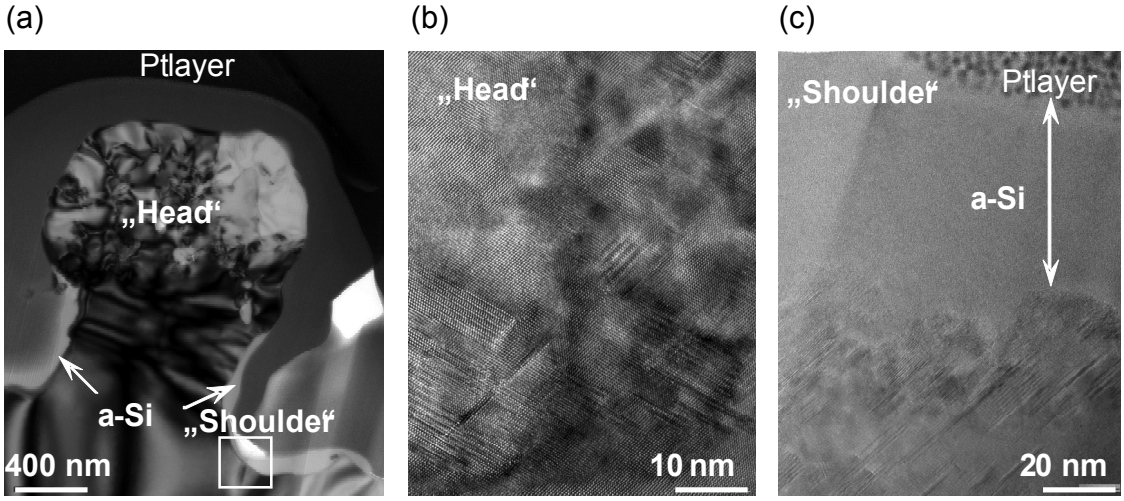

Fig. 6.9: (a) BF-TEM micrograph of the "Big ripple" designated in Fig. 10 (a); (b) and (c) HR-TEM micrographs of the selected in (a) "Head" and "Shoulder" regions.

Even more interesting information is found by analysis of the edge region displayed in Fig. 6.8 (b). The BF-TEM images corresponding to different investigated domains are exhibited in Fig. 6.10. Even well outside of the crater, in the undulations area (Fig. 6.7 (c), (d)), we found a periodic sequence of amorphous and crystalline silicon, continuing the crest/valley sequence. Detail of this region (Fig. 6.10 (a)) exhibits two islands of a-Si in the crystalline silicon. The distance between adjacent amorphous formations as well as their size becomes less at the outside. This confirms the idea that the perturbations spread out from the irradiated area [RVR10].

Next, the BF-TEM image of the ripple at the edge of the crater (Ripple 1 in Fig. 6.8 (b)) is shown in Fig. 6.10 (b). The distinguishing feature of this ripple is that not only shoulders are covered with amorphous silicon (cf. Fig. 6.9 (a)), but also on the top we can observe a small cavity filled with amorphous material. We can consider this formation as intermediate between the well developed ripple at the middle and the first laser modification of the material at the edge.

The last detail of the edge region, Ripple 2 in Fig. 6.10 (c) is located closer to the central part. It is, in general, similar to the "big ripple" of Fig. 6.9 (a). While its top consists also of a heavily distorted region with extended defects, the amorphous silicon layer at the shoulders of the ripple is much thicker.

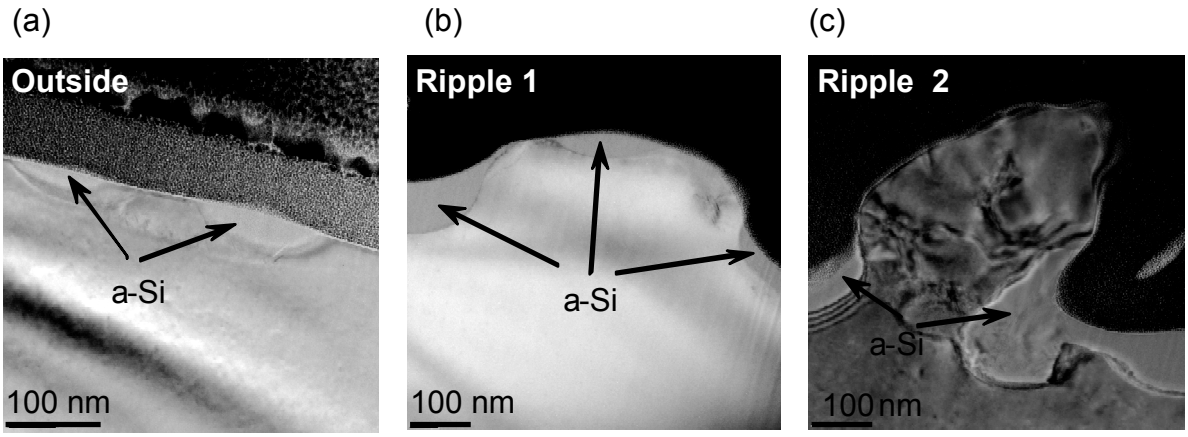

Fig. 6.10: BF-TEM micrographs show appearance of amorphous silicon at the edge region of ablated spot. Position of the fragments (a)-(c) is illustrated in Fig. 6.8 (b).

TEM study of ripple patterns on Si shed light on the complex internal changes of the crystal lattice during ablation and structure formation process. It has been shown that the central part of the ablated spot is almost free from amorphous silicon. Taking into account that the laser pulse has a Gaussian intensity profile, we can conclude that the higher the absorbed laser energy (or the higher irradiation dose) the higher degree of instability is induced at the surface, the farther material from thermal equilibrium, the less amorphous silicon is formed in the area. This study confirms the assumption that the ripples originate, more likely, as a result of surface relaxation from a heavy laser induced perturbation, than from some equilibrium processes like thermal melting. The existence of the modifications in crystal structure well beyond the laser irradiated area can be attributed to a long-lived perturbation that diffuse out of the irradiated area [RVR10].

6.4. Photoluminescence measurements

Detection of the structural surface modifications beyond the visible laser spot (e.g. Fig. 5.19 (d), Fig. 6.7 (c) and (d)), as well as the periodic sequences of amorphous and crystalline silicon registered also far outside the apparently ablated area (Fig. 6.10 (a)), support the idea that the laser-generated perturbations spread outside the irradiated area. To study more these *long-range* modifications in a material, a photoluminescence (PL) analysis has been performed on an ablated Si sample.

The sample for PL measurements was prepared by superimposing lines of irradiated spots, as shown in Fig. 6.11 (a). A room-temperature PL mapping of the structured area (Fig. 6.11 (b)) exhibits wavelike modulation of the band-band (BB) luminescence (1.1 eV) that reproduces well a morphology of the adjacent grooves, scribed in the area (position (2) in Fig. 6.11 (b)). Moreover, this periodic modulation

of band-band luminescence was detected not only inside, but also *well beyond* the ablated area (positions (1) and (3) in Fig. 6.11), where no morphological changes on the surface could be detected. Note that, the band-band luminescence, reflecting the free carrier lifetime, is strongly reduced in the laser-structured area due to an increased surface recombination of excited carriers.

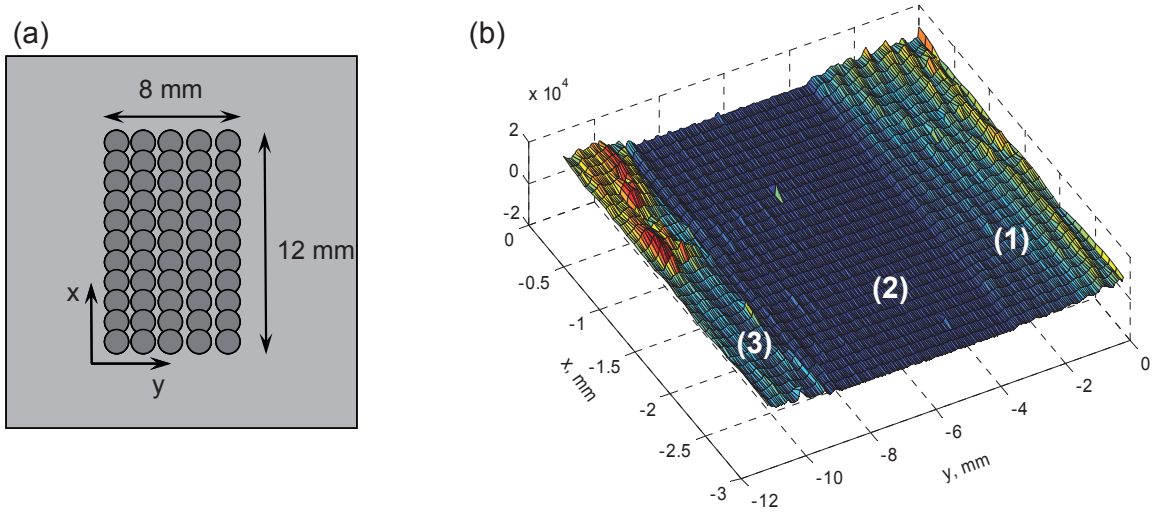

Fig. 6.11: (a) Sketch of laser irradiated silicon sample; the structured area (8×12 mm^2) consists of adjacent grooves of overlapped ablated spots. (b) Band-band PL map of the ablated area (at room temperature); the central dark-blue part (-8mm < y < -2mm) is covered by lines/grooves in x-direction of irradiated spots.

Detailed PL spectrum at 80 K (Fig. 6.12 (a)) has revealed two emission lines: defect-related D1-luminescence (0.8 eV) at 1550 nm [DPT77] and band-band luminescence (1.1 eV) at 1127 nm (Fig. 6.12 (a)). Surprisingly the D1-line, giving evidence of formation of extended defects and dislocations in the crystal, appears also in the *vicinity* of the ablation damage (Fig. 6.12 (b)). Finally, the comparison between the ratio of BB and D1- luminescence reveals the evidence of extended defect formation (*but no signature of thermal melting!*) not only in the directly ablated area, but also in the surrounding material.

The long-range material modifications can be attributed to a *long-lived* laser induced perturbation, slowly decaying by diffusion of the excitation out of the irradiated volume. They play a feedback role by multipulse irradiation in the pattern formation process. These results propose the active role of the irradiated material in pattern formation and support our assumption that ripples occur from laser-induced instability via a self-organized relaxation of the highly excited target material.

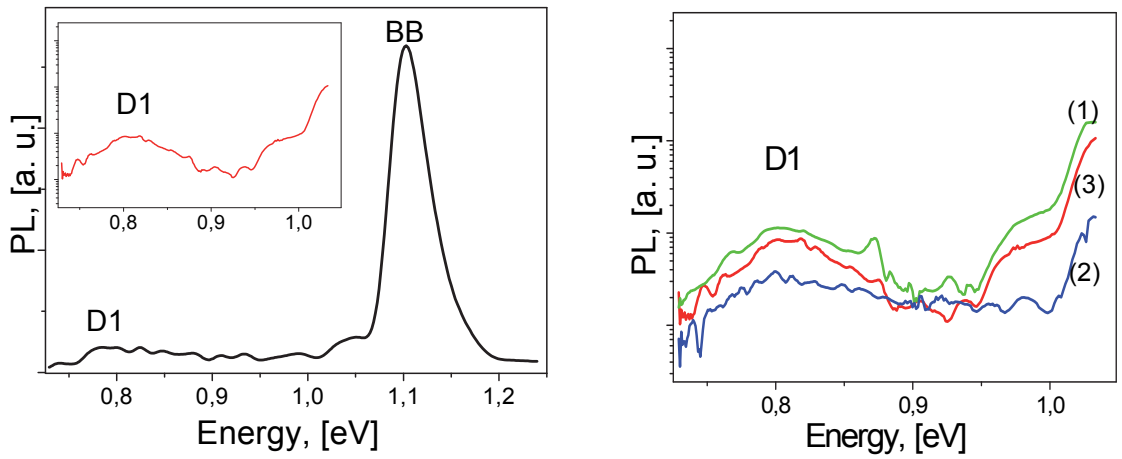

Fig. 6.12: Scanning at 80 K. (left panel) PL spectra of the ablated area exhibits two lines, BB transition (1.1 eV) and D1 (0.8 eV); the inset represents the magnified detail of the D1 line on a logarithmic scale. (right panel) D1 signal in different positions inside and outside the ablated region. The corresponding positions of spectra (1), (2) and (3) are shown in Fig. 6.11 (b)).

6.5. Conclusion

In conclusion, structural cross-section analysis has revealed supplementary data on the intrinsic (crystal lattice) modifications of the laser affected material.

Laser-induced complex modifications extend far away beyond the structured area. Affecting internal material properties, they result in new characteristics of the ablated sample and proposing new applications. For instance, electrical measurements on the ablated silicon sample have revealed the possibility to create nanoscaled potential pattern.

TEM analysis supported by μ-Raman and PL spectroscopy has demonstrated that the central part of an ablation spot produced by femtosecond laser pulses on silicon target consists of highly distorted crystalline phases, rich in defects [SVR10]. This heavily modified area is almost free of amorphous silicon, which is only found at the shoulders of the ripples. Moreover, the fraction of amorphous material increases to the edge of the spot with decreasing irradiation dose. Such modifications indicate very fast, nonthermal surface reorganization from strong material instability induced by ultrafast irradiation and ablation that is consistent with the model of self-organized structure formation.

7. General Conclusions and Outlook

The dissertation is devoted to the phenomena of surface patterning observed upon multipulse femtosecond laser ablation on solid targets. The main purpose of the work is a better understanding of the physical mechanisms involved in the surface pattern formation process.

Taking into account the ultra-fast dynamics of laser-matter interaction, we suggest that the strong surface instability induced at the irradiated area by high-energetic femtosecond laser pulses, relaxes by means of two competing processes (surface erosion and thermal selfdiffusion) that leads to ripple formation.

In framework of this approach, we describe the time evolution of a growing surface profile upon irradiation with polarized laser pulses by an anisotropic noisy Kuramoto-Sivashinsky equation with coefficients, depending on such experimental parameters as laser polarization, laser intensity and the incident angle of laser beam. Numerical solution of this equation reveals a surface topography that agrees well with the ripple patterns obtained under equivalent experimental conditions. Moreover, the theoretical approach also accounts for the well known pattern change upon increasing the irradiation dose; and it also includes the positive feedback experimentally established in pattern formation process. For a further comparison of experimental and numerical results, the model should be improved by including of the non-uniform surface diffusion, pulse-to-pulse development of pattern or taking into account the spatial intensity distribution in the Gaussian beam profile and material parameters that characterize the optical properties of the high-excited state.

Despite of the excellent qualitative agreement between the numerically calculated patterns and our experimental results, and a number of predictions that were proved experimentally, the main critical point of the approach is a quantitative description of the pattern characteristics. In framework of this theory we can estimate quite easily the relative change of pattern, for instance, an increase of the pattern size with an increase of the absorbed laser energy, but absolute values are rather difficult to calculate, because we need parameters for a high-excited material that are not yet available.

The experimental part of this work presents a systematic study of ripple characteristics and self-organization control parameters in the pattern formation process. The research is focused on the collection and thorough analysis of the data on surface structuring observed upon femtosecond laser ablation on the various target materials. The important role of laser polarization as main control parameter in the pattern formation was confirmed in numerous experiments. It was demonstrated that

the ripple orientation and the ripple shape are dictated by the incident laser electric field. Further, we obtained that the ripple period depends on both on the applied irradiation dose and on the target material as shown in Tab. 1.

Target material	CaF_2, MgF_2, Al_2O_3, NaCl	n-Si, p-Si	Fused silica	Tungsten, Molybdenum
Period of ripples	100÷300 nm	100 nm÷10 µm	200÷500 nm	400÷600 nm

Tab. 1: Period of surface structures observed on different types of targets after femtosecond laser ablation.

Additionally, a varying of the ripple size at the same irradiation spot does not follow smoothly to the Gaussian beam profile, but it changes gradually, exhibiting a typical behavior for structures originating from instability.

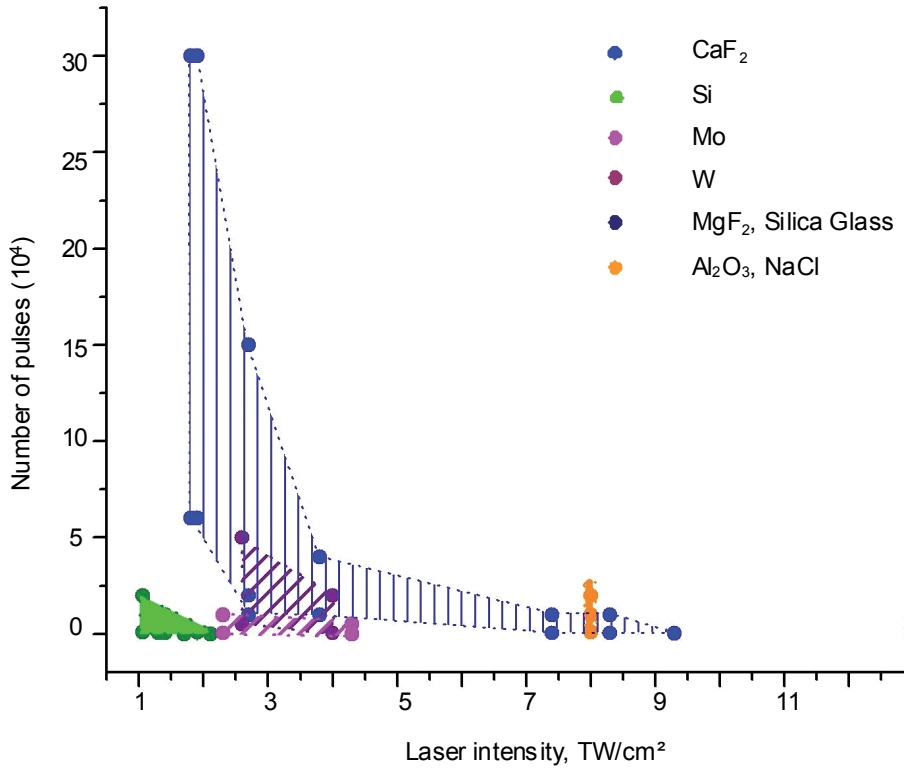

Fig. 7.1: Occurrence of ripple structures on different targets in dependence on the applied irradiation dose (laser intensities × number of pulses).

Summarized results, exhibiting regions of ripple formation at different irradiation dose on various targets, are presented in the Fig. 7.1. The investigation reveals the existence of appropriate windows of laser intensity and number of pulses for

successful development of ripple patterns on the different target materials. We see that for some samples such as, for instance, CaF_2, formation of ripples has been registered in a quite wide range of the applied irradiation dose. For other targets, like NaCl or Al_2O_3, only a very limited range could be found for surface structuring. Moreover, application of a large number of pulses at lower intensities is established as the favourable regime for the development of surface ripples on the all investigated targets.

Generally, the occurrence of ripple structures on opaque as well as on transparent targets, irrespective of their crystallographic structures and conductive properties indicates a universal character of pattern formation phenomenon. Moreover, taking into account the similarity of surface structures generated on different materials, we can conclude that the ripple formation process is not defined by physical properties of a target material in thermodynamic equilibrium, but a high-excited material state caused by femtosecond pulse irradiation has to be considered here. All these experimental observations strongly support the self-organization mechanism of ripple formation.

8. Appendix

Model parameters [KTV07]:

Density: $\rho = 2.3$ g cm^{-3}.
Energy gap: $E_{\text{gap}} = 1.1$ eV.
Lattice specific heat: $c_L = 0.88$ J g^{-1}K^{-1}.
Lattice thermal conductivity: $\kappa_L = 1.5$ Wcm^{-1} K^{-1}.
Linear absorption coefficient: $\alpha = 1.12 \times 10^3$ cm^{-1}.
Two-photon absorption coefficient: $\beta = 9$ cmGW^{-1}.
Free carrier absorption coefficient: $\alpha_{FCA} = c \times n$ with $c = 4 \times 10^{-18}$ cm^2.
Recombination time: $\tau_C = \dfrac{1}{\dfrac{1}{\tau_0} + \dfrac{1}{\tau_{Auger}}} + \tau_\infty$, where $\tau_{Auger} = \dfrac{1}{\gamma \cdot n^2}$;
with $\gamma = 4 \times 10^{-31}$ cm^6 s^{-1}.
Ambipolar diffusion coefficient: $D = 18$ cm^2 s^{-1}.
Energy relaxation time: $\tau_E = \tau_{E0} (1 + (n/n_1)^2)$
with $n_1 = 2 \times 10^{21}$ cm^{-3} and $\tau_{E0} = 0.5$ ps.

9. Acknowledgements

First of all, I would like to thank my dissertation supervisor, Prof. Dr. Jürgen Reif, for giving me the opportunity to work on such an interesting and fascinating research topic, for his professional guidance, valuable support and encouragement throughout the work. I am grateful for his thorough and constructively critical proof-reading of the first thesis drafts, for the insightful comments that contributed to the progress of my work.

I would like to express my deepest thanks to my dissertation referees, Prof. Dr. M. Bestehorn and Prof. Dr. S. Vallete for expert evaluation of the manuscript and for their valuable comments.

My sincere thanks and appreciation belong to my colleagues at the Chair of Experimental Physics II and Joint Lab IHP/BTU for their help and cooperation as well as for friendly, cordial atmosphere in our group.

I am particularly grateful for the assistance in analysis of surface morphologies with SEM and AFM given by Dr. W. Seifert, Dr. M. Ratzke, Dr. G. Jia, Dipl.-Phys. M. Holla and Dipl.-Phys. H.-M. Krause. Special thanks belong to Dr. F. Costache and Prof. Dr. R. Schmid for sharing their experience and knowledge with me.

I gratefully acknowledge Prof. Dr. M. Bestehorn and Dr. S. Varlamov for their close collaboration and fruitful discussions during the development of the model and the performance of the numerical calculations.

I extend my warmest gratitude to Carolyn Prescott for the editing of my manuscript.

Finally, the special recognition goes out to my family for their patience, encouraging and supporting me and for never letting me doubt myself during all these years.

10.References

[AAM88] M. Agranat, S. Anisimov, B. Makshantsev; Appl. Phys. B (1988) 47, 209.

[ABF77] S. Anisimov, V. Benderskii, G. Farkas; Sov. Phys.-Uspekhi (1977) 20, 467.

[AHR03] P. Allenspacher, B. Huettner, W. Riede; Proc. SPIE (2003) 4932, 358.

[AKP74] S. Anisimov, B. Kapeliovich, T. Perelman; Sov. Phys.-JETP (1974) 39, 375.

[ALS99] D. Ashkenasi, M. Lorenz, R. Stoian, A. Rosenfeld; Appl. Surf. Sci. (1999) 150(1), 101.

[Ani95] S. Anisimov, V. Khokhlov; Ch. *„Effect of Ultrashort Laser Pulses"* in *Instabilities in Laser-Matter Interaction* (CRC Press, 1995), pp. 63-65.

[AnL02] S. Anisimov, B. Lukyanchuk; Physics-Uspekhi (2002) 45(3), 293.

[ArW68] E.T. Arakawa, M.W. Williams; J. Phys. Chem. Solids (1968) 29, 735.

[AsM76] N.W. Ashcroft, N.D. Mermin; *Solid State Physics* (Harcourt College Publisher, 1976), pp. 373-414.

[ASR00] D. Ashkenasi, R. Stoian, A. Rosenfeld; Appl. Surf. Sci. (2000) 154-155, 40.

[Bae96] D. Baeuerle; Ch. *„Modelling of Pulsed-Laser Ablation"* in *Laser Processing and Chemistry* (Springer, 1996), pp. 209-226.

[BBK02] J. Bonse, S. Baudach, J. Krüger, W. Kautek, M. Lenzner; Appl. Phys. A (2002) 74, 19.

[BBM04] J. Bonse, K.-W. Brzezinka, A.J. Meixner; Appl. Surf. Sci. (2004) 221, 215.

[BeG66] H.B. Bepp, A. Gold; Phys. Rev. (1966) 143, 1.

[BeN01] M. Bestehorn, K. Neuffer; Phys. Rev. Lett. (2001) 87, 046101.

[BFZ05] M. Bashevoy, V. Fedotov, N. Zheludev; Opt. Exp. (2005) 13, 8372.

[Bir65] M. Birnbaum; J. Appl. Phys. (1965) 36, 3688.

[Blo74] N. Bloembergen; IEEE Journal of Quantum Electronics, (1974) 10, 375.

[BMS05] J. Bonse, M. Munz, H. Sturm; J. Appl. Phys. (2005) 97, 013538.

[BoH03] A. Borowiec, H.K. Haugen; Appl. Phys. Lett. (2003) 82, 4462.

[BoK10] J. Bonse, J. Krueger; J. Appl. Phys. (2010) 108, 034903.

[BOM04] A. Bulgakov, I. Ozerov, W. Marine; Appl. Phys. A (2004) 79, 1591.

[BrH88] R.M. Bradley, J.M.E. Harper; J. Vac. Sci. Technol. (1988) 6, 2390.

[BRK09] J. Bonse, A.Rosenfeld, J. Krueger; J. Appl. Phys. (2009) 106, 104910.

[BSC10] J. Byskov-Nielsen, J.-M. Savolainen, M.S. Christensen, P. Balling; Appl. Phys. A (2010) 101, 97.

[BSH11] S. Bashir, R.M. Shahid, W. Husinsky; Radiation Effects and Defects in Solids (2011) 166, 30.

[BSR06] V.R. Bhardwaj, E. Simova, P.P. Rajeev, C. Hnatovsky, R.S. Tylor, D.M. Rayner, P.B. Corkum; Phys. Rev. Lett. (2006) 96, 057404.

[BSS00] J. Bonse, H. Sturm, D. Schmidt, W. Kautek; Appl.Phys. A (2000) 71, 657.

[BTW70] M.H. Brodsky, R.S. Title, K. Weiser, G.D. Pettit; Phys. Rev. B (1970) 6, 2632.

[BuB02] N. Bulgakova, I. Bourakov; Appl. Surf. Sci. (2002) 197-198, 41.

[Car01] G. Carter; J. Phys. D: Appl. Phys. (2001) 34, R1-R22.

[CCV05] M. Castro, R. Cuerno, L. Vazquez, R. Gago; Phys. Rev. Lett (2005) 94(1), 016102.

[CER06] F. Costache, S. Eckert, J. Reif; Appl. Surf. Sci. (2006) 252, 4416.

[CER08] F. Costache, S. Eckert, J. Reif; Appl. Phys. A (2008) 92, 897.

[CGB12] J.P. Colombier, F. Garrelie, P. Brunet, A. Bruyere, F. Pigeon, R. Stoian, O. Parriaux; Journal of Laser Micro/Nanoengineering (2012) 7(3), 362.

[ChG02] T.Y. Choi, C.P. Grigoropoulos; J. Appl. Phys. (2002) 92, 4918.

[CHR02] F. Costache, M. Henyk, J. Reif; Appl. Surf. Sci. (2002) 186, 352.

[CHR03] F. Costache, M. Henyk, J. Reif; Appl. Surf. Sci. (2003) 208-209, 486.

[CKR04] F. Costache, S. Kouteva-Arguirova, J. Reif; Solid State Physics (2004) 95-96, 635.

[ClE89] S.E. Clark, D.C. Emmony; Phys. Rev. B (1989) 40, 2031.

[CMK94] E. Chason, T.M. Mayer, B.K. Kellerman, D.T. McIlroy, A.J. Howard; Phys. Rev. Lett. (1994) 72, 3040.

[CMN96] B. Chichkov, C. Momma, S. Nolte, F. von Alvensleben, A. Tünnermann; Appl. Phys. A (1996) 63, 109.

[Cos07] F. Costache; Diss. *„Dynamics of Ultra-short Laser Pulse Interaction with Solids at the Origin of Nanoscale Surface Modification“* (Shaker, 2007).

[CrH07] T.H.R. Crawford, H.K. Haugen; Appl. Surf. Sci. (2007) 253, 4970.

[CSB99] A. Cavalleri, K. Sokolowski-Tinten, J. Bialkowski, M. Schreiner, D. von der Linde; J. Appl. Phys. (1999) 85, 3301.

[CuB95] R. Cuerno, A.-L. Barabasi; Phys. Rev. Lett. (1995) 74, 4746.

[CZM11] M. Cornejo, B. Ziberi, C. Meinecke, D. Hirsch, J.W. Gerlach, T. Hoeche, F. Frost, B. Rauschenbach; Appl. Phys. A (2011) 102, 593.

[Del75] N.B. Delone; Uspehi Phys. Nauk (1975) 115, 361.

[DeW96] I. De Wolf; Semicond. Sci. Technol. (1996) 11, 139.

[DHB06] H. Dachraoui, W. Husinsky, G. Betz; Appl. Phys. A (2006) 83, 333.

[DPT77] N. Drozdov, A. Patrin, V. Tkachev; Phys. Status Solidi (1977) 83, K127.

[DRD09] D. Dufft, A. Rosenfeld, S.K. Das, R. Grunwald, J. Bonse; J. Appl. Phys. (2009) 105, 34908.

[DSS09] B. Dusser, Z. Sagan, H. Soder, N. Faure, J.P. Colombier, M. Jourlin, E. Audouard; Opt. Exp. (2009) 18, 2913.

[DSY82] H.M. van Driel, J.E. Sipe, J.F. Young; Phys. Rev. Lett. (1982) 49, 1955.

[EAC99] J. Erlebacher, M.J. Aziz, E. Chason, M.B. Sinclair, J.A. Floro; Phys. Rev. Lett. (1999) 82, 2330.

[EHW73] D.C. Emmony, R.P. Howson, L.J. Willis; Appl. Phys. Lett. (1973) 23, 598.

[EZS84] V.I. Emeljyanov, E.M. Zemskov, V.N. Seminogov; Sov. J. Quantum Electron. (1984) 14, 1515.

[FLI84] J.G. Fujimoto, J.M. Liu, E.P. Ippen, N. Bloembergen; Phys. Rev. Lett. (1984) 53, 1837.

[GCP11] F. Garrelie, J.-P. Colombier, F. Pigeon, S. Tonchev, N. Faure, M. Bounhalli, S. Reynaud, O. Parriaux; Opt. Exp. (2011) 19, 9035.

[GNJ08] J. Goldstein, D.E. Newbury, D.C. Joy, P. Echlin, C.E. Lyman, E. Lifshin; *Scanning electron microscopy and x-ray microanalysis* (Springer, 2008).

[GrM06] M.N.W. Groenendijk, J. Meijer; CIRP Annals - Manufacturing Technology (2006) 55, 183.

[GRR08] M. Gedvilas, G. Raciukaitis, K. Regelskis; Appl. Phys. A (2008) 93, 203.

[GRT02] E.G. Gamaly, A.V. Rode, V.T. Tikhonchuk, B. Luther-Davies; Phys. Plasmas (2002) 9, 949.

[HBC06] J. Hermann, M. Benfarah, G. Coustillier, S. Bruneau, E. Axente, J.-F. Guillemoles, M. Sentis, P. Alloncle, T. Itina; Appl. Surf. Sci. (2006) 252, 4814.

[HCR02] M. Henyk, F. Costache, J. Reif; Appl. Surf.Sci. (2002) 197-198, 90.

[HGC97] R.F.W. Herrmann, J. Gerlach, E.E.B. Campbell; Nuclear Instruments and Methods in Physics Research Section B: Beam Interactions with Materials and Atoms (1997) 122, 401.

[HHH01] J.L. Hansen, M. van Hecke, A. Haaning, C. Ellegaard, K.H. Andersen, T. Bohr, T. Sams; Nature (2001) 410, 324.

[HMW00] M. Henyk, R. Mitzner, D. Wolfframm, J. Reif; Appl. Surf. Sci. (2000) 154-155, 249.

[HNO10] M. Hashida, S. Namba, K. Okamuro, S. Tokita, S. Sakabe; Phys. Rev. B (2010) 81, 115442.

[HRK12] S. Hoem, A. Rosenfeld, J. Krueger, J. Bonse; J. Appl. Phys. (2012) 112, 014901.

[HSR01] V. Hertel, R. Stoian, A. Rosenfeld, D. Ashkenasi, E.E.B. Campbell; Riken Review (2001) 32, 23.

[HVW99] M. Henyk, N. Vogel, D. Wolfframm, A. Tempel, J. Reif; Appl. Phys. A (1999) 69, 355.

[HWR00] M. Henyk, D. Wolfframm, J. Reif; Appl. Surf. Sci.(2000) 168, 263.

[HWW90] K. Hata, M. Watanabe, S. Watanabe; Appl. Phys. B (1990) 50, 55.

[ItN86] N. Itoh, T. Nakayama; Nucl. Instr. Meth. B (1986) 13, 550.

[Ito82] N. Itoh; Adv. Phys. (1982) 31, 491.

[JBW88] Y. Jee, K. Becker, R.M. Walser; J. Opt. Soc. Am. B (1988) 5, 648.

[JDG09] H.O. Jeschke, M.S. Diakhate, M.E. Garcia; Appl. Phys. A (2009) 96, 33.

[JGL02] H.O. Jeschke, M.E. Garcia, M. Lenzner, J. Bonse, J. Krueger, W. Kautek; Appl. Surf. Sci. (2002) 197-198, 839.

[KeB82] F. Keilmann, Y.H. Bai; Appl. Phys. A (1982) 29, 9.

[Kel65] L.V. Keldysh; Sov. Phys. JETP (1965) 20, 1307.

[KKR87] S. Kubotan, N. Kanai, J. Ruan(Gen); Phys. Stat. Sol. (1987) 139, 635.

[KOS04] S. Kouteva-Arguirova, V. Orlov, W. Seifert, H. Richter, J. Reif; Solid State Phenomena (2004) 95-96, 513.

[KPZ86] M. Kardar, G. Parisi, Y.-C. Zhang;Phys. Rev. Lett. (1986) 56, 889.

[KRD05] W. Kautek, P. Rudolph, G. Daminelli, J. Krueger; Appl. Phys. A (2005) 81, 65.

[KRV00] A. Kaiser, B. Rethfeld, M. Vicanek, G. Simon; Phys. Rev. B (2000) 61, 11437.

[KST01] S. Kawata, H.-B. Sun, T. Tanaka, K. Takada; Nature (2001) 412, 697.

[KTL95] D.Y. Kim, S.K. Tripathy, L. Li, J. Kumar; Appl. Phys. Lett. (1995) 66, 1166.

[KTV07] D.P. Korfiatis, K.-A.Th. Thoma, J.C. Vardaxoglou; J. Phys. D: Appl. Phys. (2007) 40, 6803.

[KuT77] Y. Kuramoto, T. Tsuzuki; Prog. Theor. Phys. (1977) 55, 356.

[LaL71] N.D. Lang, W. Lohn; Phys. Rev. B. (1971) 3, 1215.

[LaLd87] L.D. Landau, E.M. Lifshitz; *Theory of elasticity* (Nauka, 1987), p.246.

[LEG08] A.M. Lindenberg, S. Engemann, K.J. Gaffney, K. Sokolowski-Tinten, J. Larsson, P.B. Hillyard, D.A. Reis, D.M. Fritz, J. Arthur, R.A. Akre, M.J. George, A. Deb, P.H. Bucksbaum, J. Hajdu, D.A. Meyer, M. Nicoul, C. Blome, Th. Tschentscher, A.L. Cavalieri, R.W. Falcone, S.H. Lee, R. Pahl, J. Rudati, P.H. Fuoss, A.J. Nelson, P. Krejcik, D.P. Siddons, P. Lorazo, J.B. Hastings; Phys. Rev. Lett. (2008) 100, 135502.

[LiS00] D.von der Linde, K. Sokolowski-Tinten; Appl. Surf. Sci. (2000), 154-155, 1.

[LLS05] A.M. Lindenberg, J. Larsson, K. Sokolowski-Tinten, K.J. Gaffney, C. Blome, O. Synnergren, J. Sheppard, C. Caleman, A.G. MacPhee, D. Weinstein, D.P. Lowney, T.K. Allison, T. Matthews, R.W. Falcone, A.L. Cavalieri, D.M. Fritz, S.H. Lee, P.H. Bucksbaum, D.A. Reis, J. Rudati, P.H. Fuoss, C.C. Kao, D.P. Siddons, R. Pahl, J. Als-Nielsen, S. Duesterer, R. Ischebeck, H. Schlarb, H. Schulte-Schrepping, Th. Tschentscher, J. Schneider, D. von der Linde, O. Hignette, F. Sette, H.N. Chapman, R.W.

Lee, T.N. Hansen, S. Techert, J.S. Wark, M. Bergh, G. Huldt, D. van der Spoel, N. Timneanu, J. Hajdu, R.A. Akre, E. Bong, P. Krejcik, J. Arthur, S. Brennan, K. Luening, J.B. Hastings; Science (2005) 308, 392.

[LLZ12] Z. Li, H. Li, J. Zhang, S. Chen, M. Huang, X. Yu; Optics and Laser Technology (2012) 44, 923.

[LSB97] D. von der Linde, K. Sokolowski-Tinten, J. Bialkowski; Appl. Surf. Sci. (1997) 109-110, 1.

[Lug07] S. Lugomer; Phys. Lett. A. (2007) 361, 87.

[Man95] Spitfire-Physics Lasers: *Spitfire User's Manual* (1995) p.11.

[MaW95] L. Mandel, E. Wolf; Ch. *„Optical Beams“* in *Optical Coherence and Quantum Optics* (Cambridge University Press, 1995), p.267.

[MBP04] W. Marine, N. Bulgakova, L. Patrone, I. Ozerov; Appl. Phys. A. (2004) 79, 771.

[MCB02] M.A. Makeev, R. Cuerno, A.-L. Barabasi; Nucl. Instr. and Meth. in Phys. Res. B. (2002) 197, 185.

[MCD98] M.C. Malin, M.H. Carr, G.E. Danielson, M.E. Davies, W.K. Hartmann, A.P. Ingersoll, P.B. James, H. Masursky, A.S. McEwen, L.A. Soderblom, P. Thomas, J. Veverka, M.A. Caplinger, M.A. Ravine, T.A. Soulanille, J.L. Warren; Scince (1998) 279, 1681.

[MCN96] C. Momma, B.N. Chichkov, S. Nolte, F. von Alvensleben, A. Tünnermann, H. Welling, B. Wellegehausen; Opt. Commun. (1996) 129, 134.

[MHL78] G.N. Maracas, G.L. Harris, C.A. Lee, R.A. McFarlane; Appl. Phys. Lett. (1978) 33, 453.

[MiK95] A. Miotello, R. Kelly; Appl. Phys. Lett. (1995) 67, 3535.

[MiK99] A. Miotello, R. Kelly; Appl. Phys. A. (1999) 69, 67.

[Mil94] J.C. Miller; (Ed. R.M. Osgood) *Laser Ablation: principles and applications* (Springer, 1994), pp.11-48.

[MiM06] G. Miyaji, K. Miyazaki ; Appl. Phys. Lett. (2006) 89, 191902.

[MiM07] G. Miyaji, K. Miyazaki; Appl. Phys. Lett.. (2007) 91, 123102.

[MiM08] G. Miyaji, K. Miyazaki; Opt. Exp. (2008) 16, 16265.

[Mir04] V. Mironov; *Fundamentals of scanning probe microscopy* (The Russian Academy of Science, 2004).

[MiV03] C. Misbah, A. Valance; Eur. Phys. J. E. (2003) 12, 523.

[MKW91] Y.W. Mo, J. Kleiner, M.B. Webb, M.G. Lagally; Phys. Rev. Lett. (1991) 66, 1998.

[MuG56] E.L. Murphy, R.H. Good, Jr.; Phys. Rev. (1956) 102, 1464.

[MvA87] M. von Allmen; (Eds.: A. Mooradian, M.B. Panish) *Laser-Beam Interactions with Materials* (Springer, 1987).

[MWW87] Y. Martin, C.C. Williams, H.K. Wickramasinghe ; J. Appl. Phys. (1987) 61, 4723.

[NiB82] E.H. Nicollian, J.R. Brews; *MOS Physics and Technology* (Wiley, 1982) p.428.

[NOW91] M. Nonnenmacher, M.P. OBoyle, H.K. Wickramasinghe ; Appl. Phys. Lett. (1991) 58, 2921.

[OMR99] A.M. Ozkan, A.P. Malshe, T.A. Railkar, W.D. Brown, M.D. Shirk, P.A. Molian; Appl. Phys. Lett. (1999) 75, 3716.

[OON09] K.Oguri, Y.Okano, T. Nishikawa, H.Nakano; Phys. Rev. B. (2009) 79, 144106.

[PER89] S. Petzold, A.P. Elg, J. Reif, E. Matthias; Proc. SPIE (1989) 1438, 180.

[PKJ99] S. Park, B. Kahng, H. Jeong, A.-L. Barabasi; Phys. Rev. Lett. (1999) 83, 3486.

[PVH98] P.P. Pronko, P.A. VanRompay, C. Horvath, F. Loesel, T. Juhasz, X. Liu, G. Mourou; Phys. Rev. B. (1998) 58, 2387.

[Rat11] M. Ratzke; Diss. „*Kraftmikroskopie als Werkzeug zur Charakterisierung elektrischer Oberflächeneigenschaften“* (2011), pp.17-19.

[RCB06] J. Reif, F. Costache, M. Bestehorn; (Eds.: J. Perriere, E. Millon, E. Fogarassy) Ch. „*Self-Organized Surface Nanostructuring by Femtosecond Laser Processing“* in *Recent Advance in Laser Processingof Materials* (Elsevier, 2006) p.275.

[RCE04] J. Reif, F. Costache, S. Eckert, M. Henyk; Appl. Phys. A. (2004) 79, 1229.

[RCE07] J. Reif, F. Costache, S. Eckert; J. Phys. Conf. Ser. (2007) 59, 1.

[RCH02] J. Reif, F. Costache, M. Henyk, S.V. Pandelov; Appl. Surf. Sci. (2002) 197-198, 891.

[RCV09] J. Reif, F. Costache, O. Varlamova, G. Jia, M. Ratzke; Phys. Status Solidi C (2009) 6, 681.

[Rei09] J. Reif; (Eds.: A. Miotello, P.M. Ossi) Ch. *„Basics Physics of Femtosecond Laser Ablation“* in *Laser-Surface Interactionfor New Materials Production* (Springer, 2009), pp. 19-41.

[Rei10] J. Reif; (Ed.: P. Schaaf) Ch. *„Processing with Ultrashort Laser Pulses“* in *Laser Processing of Materials* (Springer, 2010).

[Rei89] J. Reif; Opt. Eng. (1989) 28, 1122.

[RHO98] M. Reichling, M. Huisinga, D. Ochs, V. Kempter; Surf. Sci. A. (1998) 403-404, 145.

[RHW00] J. Reif, M. Henyk, D. Wolfframm; Proc. SPIE. (2000) 3933, 26.

[RJV03] W.G. Roeterdink, L.B.F. Juurlink, O.P.H. Vaughan, J. Dura Diez, M. Bonn, A.W. Kleyn; Appl. Phys. Lett. (2003) 82, 4190.

[RKV02] B. Rethfeld, A. Kaiser, M. Vicanek, G. Simon; Phys. Rev. B. (2002) 65, 214303.

[RRF01] A. Rousse, C. Rischel, S. Fourmaux, I. Uschmann, S. Sebban, G. Grillon, Ph. Balcou, E. Foerster, J.P. Geindre, P. Audebert, J.C. Gauthier, D. Hulin; Nature (2001) 410, 65.

[RRV06] J. Reif, M. Ratzke, O. Varlamova, F. Costache; Mat. Sci. and Eng. B. (2006) 134, 114.

[RSL04] B. Rethfeld, K. Sokolowski-Tinten, D. von der Linde, S. Anisimov; Appl. Phys. A. (2004) 79, 767.

[Rub71] G.W. Rubloff; Phys. Rev. B. (1971) 3, 285.

[RVB10] J. Reif, O. Varlamova, M. Bounhalli, T. Arguirov, M. Schade, H.S. Leipner; *LASE*. International Society for Optics and Photonics. (2010) 75860H.

[RVC08] J. Reif, O. Varlamova, F. Costache; Appl. Phys. A. (2008) 92 (4), 1019.

[RVR10] J. Reif, O. Varlamova, M. Ratzke, M. Schade, H.S. Leipner, T. Arguirov; Appl. Phys. A. (2010) 101, 361.

[RVV11] J. Reif, O. Varlamova, S. Varlamov, M. Bestehorn; Appl. Phys. A. (2011) 104 (3), 969.

[SAP96] P.L. Silvestrelli, A. Alavi, M. Parrinello, D. Frenkel; Phys. Rev. Lett. (1996) 77, 3149.

[SBD01] K. Sokolowski-Tinten, C. Blome, C. Dietrich, A. Tarasevitch, M. Horn von Hoegen, D. von der Linde, A. Cavalleri, J. Squier, M. Kammler ; Phys. Rev. Lett. (2001) 87, 225701.

[SBL95] K. Sokolowski-Tinten, J. Bialkowski, D. von der Linde; Phys. Rev. B. (1995) 51, 14186.

[ScS60] W.I. Scouler, A. Smakula; Phys. Rev. (1960) 120, 1154.

[SCS99] C.W. Siders, A. Cavalleri, K. Sokolowski-Tinten, Cs. Toth, T. Guo, M. Kammler, M. Horn von Hoegen, K.R. Wilson, D. von der Linde, C.P.J. Barty; Science (1999) 286, 1340.

[SHT09] S. Sakabe, M. Hashida, S. Tokita, S. Namba, K. Okamuro; Phys. Rev. B. (2002), 79, 033409.

[SiB81] J.E. Sipe, J. Becher; J. Opt. Soc. Am. (1981) 71, 1286.

[Sig69] P. Sigmund; Phys. Rev. (1969) 184, 383.

[Sig73] P.Sigmund; Journal of material scince (1973) 8, 1545.

[Sin93] J. Singh; Ch. *„Semiconductor Bandstructure“* in *Physics of Semiconductors and their Heterostructures* (McGraw Hill College, 1993).

[Sip80] J.E. Sipe; Phys.Rev.B. (1980) 22, 1589.

[SJL07] H. Sun, T. Jia, C. Li, X. Li, S. Xu, D. Feng, X. Wang, X. Ge, Z. Xu; Solid State Communication (2007) 141, 127.

[SKB77] A. Schmid, P. Kelly, P. Braeunlich; Phys. Rev. B. (1977) 16, 4569.

[SKI08] A. Serpenguezel, A. Kurt, I. Inanc, J. E. Cary, E. Mazur; Journal of Nanophotonics. (2008) 2, 021770.

[SKK73] M. Siegrist, G. Kaech, F.K. Kneubuehl; Appl. Phys. (1973) 2, 45.

[SKS05] G. Seifert, M. Kaempfe, F. Syrowatka, C. Harnagea, D. Hesse, H. Graener; Appl. Phys. A. (2005) 81, 799.

[SLF87] R.W. Schoenlein, W.Z. Lin, J.G. Fujimoto, G.L. Eesley; Phys. Rev. Lett. (1987) 58, 1680.

[SoL00] K. Sokolowski-Tinten, D. von der Linde; Phys. Rev. B. (2000) 61, 2643.

[SRA02] R. Stoian, A. Rosenfeld, D. Ashkenasi, I.V. Hertel, N.M. Bulgakova, E.E.B. Campbell; Phys. Rev. Lett.. (2002), 88, 097603.

[Sri86] R. Srinivasan; Scince. (1986) 234, 559.

[StB90] P. Stampfli, K.H. Bennemann; Phys. Rev. B. (1990) 42, 7163.

[StB94] P. Stampfli, K.H. Bennemann; Phys. Rev. B. (1994) 49, 7299.

[SVR10] M. Schade, O. Varlamova, J. Reif, H. Blumtritt, E. Erfurth, H.S. Leipner; Anal. Bioanal. Chem. (2010) 396, 1905.

[SYP83] J.E. Sipe, J.F. Young, J.S. Preston, H.M. van Driel; Phys. Rev. B. (1983) 27, 1141.

[TBL98] C. Teichert, J.C. Bean, M.G. Lagally; Appl. Phys. A. 1998, 67, p.675.

[TeS81] P.A. Temple, M.J. Soileau; IEEE Journal of Quantum Electronics. (1981) 17, 2067.

[ThC04] S. Theppakuttai, S.C. Chen; J. Appl. Phys. (2004) 95, 5049.

[TKI89] K. Tanimura, T. Katoh, N. Itoh; Phys. Rev. B. (1989) 40, 1282.

[TKM07] T. Tomita, K. Kinoshita, S. Matsuo, S. Hashimoto; Appl. Phys. Lett. (2007) 90, 153115.

[VoG08] A.Y. Vorobyev, C. Guoa; Appl. Phys. Lett. (2008) 92, 041914.

[VWR98] H. Varel, M. Waehmer, A. Rosenfeld, D. Ashkenasi, E.E.B. Campbell; Appl. Surf. Sci. (1998) 127-129, 128.

[Wan94] X.Y. Wang, D.M. Riffe, Y.-S. Lee, M.C. Downer; Phys. Rev. B. (1994) 50, 8016.

[WMF03] Q. Wu, Y. Ma, R. Fang, Y. Liao, Q. Yu; Appl. Phys. Lett. (2003) 82, 1703.

[WMW77] R.T. Williams, C.L. Marquardt, J.W. Williams, M.N. Kabler; Phys. Rev. B. (1977) 15, 5003.

[WRK03] J. Wang, P. Roman, E. Kamieniecki, J. Ruzylloa; Electrochem. Solid State Lett. (2003) 18, 19379.

[YaT99] O. Yavas, M. Takai ; J. Appl. Phys. (1999) 85, 4207.

[YMK03] N. Yasumaru, K. Miyazaki, J. Kiuchi; Appl. Phys. A (2003) 76, 983.

[YPD83] J.F. Young, J.S. Preston, H.M. van Driel, J.E. Sipe; Phys. Rev. B (1983) 27, 1155.

[YSD84] J.F. Young, J.E. Sipe, H.M. van Driel; Phys. Rev. B. (1984) 30, 2001.

[YSP82] J.F. Young, J.E. Sipe, J.S. Preston, H.M. van Driel; Appl. Phys. Lett. (1982) 41, 261.

[YUK10] M. Yamaguchi, S. Ueno, R. Kumai, K. Kinoshita, T. Murai, T. Tomita, S. Matsuo, S. Hashimoto; Appl. Phys. A. (2010) 99, 23.

[Zan88] A. Zangwill; *Physics Surfaces* (Cambridge University Press, 1988).

[ZFH05] B. Ziberi, F. Frost, T. Hoeche, B. Rauschenbach; Phys. Rev. B. (2005) 72, 235310.

[ZGO06] S.V. Zabotnov, L.A. Golovan, I.A. Ostapenko, Yu.V. Ryabchikov, P.K. Kashkarov, V.V. Yakovlev; JETP Letters (2006) 83, 69.

[ZhG00] L.V. Zhigilei, B.J. Garrison; J. Appl. Phys. (2000) 88, 1281.

[ZPP06] V. Zorba, L. Persano, D. Pisignano, A. Athanassiou, E. Stratakis, R. Cingolani, P. Tzanetakis, C. Fotakis; Nanotechnology (2006) 17, 3234.

[ZTW98] Y.F. Zhang, Y.H. Tang, N. Wang, D.P. Yu, C.S. Lee, I. Bello, S.T. Lee; Appl. Phys. Lett. (1998) 72, 1835.